Technische Universität München
Institut für Energietechnik

Lehrstuhl für Thermodynamik

Impact of Hydrodynamics on Initial Cake Layer Formation in Forward Osmosis

Andreas Michael Kastl

Vollständiger Abdruck der von der Fakultät für Maschinenwesen der Technischen Universität München zur Erlangung des akademischen Grades eines

Doktor – Ingenieurs

genehmigten Dissertation.

Vorsitzende:
Prof. Dr. rer. nat. Julija Zavadlav
Prüfer der Dissertation:
1. Prof. Dr.-Ing. Thomas Sattelmayer
2. Prof. Edo Bar-Zeev, Ph.D.

Die Dissertation wurde am 21.01.2021 bei der Technischen Universität München eingereicht und durch die Fakultät für Maschinenwesen am 14.05.2021 angenommen.

Acknowledgement

I pursued this thesis during my time at the Chair of Thermodynamics of the Technical University of Munich. My thanks to Prof. Dr.-Ing. Thomas Sattelmayer for the scientific supervision of my thesis. Your insightful feedback has helped me focus my research efforts. I would also like to thank Prof. Edo Bar-Zeev, Ph.D. for being my second examiner. Thank you for the great scientific discussions and collaboration on our publications. I also wish to extend my thanks to Prof. Dr. rer. nat. Julija Zavadlav for taking the chair in my examination.

My gratitude goes to Dr.-Ing. Florian Kiefer and Alexander Präbst for introducing me to the topic of water research, supporting my lab work, and collaboration on my first publication. Thanks also to Bernd Heithorst for numerous discussions and for reviewing my thesis. Thanks to Anne Bogler for teaching me how to work in a microbiology lab and for great teamwork. My thanks to Dr.-Ing. Markus Spinnler for his support and for reviewing my thesis. I also wish to thank Simon Tartsch for giving me feedback on my thesis. I am grateful to the TP and SI group participants for their valuable input, especially Thomas Hofmeister and Gerrit Heilmann. Several parts of my test rig had to be manufactured or controlled. I wish to extend my thanks to the workshop, especially Jens Hümmer, Thomas Schleussner, and Helmut Koller. Additionally, many thanks to Helga Bassett und Sigrid Schulz-Reichwald for their administrative support.

Last but not least, I would like to thank my family and friends for their support during these years. Above all, I would like to thank my wife Lena for her patience, understanding, and support.

Aying, August 2021 Andreas Kastl

Abstract

Freshwater is a rare resource. Although it can be replenished by polishing wastewater with membrane processes, biofouling is a severe problem. Biofouling increases the costs of wastewater treatment by membrane processes and must be mitigated. The initial stage of cake layer formation is critical during biofilm formation and biofouling development in membrane systems. However, the effects of hydrodynamic conditions on the deposition of bacteria remain unclear during the initial stages of biofilm formation. This dissertation investigates the impact of permeate water flux and crossflow velocity on fouling propensity in forward osmosis systems with spacers. Additionally, the fouling mitigation potential of pulsating flows is assessed.

Fluorescence microscopy was used to track *Bacillus subtilis* and inert beads in situ and in real-time in a forward osmosis system with spacers during the first hours of biofilm formation. The impact of permeate water flux, crossflow velocity, and pulsating flows on spatio-temporal deposition patterns was quantified. Subsequently, core mechanisms of particle deposition were identified by computational fluid dynamics. The insights gained in steady-state and transient operating conditions were then applied to spiral-wound modules. Areas prone to fouling were identified at steady-state and pulsating flow conditions.

The results of this research indicate that an appropriate choice of hydrodynamic conditions can minimize bacteria accumulation before biofilm formation in forward osmosis. Another key finding is that the ratio of permeate water flux to crossflow velocity impacts all aspects of particle deposition. Concomitantly, pulsating flows are a viable technique to delay the onset of fouling in membrane processes. These insights are relevant in new or cleaned forward osmosis membrane systems used to treat water of high fouling propensity and could aid in designing new spacer geometries.

Kurzfassung

Süßwasser ist eine wichtige, aber knappe Ressource. Durch Membranverfahren lässt sich Süßwasser aus verunreinigtem Wasser aufbereiten, jedoch sind diese Verfahren sehr anfällig für Biofouling. Biofouling treibt die Kosten der Abwasseraufbereitung signifikant in die Höhe und muss daher minimiert werden. Für die Bildung eines Biofilms und die Entwicklung von Biofouling in Membransystemen ist vor allem das Anfangsstadium der Ablagerung von Bakterien ausschlaggebend. Es ist naheliegend, dass sich hydrodynamischen Bedingungen auf dieses Anfangsstadium und damit auf die Lebenszeit eines Membransystems auswirken, jedoch wurde dies bisher noch nicht hinreichend untersucht. Die vorliegende Dissertation analysiert den Einfluss von Permeation und Überströmungsgeschwindigkeit auf die Ablagerung in der Vorwärtsosmose. Weiterhin wird das Minderungspotential pulsierender Strömungen auf Fouling untersucht.

Fluoreszenzmikroskopie ermöglichte hierbei die In-situ- und Echtzeit-Verfolgung von *Bacillus subtilis* und inerten Partikeln während der ersten Stunden der Biofilmbildung in einem Vorwärtsosmose System mit Spacern. In diesem Zusammenhang wurde der Einfluss der hydrodynamischen Bedingungen auf die Ablagerungsmuster örtlich und zeitlich quantifiziert. Mithilfe von numerischer Strömungsmechanik konnten die Kernmechanismen der Partikelablagerung identifiziert werden. Die gewonnenen Erkenntnisse wurden dann auf die Vorgänge in einem Spiralwickelmodul übertragen. Es konnten die Bereiche im Spiralwickelmodul ermittelt werden, die bei stationären und pulsierenden Strömungsbedingungen jeweils für Fouling anfällig sind.

Die Ergebnisse zeigen, dass das Verhältnis von Permeation zu Überströmungsgeschwindigkeit alle Aspekte der Partikelablagerung in der Vorwärtsosmose beeinflusst und eine geeignete Wahl hydrodynamischer Parameter die Ablagerung von Bakterien auf der Membranoberfläche minimieren kann. Zudem kann das Einsetzen von Fouling in Membranverfahren durch pulsierende Strömungen verzögert werden, was wiederum die Lebenszeit solcher Membransysteme erhöht. Diese Erkenntnisse sind relevant für neue

oder bereits gereinigte Vorwärtsosmose-Membransysteme, die zur Aufbereitung von sehr verschmutztem Wasser eingesetzt werden, und können bei der Geometrieoptimierung von Spacern helfen.

Contents

List of Figures

List of Tables

Nomenclature

Abbreviations

ANOVA	Analysis of variance
CC	Co-current
CO	Counter-current
CFD	Computational fluid dynamics
CP	Concentration polarization
CLSM	Confocal laser scanning microscopy
CTA	Cellulose triacetate
DDW	Double distilled water
DLVO	Derjaguin Landau Verweey Overbeek
ECP	External concentration polarization
EDTA	Ethylenediaminetetraaceticacid
EPS	Extracellular polymeric substance
FCM	Flow cytometry method
FO	Forward osmosis
GCI	Grid convergence index
HCHP	High crossflow and high permeation
HCLP	High crossflow and low permeation
ICP	Internal concentration polarization
LCHP	Low crossflow and high permeation
LCLP	Low crossflow and low permeation
LSD	Least significant difference
LB	Luria–Bertani broth
NF	Nanofiltration
OCT	Optical coherence tomography
OD	Optical density

RO	Reverse osmosis
ROP	Reverse osmosis permeate
SWM	Spiral-wound module
TFC	Thin-film composite

Constants

e	Elementary charge	1.6022×10^{-19}	C
k_B	Boltzmann constant	1.3806×10^{-23}	$m^2\,kg\,s^{-2}\,K^{-1}$
R	Gas constant	8.3145	$J\,K^{-1}\,mol^{-1}$
ϵ_0	Vacuum permittivity	8.8542×10^{-12}	$F\,m^{-1}$

Dimensionless Numbers

Re	Reynolds number
$\mathrm{Re_r}$	Relative Reynolds number
$\mathrm{Re_G}$	Shear Reynolds number
Sh	Sherwood number
Sc	Schmidt number

Latin Letters

a	Damping rate	m^{-1}
A	Area	m^2
$A_{V,SP}$	Volume specific surface area	$m^2\,m^{-3}$
$A_{orifice}$	Orifice parameter	m^{-4}
B	Salt permeability	$m\,s^{-1}$
BA	Bacterial abundance	$cells\,m^{-2}$
$B_{orifice}$	Orifice parameter	-
C_D	Drag coefficient	-
C_L	Lift force coefficient	-
c	Molar concentration	$mol\,m^{-3}$

D	Diffusion coefficient	$\mathrm{m^2\,s^{-1}}$
DP	Normalized particle count	$\mathrm{beads\,m^{-2}}$
d	Diameter	m
d_h	Hydraulic diameter	m
e	Error	-
F	Force	N
f	Frequency	Hz
H	Hamaker constant	J
h	Channel height	m
j	Specific mass flux	$\mathrm{m\,s^{-1}}$
K	Membrane permeability	$\mathrm{m\,s^{-1}\,Pa^{-1}}$
k	Mass transfer coefficient	$\mathrm{m\,s^{-1}}$
L	Length	m
l	Thickness	m
M	Molar mass	$\mathrm{kg\,mol^{-1}}$
m	Mass	kg
$\dot{m}$	Mass flow rate	$\mathrm{kg\,s^{-1}}$
N	Number	-
n	Mole number	mol
p	Pressure	Pa
p	Level of statistical significance	-
R	Distance	m
R	Proportion of variance	-
r	Radius	m
S	Structural parameter	m
T	Temperature	K
t	Time	s
u	Velocity	$\mathrm{m\,s^{-1}}$
V	Volume	$\mathrm{m^3}$
V_m	Molar volume	$\mathrm{m^3\,mol^{-1}}$
$\dot{V}$	Volume flow rate	$\mathrm{m^3\,s^{-1}}$
w	Mass fraction	$\mathrm{kg\,kg^{-1}}$
x	Position	m
x_A	Mole fraction of component A	-

x_B	Mole fraction of component B	-
z	Ion valency	-

Greek Letters

α_d	Particle volume fraction	-
Δ	Difference operator	-
δ	Thickness of boundary layer	m
ε	Porosity, void fraction	-
ϵ_r	Relative permittivity	-
η	Kinematic viscosity	Pa s
κ_D	Inverse Debye length	m^{-1}
κ_C	Conductivity	$S\,m^{-1}$
λ	Wavelength of dispersion interaction	m
μ	Chemical potential	$J\,mol^{-1}$
ν	Dynamic viscosity	$m^2\,s^{-1}$
Π	Osmotic pressure	Pa
ρ	Density	$kg\,m^{-3}$
σ	j_W / u_F	-
τ	Fluid shear	Pa
τ_T	Tortuosity	-
ϕ	Potential energy	J
Ψ	Deposition probability	$\%\,m^{-1}$
ψ	Surface potential	V
ω	Angular frequency	Hz
ζ	Osmotic coefficient	-

Subscripts

$(...)_a$	Active layer
$(...)_b$	Bulk
$(...)_{BS}$	*Bacillus subtilis*
$(...)_{cross}$	Cross-sectional

$(...)_{D}$	Draw
$(...)_{dep}$	Deposited
$(...)_{edl}$	Electrostatic double layer
$(...)_{exp}$	Experiment
$(...)_{F}$	Feed
$(...)_{f}$	Fluid
$(...)_{inj}$	Injected
$(...)_{j}$	Running index
$(...)_{k}$	Running index
$(...)_{m}$	Membrane
$(...)_{max}$	Maximum value
$(...)_{min}$	Minimum value
$(...)_{o}$	Observation zone
$(...)_{orifice}$	Orifice
$(...)_{P}$	Adjacent cell
$(...)_{p}$	Particle
$(...)_{PB}$	Polystyrene beads
$(...)_{S}$	Salt
$(...)_{sim}$	Simulation
$(...)_{SL}$	Support layer
$(...)_{tot}$	Total
$(...)_{VdW}$	Van der Waals
$(...)_{W}$	Water

Superscripts

$(\tilde{...})$	Oscillating value
$(\bar{...})$	Mean value
$(\vec{...})$	Vector
$(...)^{*}$	Pure substance or in equilibrium with a pure substance
$(...)^{ref}$	Reference

Forces

$\vec{F}_{\mathrm{P}}$	Pressure gradient force	N
$\vec{F}_{\mathrm{VdW}}$	Van der Waals force	N
$\vec{F}_{\mathrm{L}}$	Lift force	N
$\vec{F}_{\mathrm{D}}$	Drag force	N
$\vec{F}_{\mathrm{G+B}}$	Gravity and buoyancy force	N
$\vec{F}_{\mathrm{V}}$	Volume force	N
$\vec{F}_{\mathrm{S}}$	Surface force	N
$\vec{F}_{\mathrm{edl}}$	Electrostatic double layer force	N

1 Introduction

1.1 Background and Motivation

Population growth and urbanization have increased significantly within the last few decades, leading to an increased demand for freshwater [5]. Sea water desalination and water reuse are two methods to increase the supply of freshwater above the limit of the hydrological cycle [6]. Theoretically, sea water desalination could provide an unlimited supply of freshwater but requires more energy than wastewater treatment [7]. Therefore, wastewater treatment is a more viable technique than sea water desalination.

Wastewater often contains a high concentration of organic material, bacteria, and pathogens. These contaminants can be entirely removed by the membrane processes nanofiltration (NF) and reverse osmosis (RO). These methods are the most predominant ones for polishing wastewater [8] but require extensive pre-treatment. Forward osmosis (FO) could reduce the pre-treatment. FO is a membrane technology which rejects particles and pathogens, does not require high hydraulic pressure, and is less prone to fouling than other membrane processes [9, 10].

In FO, an osmotic pressure gradient drives a permeate water flux from the feed solution, which is wastewater, to the draw solution. The draw solution is diluted while the feed solution is concentrated. Hence, the draw solution has to be regenerated. The FO regeneration step consumes significantly more energy than the osmosis process itself. The most common process for regeneration is RO. In that case, FO is the pre-treatment step for RO. In most applications, the FO-RO setup is the most energy-efficient as RO has a theoretical minimum energy requirement of $1.5\,\mathrm{kW\,h\,m^{-3}}$ [11].

FO is very versatile in its application [12] and has been used to treat oil and

gas well fracturing water [13–15], landfill leachate [16], anaerobic digester centrate [17], activated sludge [18], and wastewater effluent from municipal sources [19, 20]. Spiral-wound modules (SWM) maximize the packing density and are typical for commercial use. In an SWM, the membrane is wrapped around a central tube with net-type spacers separating the membrane sheets [21]. The spacers enhance mixing and reduce concentration polarization but also increase biofouling [22, 23].

Biofouling is the negative effect of biofilm formation in industrial processes. Biofilm formation in the feed channel leads to increased pressure drop along the SWM and a decrease in permeate water flux. A biofilm is a complex and sessile microbial entity that evolves from cell-to-cell and cell-to-surface interactions [3]. Extracellular polymeric substances (EPS) reinforce microbial communities of multi-layered, loosely packed live and dead cells [24]. The EPS contains approximately 70 % proteins and polysaccharides. The rest is composed of humic substances, uronic acids as well as DNA [25]. In the biofilm, water channels separate cells and allow transport of oxygen, nutrients, chemical messengers, genetic material, as well as anti-microbial agents [26]. [3]

In the initial stage of biofilm formation, organic matter and bacterial cells deposit on the membrane surface and attach reversible via different physicochemical interactions [27]. Irreversible attachment may follow as bacteria secrete EPS, which anchor the cells to each other and the surface [3, 28]. Although cells initiate reproduction after a few minutes, it takes a few hours to develop the first biofilm colonies. In this initial stage, the cake layer develops as a monolayer. [29, 30]

During the initial stage of biofilm formation, various factors may influence deposition within the membrane channel. These factors include the hydrodynamic conditions in the feed channel, the bacterial species, and concentration of nutrients in the feed solution, as well as surface properties, including charge and hydrophobicity [3,29,31]. Therefore, understanding this first stage of biofilm formation is crucial for the development of biofouling mitigation approaches.

To date, different studies have determined the impact of hydrodynamics on membrane fouling using a variety of foulants with various effects [22, 32–37]. However, no quantitative reports are available on the impact of crossflow and permeate water flux on the initial stages of biofilm formation in membrane systems with spacers. The quantification of deposition in time and space by fluorescence microscopy can provide crucial information on areas prone to fouling and may lead to new approaches for fouling mitigation.

One of these new approaches for fouling mitigation might be pulsating feed flows. Kuruneru et al. [38] stated that pulsating flows change the motion of particles in the fluid, increase the fluid shear, which periodically disrupts the fouling layer, and alter the aggregate structure of deposited particles in a heat exchanger. These mechanisms may also offer a higher probability of particle detachment and re-suspension into the bulk solution of a membrane process. Pulsating feed flows decreased fouling in RO [39] significantly. However, the impact of pulsating flows on cake layer formation in FO has not been studied previously. Spatial and temporal quantification of deposition patterns may provide information about important fouling mitigation parameters of pulsating flows.

1.2 Research Aims and Objectives

The dissertation has two research aims:

1. Investigate the impact of steady-state hydrodynamics on cake layer formation in an FO SWM.
    - Quantify the impact of crossflow velocity and permeate water flux on particle deposition.
    - Model the impact of hydrodynamics on particle deposition in a spacer-filled channel with computational fluid dynamics (CFD).
    - Predict hydrodynamics in an FO SWM at steady-state. Identify areas that are prone to biofouling at steady-state.

2. Assess the potential of pulsating feed flows to mitigate cake layer formation in an FO SWM.

    - Quantify the impact of pulsating feed flows on the deposition of particles.
    - Identify areas that are prone to biofouling with pulsating feed flows.

1.3 Scope, Value and Outline of this Dissertation

Freshwater is a rare source on this planet. Treating wastewater uses less energy and is thus more viable to produce freshwater than sea water desalination. However, biofouling of membrane processes is a severe hindrance to widespread applications. Increasing the understanding of initial cake layer formation is crucial when developing a system that treats wastewater. Decreasing the fouling potential of FO reduces energy costs and increases the likelihood of application.

The main goal of this dissertation is to increase the understanding of the impact of hydrodynamics on cake layer formation. The cake layer was visualized in a bench-scale FO test rig with spacers by fluorescence microscopy. Thus, it was possible to gather detailed information about the initial stage of cake layer formation. To date, there is no detailed experimental data concerning initial cake layer formation in FO. This dissertation provides spatial and temporal data for the deposition of *Bacillus subtilis* in FO with spacers at different operating conditions. *Bacillus subtilis* are Gram-positive, rod-shaped, and motile bacteria that form spores and are often found in domestic wastewater [34, 40, 41]. *Bacillus subtilis* are commonly used as model bacteria [42, 43].

The dissertation also provides data about the impact of pulsating flows on the deposition of polystyrene beads. Although the ability of bacteria to move may alter the deposition process, polystyrene beads have recently been used as a proxy for bacterial deposition [44–47]. Studies in

parallel plate flow cells demonstrated that the deposition of bacteria and polystyrene beads are similar [48].

This dissertation thus contributes to the understanding of

- the impact of permeate water flux and crossflow velocity on cake layer formation in FO.
- the impact of pulsating flows on cake layer formation in FO.

The scope of this dissertation covers the impact of hydrodynamics, both steady-state and transient, on the initial stage of cake layer formation in FO with spacers. The results of this investigation also have implications for other membrane systems.

Following the Introduction, Chapter 2 provides the principles of FO and particle deposition. Chapter 3 investigates the impact of crossflow velocity and permeate water flux on the deposition of *Bacillus subtilis* in FO with fluorescence microscopy. Chapter 4 investigates deposition on a microscopic level with CFD. Chapter 5 quantifies the impact of pulsating flows on particle deposition with fluorescence microscopy. In Chapter 6, the FO process is investigated in an SWM. The system simulation identifies areas prone to biofouling and provides design guidelines for transient operating conditions. Chapter 7 summarizes the key findings and concludes the dissertation.

2 Fundamentals of Forward Osmosis and Fouling

This chapter provides the fundamentals for the present dissertation. The first part covers the chemical potential and osmotic pressure of electrolyte solutions. The fundamentals of the forward osmosis (FO) process are introduced next. The third part discusses the particle deposition process and modeling of elemental particle forces.

2.1 Thermodynamics of an Electrolyte Solution

This section is based on the book of Atkins and de Paula [1]. The osmotic pressure will later be used to calculate the permeate water flux and reverse salt flux in FO.

2.1.1 Chemical Potential

The influence of pressure on the chemical potential of a system is important to explain the concept of osmotic pressure. The chemical potential is defined as the molar Gibbs free energy. For simplification purposes, the chemical potential of a container filled with vapor (cf. Fig. 2.1a) will be considered first. The influence of the pressure on the chemical potential of the vapor can be evaluated by changing the pressure of the system from a reference p^{ref} to p. A constant temperature is assumed. The chemical potential μ would deviate from an arbitrary reference $\mu(p^{\mathrm{ref}})$ by

$$\mu(p) = \mu(p^{\mathrm{ref}}) + \int_{p^{\mathrm{ref}}}^{p} V_{\mathrm{m}} \mathrm{d}p. \tag{2.1}$$

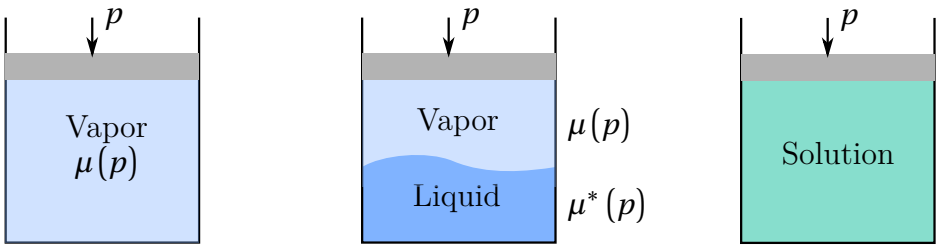

(a) System with vapor. **(b)** System with vapor and liquid. **(c)** System with solvent A and solute B.

Figure 2.1: Chemical potential of a closed system.

For an ideal gas, the molar volume can be calculated as $V_m = R\ T/p$. The correlation of pressure and chemical potential for a system that is filled with vapor is then:

$$\mu(p) = \mu(p^{\text{ref}}) + R\ T\ \ln\frac{p}{p^{\text{ref}}}. \tag{2.2}$$

Next, a system that is filled with vapor and liquid will be investigated (cf. Fig. 2.1b). When considering a closed container that is filled with vapor and liquid at equilibrium, the chemical potential of the vapor must be equal to the chemical potential of the liquid:

$$\mu^* = \mu^{\text{ref}} + R\ T\ \ln\frac{p^*}{p^{\text{ref}}}. \tag{2.3}$$

The third system is filled with a solution of solvent A and solute B (cf. Fig. 2.1c). In the following, the superscript * denotes a pure substance, while no superscript indicates that the substance is part of a solution. When another substance (B) is present, the chemical potential of component A changes to:

$$\mu_A = \mu_A^{\text{ref}} + R\ T\ \ln\frac{p_A}{p^{\text{ref}}}. \tag{2.4}$$

By combining the equation for a pure liquid 2.3 with the equation for the

chemical potential of A in a mixture 2.4 the reference values for pressure and chemical potential can be eliminated:

$$\mu_A = \mu_A^* + R\ T\ \ln\frac{p_A}{p_A^*}. \tag{2.5}$$

Francois Raoult conducted experiments with liquids that had similar physical properties. He observed that the mole fraction x_A of component A in the liquid mixture is approximately equal to the ratio of partial pressure p_A of component A to its vapor pressure p_A^* as a pure substance:

$$x_A = \frac{p_A}{p_A^*}. \tag{2.6}$$

Mixtures obeying Raoult's law across the whole composition range from pure A to pure B are called ideal solutions. For those, it follows from 2.5 and 2.6:

$$\mu_A = \mu_A^* + R\ T\ \ln x_A. \tag{2.7}$$

Aqueous salt solutions deviate from the behavior of an ideal solution already at concentrations as low as $1\,\mathrm{mol\,m^{-3}}$ [1]. The osmotic coefficient ζ compensates for the deviation

$$\mu_A = \mu_A^* + \zeta(T, x_A)\ R\ T\ \ln x_A. \tag{2.8}$$

2.1.2 Osmotic Pressure

Osmosis is the spontaneous passage of pure water into the saline solution across a membrane [1]. Figure 2.2 depicts a system where pure water is separated by a membrane from a saline solution. It is assumed that the membrane is semi-permeable, which means that the membrane is passable by pure water but not salt. The osmotic pressure Π is the hydraulic pressure that is needed to prevent such spontaneous passage.

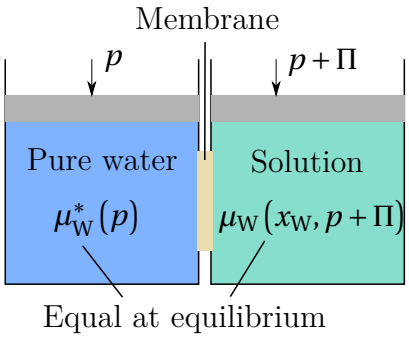

Figure 2.2: Schematic representation of the osmotic process. Figure adapted from Atkins and de Paula [1].

In the saline solution, the chemical potential of water $\mu_W(p)$ is lower than that of pure water $\mu^*_W(p)$. The difference in chemical potential between the pure water and the saline solution would lead to a passage of pure water through the membrane. However, the osmotic pressure Π was defined as the hydraulic pressure that leads to an equilibrium between both sides. Hence, the chemical potentials of pure water $\mu^*_W(p)$ and the saline solution $\mu_W(x_W, p+\Pi)$ are equal:

$$\mu^*_W(p) = \mu_W(x_W, p+\Pi). \tag{2.9}$$

The chemical potential of a real solution was derived in section 2.1.1. Combining equations 2.1, 2.8, and 2.9 leads to

$$-\zeta\ R\ T\ \ln x_W = \int_p^{p+\Pi} V_m\ \mathrm{d}p. \tag{2.10}$$

The molar volume V_m of the liquid solution can be assumed to be independent of the pressure. The osmotic pressure Π is then

$$\Pi = -\ \zeta\ R\ T\ \frac{\ln x_W}{V_m}. \tag{2.11}$$

The draw solute within this dissertation is sodium chloride. Solving sodium chloride in water leads to a dissociation of Na^+ and Cl^- ions. Hence there

are three components: (i) water, (ii) sodium, and (iii) chloride ions. In this three-component mixture, the molar concentration x_W of water can be replaced by $1 - 2\ x_{NaCl}$. The term $\ln(1 - 2\ x_{NaCl})$ can be approximated by $-2\ x_{NaCl}$

$$\Pi \approx 2\ \zeta_{NaCl}\ R\ T\ \frac{x_{NaCl}}{V_m} = 2\ \zeta_{NaCl}\ R\ T\ c_{NaCl}. \tag{2.12}$$

The mean osmotic coefficient for sodium chloride ζ_{NaCl} can be calculated by interpolating between values provided by Clarke and Glew [49]. The error of the approximation $\ln(1 - 2\ x_{NaCl}) \approx -2\ x_{NaCl}$ increases with an increase of c_{NaCl}. The highest sodium chloride concentration was $1 \times 10^3\,\mathrm{mol\,m^{-3}}$ in this dissertation. For this value, the approximation produces an error of 3.6 %. A further simplification for dilute solutions is the van't Hoff equation, which neglects the osmotic coefficient ζ

$$\Pi \approx 2\ R\ T\ c_{NaCl}. \tag{2.13}$$

The error of the van't Hoff equation increases with an increase in sodium chloride concentration. At a concentration of $1 \times 10^3\,\mathrm{mol\,m^{-3}}$, the van't Hoff equation leads to an error of 7.4 %. Hence, the van't Hoff equation was used in this dissertation.

2.2 Forward Osmosis

The FO section introduces a model for the calculation of permeate water flux and reverse salt flux across the membrane. Additionally, hydrodynamics in spacer-filled channels, membrane choice, and draw solution regeneration are discussed.

2.2.1 Mass Transfer Across the Membrane

In FO, a membrane separates the feed and draw channel in an open system (cf. Fig. 2.3). Wastewater passes the feed channel, while a sodium chloride

solution passes the draw channel. Figure 2.2 depicted a closed system with a separation of pure water and a saline solution. However, the membrane separates two solutions here. At the end of the module, mass transfer across the membrane has led to a concentration of the wastewater and dilution of the draw solution. This section introduces a model published by Tiraferri et al. [2] to calculate the permeate water flux and reverse salt flux in FO.

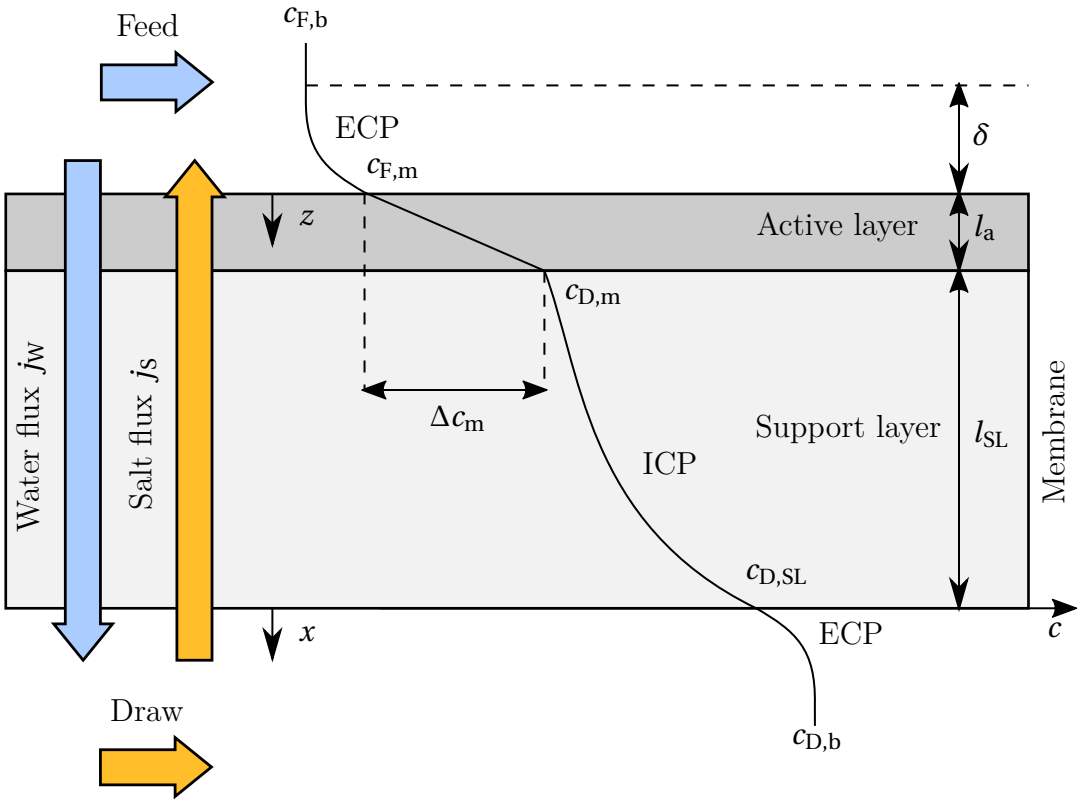

Figure 2.3: Concentration polarization and fluxes in FO. Figure adapted from Tiraferri et al. [2] and Bogler et al. [3].

Section 2.1.2 assumed that the membrane is semi-permeable. However, the membrane is not a perfect barrier and draw solutes are transported across the membrane [50]. In the case of a membrane with a high salt rejection, the permeate water flux j_W across the active layer is the membrane permeability K multiplied by the osmotic pressure difference $\Delta\Pi_m$ [2]

$$j_W = K\ \Delta\Pi_m. \tag{2.14}$$

The reverse salt flux j_S is

$$j_S = -B \left(c_{D,m} - c_{F,m}\right). \tag{2.15}$$

Here, $c_{D,m}$ and $c_{F,m}$ are the molar ion concentrations on draw and feed side of the active layer. B is the salt permeability of the membrane.

The permeate water flux reduces the local molar ion concentration $c(x)$ within the supporting layer. This effect is called internal concentration polarization (ICP). The salt flux within the support layer is the sum of diffusive and convective salt transport

$$j_S(x) = -D_{SL} \frac{\mathrm{d}c(x)}{\mathrm{d}x} + j_W \; c(x). \tag{2.16}$$

The diffusion coefficient of the support layer D_{SL} is lower than the diffusion coefficient of the bulk solution D. D_{SL} is D multiplied by the ratio of porosity ε to tortuosity τ_T of the support layer

$$D_{SL} = \frac{D \; \varepsilon}{\tau_T}. \tag{2.17}$$

At steady-state, the salt flux across the support layer (cf. Eq. 2.16) must be equal to the salt flux across the active layer (cf. Eq. 2.15)

$$D_{SL} \; \frac{\mathrm{d}c(x)}{\mathrm{d}x} - j_W \; c(x) = B \left(c_{D,m} - c_{F,m}\right). \tag{2.18}$$

Equation 2.18 is a linear first-order differential equation. The boundary condition is $c(0) = c_{D,SL}$. Solving the differential equation leads to:

$$c_{D,m} = \underbrace{c_{D,SL} \exp\left(-\frac{j_W \; S}{D}\right)}_{\text{Dilutive ICP}} + \underbrace{\frac{B}{j_W} \left(c_{D,m} - c_{F,m}\right) \left[\exp\left(-\frac{j_W \; S}{D}\right) - 1\right]}_{\text{Reverse salt permeation}}. \tag{2.19}$$

Here, S is the support layer structural parameter and defined as $S = l_{SL} \tau_T / \epsilon$.

External concentration polarization (ECP) must also be considered. Wastewater contains a low concentration of ions. The membrane active layer selectively retains these ions in the feed solution. The concentration of solutes builds up in the boundary layer at the active side. The salt flux in the feed solution can be calculated similar to equation 2.16:

$$j_S = -D\frac{\mathrm{d}c(z)}{\mathrm{d}z} + j_W\ c(z). \tag{2.20}$$

Once steady-state has been reached, the salt flux within the ECP boundary layer (cf. Eq. 2.20) has to be equal to the salt flux across the active layer (cf. Eq. 2.15)

$$D\frac{\mathrm{d}c(z)}{\mathrm{d}z} - j_W\ c(z) = B\ \left(c_{\mathrm{D,m}} - c_{\mathrm{F,m}}\right). \tag{2.21}$$

At position $z = -\delta$ the molar ion concentration has to be $c_{\mathrm{F,b}}$. Solving equation 2.21 leads to

$$c_{\mathrm{F,m}} = \underbrace{c_{\mathrm{F,b}} \exp\left(\frac{j_W}{k}\right)}_{\text{ECP}} - \underbrace{\frac{B}{j_W}\left(c_{\mathrm{D,m}} - c_{\mathrm{F,m}}\right)\left[1 - \exp\left(\frac{j_W}{k}\right)\right]}_{\text{Reverse salt permeation}}. \tag{2.22}$$

Here, $k = D/\delta$ is the boundary layer mass transfer coefficient and will be introduced in section 2.2.2. Like $c_{\mathrm{D,m}}$, $c_{\mathrm{F,m}}$ consists of two terms: The bulk concentration that is corrected by external concentration polarization and an increase in salt concentration due to reverse salt permeation across the active layer.

It is impractical to measure $c_{\mathrm{D,m}}$ and $c_{\mathrm{F,m}}$ in experiments. Hence, $c_{\mathrm{F,m}}$ is subtracted from $c_{\mathrm{D,m}}$

$$c_{\mathrm{D,m}} - c_{\mathrm{F,m}} = \frac{c_{\mathrm{D,SL}} \exp\left(-\frac{j_W\ S}{D}\right) - c_{\mathrm{F,b}} \exp\left(\frac{j_W}{k}\right)}{1 + \frac{B}{j_W}\left[\exp\left(\frac{j_W}{k}\right) - \exp\left(-\frac{j_W\ S}{D}\right)\right]}. \tag{2.23}$$

The next step neglects the ECP in the draw channel ($\Pi_{D,SL} \approx \Pi_{D,b}$) and applies the van't Hoff equation (cf. Eq. 2.13). The permeate water flux can then be calculated by combining equation 2.14 and 2.23:

$$j_W = K \left\{ \frac{\pi_{D,b} \exp\left(-\frac{j_W S}{D}\right) - \pi_{F,b} \exp\left(\frac{j_W}{k}\right)}{1 + \frac{B}{j_W}\left[\exp\left(\frac{j_W}{k}\right) - \exp\left(-\frac{j_W S}{D}\right)\right]} \right\}. \tag{2.24}$$

The combination of equation 2.15 and 2.23 leads to the reverse salt flux in FO

$$j_S = B \left\{ \frac{c_{D,b} \exp\left(-\frac{j_W S}{D}\right) - c_{F,b} \exp\left(\frac{j_W}{k}\right)}{1 + \frac{B}{j_W}\left[\exp\left(\frac{j_W}{k}\right) - \exp\left(-\frac{j_W S}{D}\right)\right]} \right\}. \tag{2.25}$$

Both equations, j_W and j_S, use parameters that can be determined with experiments and take into account ICP, ECP on the feed side, and reverse salt flux.

2.2.2 Hydrodynamics in Spacer-Filled Channels

A spacer separates the membrane sheets in an SWM and significantly influences the mass transfer within the module. Although the main purpose of the spacer is the stabilization of the feed and the draw channel, the spacer also promotes mixing within the channel which reduces ECP. The following section will discuss the calculation of characteristic numbers, such as Reynolds number Re and mass transfer coefficient k, for the flow and mass transfer in a spacer-filled channel.

The spacer has to be considered when calculating the Reynolds number. Schock and Miquel [51] characterized spacers by their porosity ε, volume specific surface area $A_{V,SP}$ and the channel height h:

$$d_{\mathrm{h}} = \frac{4\ \varepsilon}{\frac{2}{h} + (1-\varepsilon)\ A_{\mathrm{V,SP}}}. \tag{2.26}$$

Here, d_{h} is the hydraulic diameter. The crossflow velocity u can be calculated as the ratio of volume flow $\dot{V}$ to the product of cross sectional area A of the channel and ε:

$$u = \frac{\dot{V}}{\varepsilon\ A}. \tag{2.27}$$

The Reynolds number of a spacer-filled channel is

$$\mathrm{Re} = \frac{u\ d_{\mathrm{h}}}{\nu}, \tag{2.28}$$

where ν denotes the kinematic viscosity of the fluid. In rectangular channels with spacers, the Sherwood number Sh can be calculated as [52]

$$\mathrm{Sh} = 0.46\ \left(\frac{u\ d_{\mathrm{h}}}{D}\right)^{0.36}. \tag{2.29}$$

The boundary layer mass transfer coefficient k was defined as the ratio of diffusivity to boundary layer thickness in section 2.2.1. In spacer-filled channels, k can be approximated as [52]

$$k = \frac{\mathrm{Sh}\ D}{d_{\mathrm{h}}}. \tag{2.30}$$

2.2.3 Membrane

Considerable research effort has been invested in improving membrane properties. The semi-permeable membrane needs to have a high permeability for the solvent but a low permeability for the solute. Biofouling can

be treated with chlorine. Hence, high membrane resistance to chlorine is advantageous.

In general, the support layer of FO membranes is thin. Membranes do not have to withstand high hydraulic pressures and a thick support layer leads to high ICP. The most common membrane types in FO are cellulose triacetate (CTA) and thin-film composite membranes (TFC).

The permeability of CTA membranes is lower than of TFC membranes [53]. TFC membranes feature two layers, an active layer and the support layer. The support is made of polysulfone or polyethersulfone [53]. Both polymers are known for chemical and mechanical resistance [54]. The most common material for the active layer of TFC membranes is polyamide [53]. Experiments within this thesis were conducted with TFC membranes.

2.2.4 Draw Solution

The draw solution has to be selected while regarding the application, which is an efficient way of extracting water from the feed solution. Multiple draw solutions are possible when treating wastewater with FO and several factors need to be considered. The solution should [55]

- provide a high osmotic pressure,
- have a high diffusivity to lower ICP,
- have a low reverse salt flux,
- not be toxic,
- be cheap.

Draw solutes can be divided into three groups: gases and volatile compounds, organic and inorganic draw solutes.

Inorganic draw solutes are the most common. Monovalent species such as sodium chloride provide high osmotic pressure, are cheap, not toxic, and

can be re-concentrated by RO. However, the salt permeability of membranes is relatively high [55]. A high salt permeability leads to a high internal concentration polarization and thus less permeate water flux across the membrane (cf. Eq. 2.24).

Ammonium bicarbonate (NH_4HCO_3) has previously been used as a draw solute [56] and is an example for gases and volatile compounds. NH_4HCO_3 has a high osmotic pressure but should not be used for drinking water production as NH_4HCO_3 could contaminate the polished water in the regeneration step.

Although the negative effect of ICP was severely reduced by the introduction of TFC membranes, reverse salt flux and ICP are still issues in FO. Hence, recent research has focused on Polyelectrolytes [57], hydrogels [58], stimuli-responsive polymers [59], and nanoparticles coated with hydrophilic groups [60]. These large particles lead to less reverse flux and ICP, but provide less osmotic pressure, and are not as available as monovalent ions.

2.3 Particle Deposition

The scope of this dissertation is the initial stage of cake layer formation. Understanding the process of particle deposition is crucial during this initial stage. Particle deposition will be modeled in Chapter 4 for polystyrene beads instead of *Bacillus subtilis* for simplification purposes. As *Bacillus subtilis* are rod shaped instead of spherical, modeling would be more complicated. The developed simulation tool uses the fundamentals introduced in this section. Newton's second law states that the time derivative of the linear momentum of a particle with mass m_p has to be equal to the sum of forces acting on that particle

$$m_\mathrm{p} \frac{\mathrm{d}\vec{u}_\mathrm{p}}{\mathrm{d}t} = \sum_j \vec{F}_j. \tag{2.31}$$

Here, $\vec{u}_\mathrm{p}$ is the velocity of the particle. The forces can be categorized into

two groups: volume forces $\vec{F}_\mathrm{V}$ and surface forces $\vec{F}_\mathrm{S}$. Volume forces $\vec{F}_\mathrm{V}$ are independent of the flow field, while surface forces $\vec{F}_\mathrm{S}$ are not

$$m_\mathrm{p}\frac{\mathrm{d}\vec{u}_\mathrm{p}}{\mathrm{d}t} = \sum_j \vec{F}_{\mathrm{V},j} + \sum_k \vec{F}_{\mathrm{S},k}. \tag{2.32}$$

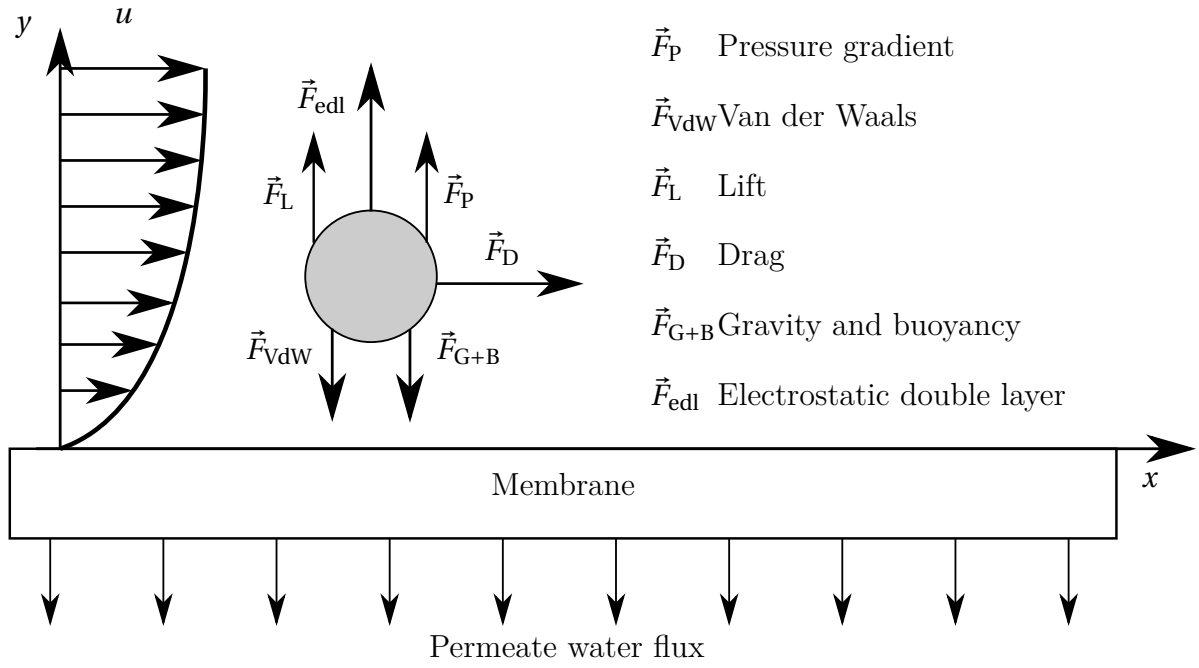

Figure 2.4: Illustration of the relevant particle forces in FO.

A particle experiences several forces in FO (cf. Fig. 2.4). Considering a steady-state flow, the most significant of those forces are the gravitational force $\vec{F}_\mathrm{G+B}$, lift force $\vec{F}_\mathrm{L}$, van der Waals force $\vec{F}_\mathrm{VdW}$, electric double layer force $\vec{F}_\mathrm{edl}$, steady-state drag $\vec{F}_\mathrm{D}$, and the fluid force on a particle from the pressure gradient $\vec{F}_\mathrm{P}$ [61]

$$m_\mathrm{p}\frac{\mathrm{d}\vec{u}_\mathrm{p}}{\mathrm{d}t} \approx \underbrace{\vec{F}_\mathrm{G+B} + \vec{F}_\mathrm{VdW} + \vec{F}_\mathrm{edl}}_{\vec{F}_\mathrm{V}} + \underbrace{\vec{F}_\mathrm{P} + \vec{F}_\mathrm{L} + \vec{F}_\mathrm{D}}_{\vec{F}_\mathrm{S}}. \tag{2.33}$$

The virtual mass force and basset force depend on the relative acceleration

of the particle to the continuous phase and are only significant in transient flows [62,63]. Hence, they were neglected. In the bulk of the fluid, the dominating particle force is the drag force $\vec{F}_{\mathrm{D}}$ [45]. Forces such as van der Waals $\vec{F}_{\mathrm{VdW}}$ and the electrostatic double layer force $\vec{F}_{\mathrm{edl}}$ are only relevant in close proximity to the membrane. However, studies have suggested that these forces play an important role in particle deposition [34,64,65]. These forces were thus included in the particle model. The following section discusses the physical background and common modeling approaches for each of these forces, Brownian motion, and particle attachment.

2.3.1 Volume Forces

Gravity and Buoyancy

Particles settle due to a difference in buoyancy and gravitation:

$$\vec{F}_{\mathrm{G+B}} = m_{\mathrm{p}}\vec{g}\left(1 - \frac{\rho_{\mathrm{f}}}{\rho_{\mathrm{p}}}\right). \tag{2.34}$$

Here, ρ_{f} is the density of the fluid, while ρ_{p} is the density of the particle. $\vec{F}_{\mathrm{G+B}}$ shows a dependency on the cube of the particle size d_{p}^3. Colloidal particles are particles with a diameter d_{p} below 1 µm, while suspended particles are defined as particles with diameters above 1 µm. Colloidal particles remain in a dispersed state for a long time, while suspended particles are removed quickly by sedimentation [66].

Van der Waals Force

Ions move randomly in an electrolyte solution. The random motion leads to a temporarily non-uniform electron distribution in molecules and atoms. This effect of uneven electron distribution is called a statistic dipole. The uneven electron distribution in molecules and atoms induces uneven distribution in nearby atoms. Hence, statistic dipoles propagate through the

solution until another dipole interferes and hinders the progress. Attracting atoms face each other. Therefore, the van der Waals force $\vec{F}_{\mathrm{VdW}}$ is an attractive force between atoms, molecules, or colloidal particles.

Hamaker [67] obtained the van der Waals potential energy between a spherical particle and a flat plate and introduced the Hamaker constant H. Hamaker assumed vacuum conditions in his derivations. In membrane processes, a particle is surrounded by a fluid. The statistic dipoles of a fluid interact with the atoms in a particle and should be taken into account [68]. Visser et al. [68] adjusted the Hamaker constant to consider the fluid:

$$H_{\mathrm{pfm}} \approx \left(\sqrt{H_{\mathrm{p}}} - \sqrt{H_{\mathrm{f}}}\right)\ \left(\sqrt{H_{\mathrm{m}}} - \sqrt{H_{\mathrm{f}}}\right). \tag{2.35}$$

H_{p} is the Hamaker constant of a particle, H_{f} the Hamaker constant of the fluid, and H_{m} the Hamaker constant of the membrane.

Furthermore, Hamaker's model does not consider the finite propagation time of the underlying electromagnetic interactions which evoke retardation effects. Gregory et al. [69] extended the model of Hamaker to include retardation effects into the van der Waals potential energy ϕ_{VdW}:

$$\phi_{\mathrm{vdW}} = -\frac{H_{\mathrm{pfm}}\ d_{\mathrm{p}}}{12\ R}\left(\frac{1}{1+14\frac{R}{\lambda}}\right). \tag{2.36}$$

The retardation effects are significant at large distances between particle and plate. Here, R is the distance of the particle to the nearest wall. λ is the characteristic wavelength of the the London dispersion force and is often assumed as 100 nm [69]. The van der Waals force $\vec{F}_{\mathrm{VdW}}$ can be calculated by differentiating the potential energy ϕ_{vdW} by R [4]:

$$F_{\mathrm{vdW}} = -\frac{H_{\mathrm{pfm}}\ d_p}{12\ R\left(1+14\frac{R}{\lambda}\right)}\left(\frac{1}{R} + \frac{14}{\lambda + 14\ R}\right). \tag{2.37}$$

Electrostatic Double Layer Force

The electrostatic double layer force $\vec{F}_{\mathrm{edl}}$ represents the interaction of two charged bodies within an electrolyte solution. If both bodies are charged in the same way, $\vec{F}_{\mathrm{edl}}$ is a repelling force and counteracts the van der Waals force $\vec{F}_{\mathrm{VdW}}$. The surface charge arises from uncoordinated bonds on the surface of the particle or from material-specific covalently bound functional groups. The ions within the electrolyte solution assemble around the charged surfaces, which changes the ideal exponential decay of the surface potential within the solution [1].

Helmholtz [70] postulated a loose bond between solvated ions, which is called Helmholtz Layer, and a surface. He neglected the thermal mobility of the electrolyte solution. Guoy-Champan [71,72] proposed that ions form a diffuse cloud. Ions with opposing charges to the surface are closer to the surface than ions with the same charge. Stern [73] combined the Helmholtz Layer with the theory of Guoy-Champan. In his theory, solvated ions are bound to the charged surface. Additionally, he proposed a diffuse cloud of ions close to the surface. This ion cloud leads to a gradual transition from surface potential to solution potential.

In Stern's Model, the potential energy ϕ_{edl} of a particle with surface potential ψ_{p} that approaches a charged flat surface with surface potential ψ_{m} can be calculated as

$$\phi_{\mathrm{edl}} = \frac{\pi}{2}\epsilon_0\epsilon_{\mathrm{r}} d_{\mathrm{p}} \left\{ 2\psi_{\mathrm{p}}\psi_{\mathrm{m}} \ln\left[\frac{1+\exp\left(-\kappa_{\mathrm{D}}R\right)}{1-\exp\left(-\kappa_{\mathrm{D}}R\right)}\right] + \left(\psi_{\mathrm{p}}^2+\psi_{\mathrm{m}}^2\right)\ln\left[1-\exp\left(-2\kappa_{\mathrm{D}}R\right)\right] \right\}. \tag{2.38}$$

Here, κ_{D} is the inverse Debye length

$$\kappa_{\mathrm{D}} = \sqrt{\frac{e^2\sum_j n_j z_j^2}{\epsilon_0\epsilon_{\mathrm{r}} k_{\mathrm{B}} T}}. \tag{2.39}$$

The variable z_j is the valency of ion j, n_j the mole number, k_B the Boltzmann constant, e the elementary charge, ϵ_0 the vacuum permittivity, and ϵ_r the relative permittivity [74]. The electrostatic double layer force $\vec{F}_\mathrm{edl}$ can be derived by differentiating the potential energy ϕ_edl by R [4]:

$$\vec{F}_\mathrm{edl} = \frac{\pi\ \epsilon_0\ \epsilon_\mathrm{R}\ d_\mathrm{p}\ \kappa_\mathrm{D}\ \exp(-\kappa_\mathrm{D}\ R)}{1-\exp(-2\ \kappa_\mathrm{D}\ R)} \left\{2\ \psi_\mathrm{p}\ \psi_\mathrm{m} - (\psi_\mathrm{p}^2 + \psi_\mathrm{m}^2)\ \exp(-\kappa_\mathrm{D}\ R)\right\}. \tag{2.40}$$

2.3.2 Surface Forces

Pressure Gradient

The pressure gradient imparts a force $\vec{F}_\mathrm{P}$ on a particle, which is directed the same way as the pressure gradient [61]. For a spherical particle, the force can be expressed as

$$\vec{F}_\mathrm{P} = -\frac{\pi\ d_\mathrm{p}^3}{6}\ \nabla p. \tag{2.41}$$

Steady-State Drag Force

Steady-state drag acts on a particle in a velocity field when there is no acceleration between the particle and surrounding fluid. For a sphere in a flow, the steady-state drag is [61]

$$\vec{F}_\mathrm{D} = 3\pi d_\mathrm{p} \eta_\mathrm{f} C_\mathrm{D}\ \left(\vec{u}_\mathrm{f} - \vec{u}_\mathrm{p}\right). \tag{2.42}$$

The drag coefficient C_D depends on the relative Reynolds number Re_r which is based on the difference of velocity of a particle to the velocity of the surrounding fluid

$$\mathrm{Re}_\mathrm{r} = \frac{d_\mathrm{p}}{\nu_\mathrm{f}} |\vec{u}_\mathrm{f} - \vec{u}_\mathrm{p}|. \tag{2.43}$$

At low relative Reynolds numbers ($\mathrm{Re}_\mathrm{r} < 1$) the drag coefficient varies inversely with Re_r. This regime is called Stoke's flow regime. When Re_r is further increased, the drag coefficient becomes independent of the relative Reynolds number. This stage is called Newton's Regime.

Putnam [75] derived an equation that is suitable for a wide range of relative Reynolds numbers:

$$C_\mathrm{D} = \begin{cases} 1 + \frac{1}{6}\ \mathrm{Re}_\mathrm{r}^{\frac{2}{3}} & \text{if } \mathrm{Re}_\mathrm{r} \leq 1000 \\ 0.0183\ \mathrm{Re}_\mathrm{r} & \text{if } \mathrm{Re}_\mathrm{r} > 1000. \end{cases} \tag{2.44}$$

Lift Force

Fluid velocities decrease from the fluid bulk to the membrane surface due to fluid friction. The side of the particle that faces away from the membrane experiences a higher velocity and thus lower pressure than the other side. The resulting pressure difference between both sides then forces the particle away from the membrane.

Saffman [76] proposed a model to calculate the lift force $\vec{F}_\mathrm{L}$. The model is limited to cases where the relative Reynolds number Re_r is far smaller than the square root of the shear Reynolds number Re_G and both are smaller than unity. The shear Reynolds number is

$$\mathrm{Re}_\mathrm{G} = \frac{d_\mathrm{p}^2}{\nu_\mathrm{f}} |\nabla \times \vec{u}_\mathrm{f}|. \tag{2.45}$$

McLaughlin [77] investigated flows with Re_G above unity and found that the lift force decreases rapidly. Saffman's prediction would overestimate the actual lift force. Mei [78] combined the equations of Saffman and McLaughlin into

$$\vec{F}_{\mathrm{L}} = 1.61\ C_{\mathrm{L}} \sqrt{\frac{\eta_{\mathrm{f}}\ \rho_{\mathrm{f}}}{|\nabla \times \vec{u}_{\mathrm{f}}|}}\ d_{\mathrm{p}}^{2}\ (\vec{u}_{\mathrm{f}} - \vec{u}_{\mathrm{p}}) \times (\nabla \times \vec{u}_{\mathrm{f}}). \tag{2.46}$$

Here, C_{L} is the lift force coefficient:

$$C_{\mathrm{L}} = \begin{cases} \left(1 - 0.3314\beta^{0.5}\right) \exp\left(-\frac{\mathrm{Re}_{\mathrm{r}}}{10}\right) + 0.3314\beta^{0.5} & \text{if } \mathrm{Re}_{\mathrm{r}} \leq 40 \\ 0.0524\sqrt{\beta\,\mathrm{Re}_{\mathrm{r}}} & \text{if } \mathrm{Re}_{\mathrm{r}} > 40 \end{cases}. \tag{2.47}$$

The variable β is defined as

$$\beta = \frac{d_{\mathrm{p}}}{2|\vec{u}_{\mathrm{f}} - \vec{u}_{\mathrm{p}}|} |\nabla \times \vec{u}_{\mathrm{f}}|. \tag{2.48}$$

2.3.3 Brownian Motion

The movement of a particle in a fluid is affected by the molecular motion of the fluid. Molecules randomly collide with the particle and force a movement. This is called Brownian motion. When the concentration of particles is not uniform within the fluid, particles will migrate toward regions with low concentrations because of Brownian motion. While this diffusion is negligible for particles that are larger than 1 µm, it becomes increasingly important as the particle diameter decreases [61].

2.3.4 Particle Attachment

Colloidal forces dominate the near-wall behavior of a particle. Irreversible and reversible attachment can be explained by the total potential energy. The Derjaguin Landau Verweey Overbeek (DLVO) theory [79, 80] states that the total potential energy ϕ is the sum of the van der Waals potential energy ϕ_{VdW} and the electrostatic double layer potential energy ϕ_{edl}.

When a particle approaches the membrane, the absolute value of ϕ_{VdW} and ϕ_{edl} increase with a decrease in distance R (cf. Fig. 2.5a). The total poten-

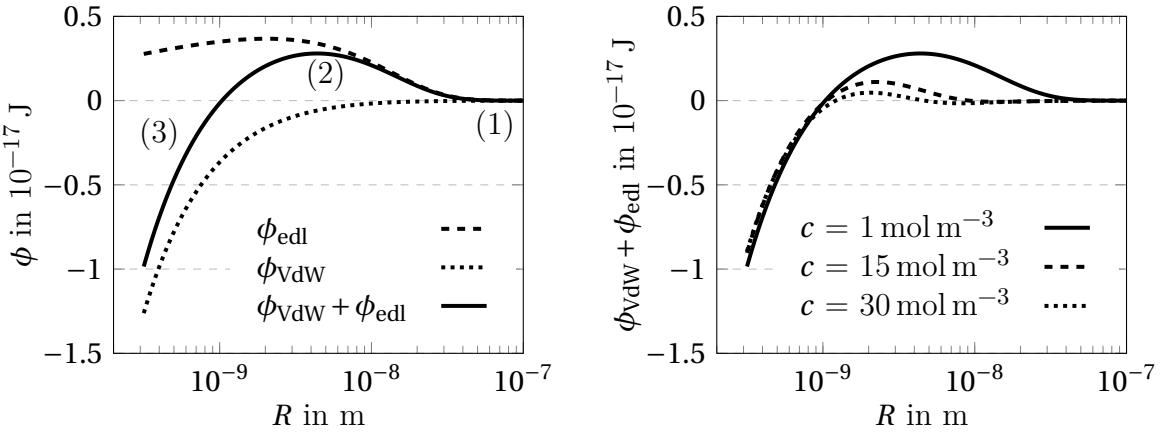

(a) Electrostatic double layer ϕ_{edl}, van der Waals ϕ_{VdW}, and total potential energy $\phi_{VdW} + \phi_{edl}$ as a function of R.

(b) Total potential energy $\phi_{VdW} + \phi_{edl}$ as a function of R for several molar sodium chloride concentrations c in the fluid.

Figure 2.5: Near wall interaction of a particle.

tial energy $\phi_{VdW} + \phi_{edl}$ has a maximum and two minima. When a particle comes closer to the membrane surface, $\phi_{VdW} + \phi_{edl}$ reaches a first minimum (1). Here, the attractive van der Waals force is greater than the repulsive electrostatic double layer force. This state is called reversible attachment. The energetic barrier (2) separates reversible (1) from irreversible attachment (3). It is called an energetic barrier, as a particle must possess enough kinetic energy to reach the maximum of $\phi_{VdW} + \phi_{edl}$. Once a particle has passed the energetic barrier, the particle falls into the primary minimum (3). The primary minimum corresponds to an irreversible attachment on the membrane surface [1]. In the CFD simulation, a particle is considered to have deposited once it touches the membrane.

Hydrodynamics affect the ion concentration close to the membrane surface in FO. The influence of the ion concentration in the fluid on the energetic barrier is significant. Figure 2.5b depicts the total potential energy $\phi_{VdW} + \phi_{edl}$ over distance R to the membrane for several sodium chloride concentrations c in the surrounding fluid. With an increase in concentration c, the energetic barrier between reversible and irreversible attachment decreases. A particle that approaches the membrane would require less kinetic energy for irreversible attachment. Hence, an increase in sodium

chloride concentration c increases the probability of particle attachment.

3 Impact of Steady-State Hydrodynamics on the First Stages of Biofilm Formation

The first research aim of the dissertation is the investigation of the impact of steady-state hydrodynamics on cake layer formation in forward osmosis (FO) spiral-wound modules (SWM). The deposition was investigated on a laboratory scale. Subsequently, Chapter 6 applies the results to a system model with an SWM to meet the steady-state research aim.

This chapter covers the laboratory-scale investigation. The impact of steady-state hydrodynamics on the first stages of biofilm formation is quantified. Dynamic biofouling experiments are conducted with *Bacillus subtilis* as a biofilm-forming model organism. High-resolution large field fluorescence microscopy captures spatio-temporal patterns of bacterial deposition. A newly developed image analysis procedure and flow cytometry quantify deposition results. Concomitantly, flow paths of bacteria through the feed channel are captured in real-time, following the inoculation of the FO system. The results indicate that a decrease in the ratio of permeate water flux to crossflow velocity leads to less deposition as well as a heterogeneous distribution of deposited cells within a spacer element. This chapter is a modified version of Kastl et al. [81].

3.1 Materials and Methods

The materials and methods section discusses the experimental FO system and the protocol of procedure. Subsequently, the bacterial strain, growth conditions, and the measurement of the cell count are discussed. Intro-

ducing the methodology includes image acquisition, image analysis, and examining the biofilm on membrane probes with flow cytometry.

3.1.1 Experimental Forward Osmosis Setup

Experiments were conducted in a bench-scale FO membrane system with spacers (cf. Fig. 3.1a). Fluorescent bacteria in the feed channel were visu-

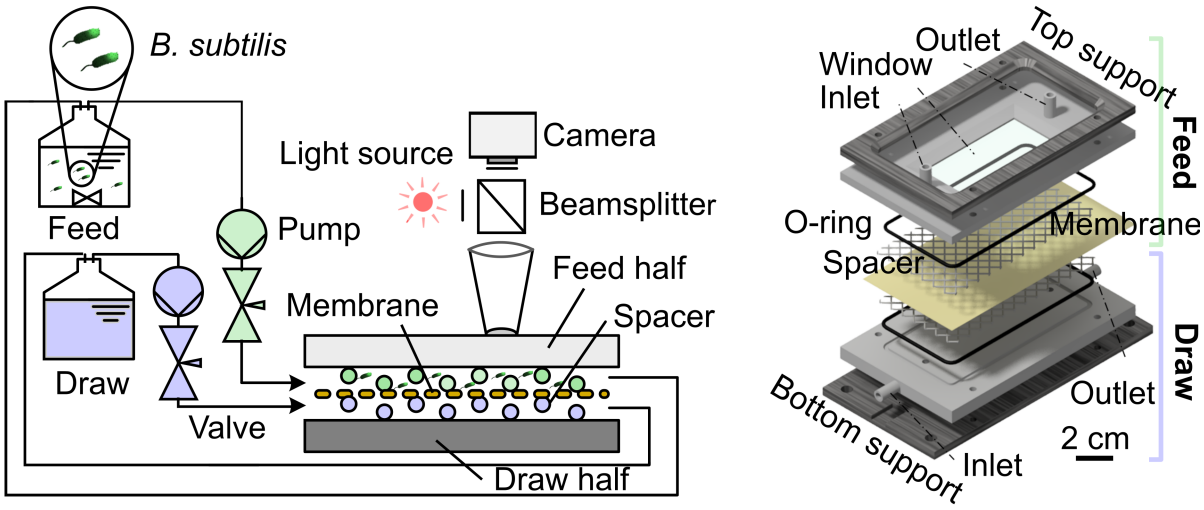

(a) Schematic drawing of the bench-scale FO system with a cross-sectional view of the flow cell and spacers.

(b) 3D printed flow cell and corresponding components.

Figure 3.1: Bench-scale FO system and 3D printed flow cell.

alized in situ and in realtime using a large field high-resolution epifluorescence microscope equipped with an Axiocam 506 monocamera. Centrifugal pumps[1] combined with needle valves[2] were used to set the crossflow rates. The crossflow velocities were continuously controlled by volumetric flow measurements. The water temperature of the FO system was held constant at 25 ± 0.5 °C. The 3D printed crossflow cell[3] consisted of four elements: support plates on the bottom and top and feed and draw halves

[1]Centrifugal pumps: Atman, China.
[2]Needle valves: Ham-Let, Israel.
[3]3D printed crossflow cell: Shapeways, USA.

(cf. Fig. 3.1b). A microscopic slide[4] sealed the view hole in the feed half. Feed and draw halves were made of acrylic photopolymer[5]. The O-rings set the membrane area[6] and the spacer[7] set the channel height. The spacer was diamond-shaped and contained two layers of polypropylene filaments. The thin-film composite FO membrane[8] was stored at 4 °C in 1 % $NaHSO_3$ solution and thoroughly washed by double distilled water (DDW) before use. Permeate water flux and reverse salt flux were $33 \pm 2\,\mathrm{L\,m^{-2}\,h^{-1}}$ and $0.60 \pm 0.1\,\mathrm{g\,L^{-1}}$, respectively, at $1 \times 10^3\,\mathrm{mol\,m^{-3}}$ NaCl draw solution and 25 °C. The contact angle of the active layer was approximately 70°.

3.1.2 Bacterial Strain and Growth Conditions

Bacillus subtilis with labeled green fluorescent protein[9] was used as a biofilm-forming model bacteria for all the experiments. *B. subtilis* are rod-shaped bacteria with an approximate size of 0.8 µm x 5 µm. *B. subtilis* form biofilms on various artificial surfaces as well as in soils and the human gut and are thus common model bacteria [42, 43]. *B. subtilis* were grown overnight (8—12 h) in Luria—Bertani broth (LB)[10], diluted, and regrown for less than 2 h to a mid-exponential state. Optical density (OD) was measured at a wavelength of 600 nm and controlled to a value of 0.5. After centrifugation at 4000 rpm for 20 min supernatant LB was removed and replaced with sterile artificial secondary effluent wastewater to re-suspend the bacteria [42].

3.1.3 Experimental Procedure

Experiments were conducted with combinations of low (LC: $1.3\,\mathrm{cm\,s^{-1}}$) and high (HC: $13.7\,\mathrm{cm\,s^{-1}}$) crossflow velocities. Additionally, the permeate wa-

[4]Microscopic slide: Menzel, Thermo Fisher, USA.
[5]Acrylic photopolymer: Visijet M3 Crystal, 3D Systems, USA.
[6]Membrane area: $7.9 \times 3.7\,\mathrm{cm^2}$.
[7]Spacer: 17 mils = 0.43 mm, Conwed, USA.
[8]FO membrane: FOMEM-0415, Porifera, USA.
[9]Labeled *Bacillus subtilis*: strain number 4846, ex. 470 nm, em. 525 nm.
[10]LB: Becton, Dickinson and Company.

ter flux was varied between low (LP: 5.6 ± 0.9 $\mathrm{L\,m^{-2}\,h^{-1}}$) and high (HP: 30 ± 3.6 $\mathrm{L\,m^{-2}\,h^{-1}}$) permeate water flux. These combinations resulted in four hydrodynamic configurations (cf. Fig. 3.2). The parameter σ was defined

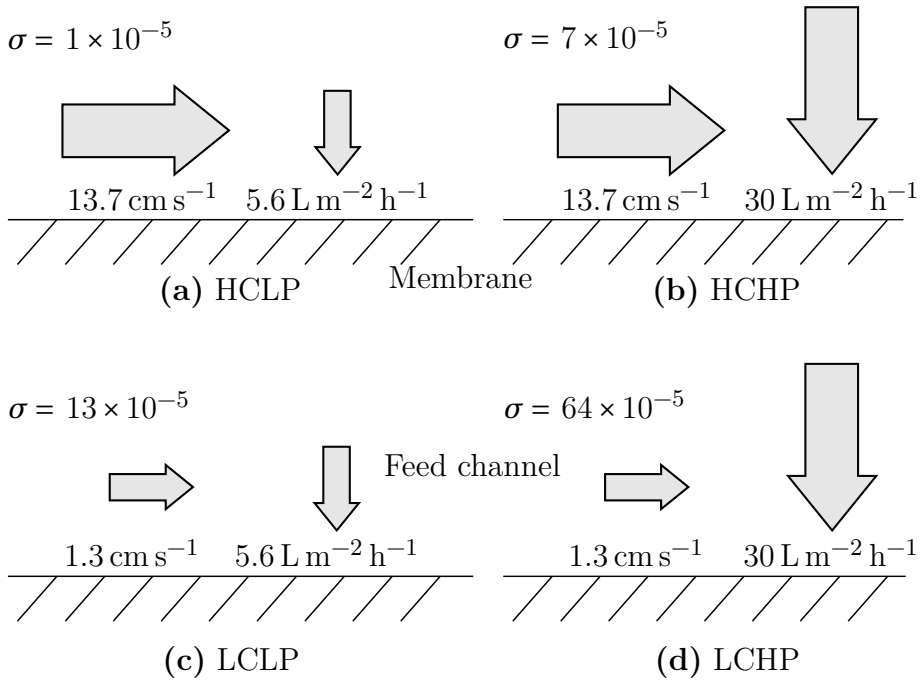

Figure 3.2: Schematic drawing of the four hydrodynamic conditions.

as the ratio of permeate water flux to crossflow velocity. The cleaning protocol before each experiment included a rinse with 10 % bleach for 10 min as well as two rinses for 30 min with double distilled water (DDW).

Air bubbles would distort the recorded images and were removed by running the FO system with DDW for up to 4 h. Feed solution properties have an impact on the deposition of bacteria. Experiments were thus initiated by adding 2 L sterile artificial secondary effluent wastewater [42, 82] to the feed tank[11]. Additionally, carbon source in the form of sodium citrate and glucose were added to the feed tank[12].

The permeate water flux was controlled by varying the molar concentration c_D in the draw solution (cf. Tab. 3.1). For this purpose, a predefined amount

[11]The feed solution then contained 8 $\mathrm{mol\,m^{-3}}$ NaCl, 0.15 $\mathrm{mol\,m^{-3}}$ $MgSO_4$, 0.5 $\mathrm{mol\,m^{-3}}$ $NaHCO_3$, 0.4 $\mathrm{mol\,m^{-3}}$ NH_4Cl, 0.2 $\mathrm{mol\,m^{-3}}$ $CaCl_2$, and 0.2 $\mathrm{mol\,m^{-3}}$ KH_2PO_4.
[12]Sodium citrate and glucose concentration: 0.6 $\mathrm{mol\,m^{-3}}$ $Na_3C_6H_5O_7$, 2.7 $\mathrm{mol\,m^{-3}}$ $C_6H_{12}O_6$.

Table 3.1: Sodium chloride concentration in the draw solution c_D and measured conductivity κ_C.

Short name	c_D	κ_C
HCHP	$720\,\mathrm{mol\,m^{-3}}$	$65 \pm 0.95\,\mathrm{mS\,cm^{-1}}$
HCLP	$50\,\mathrm{mol\,m^{-3}}$	$4.6 \pm 0.08\,\mathrm{mS\,cm^{-1}}$
LCHP	$970\,\mathrm{mol\,m^{-3}}$	$82 \pm 1.97\,\mathrm{mS\,cm^{-1}}$
LCLP	$60\,\mathrm{mol\,m^{-3}}$	$5.5 \pm 0.16\,\mathrm{mS\,cm^{-1}}$

of $5 \times 10^3\,\mathrm{mol\,m^{-3}}$ NaCl stock solution was added to the draw reservoir (8 L), and conductivity κ_C was measured[13]. Both feed and draw solutions were mixed for 15 min before *B. subtilis* was added to the feed solution in a concentration c_{BS} close to wastewater conditions ($2 \pm 0.5 \times 10^9\,\mathrm{cells\,L^{-1}}$). Feed samples were taken hourly to quantify total bacterial abundance with an Attune NxT flow cytometer (FCM)[14]. *B. subtilis* was counted with the FCM according to the green fluorescence[15] and side scatter of the bacteria (cf. Fig. 3.3).

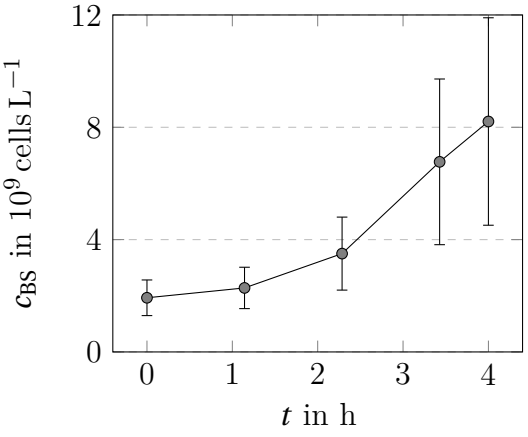

Figure 3.3: Concentration of *Bacillus subtilis* c_{BS} and standard deviation in feed reservoir over time t.

[13]Conductivity meter: Eutech Instruments, Thermo Scientific, USA.
[14]Attune NxT flow cytometer: Life Technologies, Thermo Fisher Scientific, USA
[15]Green fluorescence: excitation 488 nm, emission 530 ± 30 nm.

3.1.4 Image Acquisition

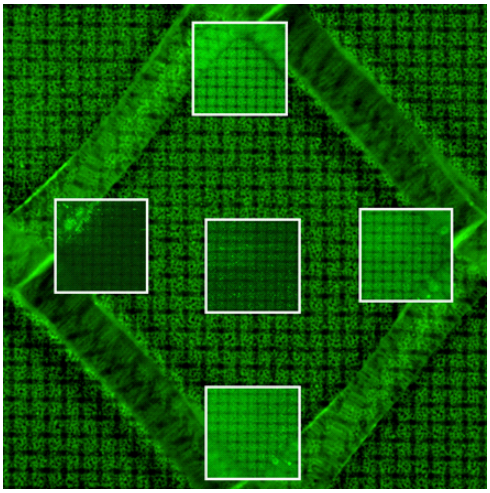

Figure 3.4: Locations of image acquisition for bacteria tracking: at the four spacer filament crossings and in the center of the spacer element.

The software ZEN[16] and an epifluorescence microscope[17] with a PanNeoFluar objective and an Axiocam 506 mono camera provided images of bacteria deposition. Two filters, excitation of 500/25 nm and emission of 535/30 nm, were used to visualize bacteria. One spacer element (approx. $1.5 \times 1.5\,\mathrm{mm}^2$) was captured at 20× magnification with the focus on the membrane surface. Images for deposition over time (4 h) were taken every 30 s. Movies for particle tracks were recorded for 30 s with a magnification of 60× and a frame rate of $10\,\mathrm{s}^{-1}$ at five different locations in the spacer element (cf. Fig. 3.4) at the beginning of each experiment.

3.1.5 Image Analysis

Recorded image series were exported from ZEN and analyzed in MATLAB. The area lying beneath the spacer filaments and outside of the observed spacer element was excluded. After background subtraction and thresh-

[16]Image analysis software: ZEN 2.6, Zeiss, Germany.
[17]Epifluorescence microscope: Axio Zoom, V16, Zeiss, Germany.

olding, clusters of connected pixels were determined, which were then separated into bacteria (5 pixels per bacteria) to obtain the bacteria count. Deposition patterns were quantified by splitting the area within the spacer element into nine regions (cf. Fig. 3.5). The bacteria tracking algorithm followed the position of identified bacteria from one time step to the next. These tracks were used to calculate the flow field, which included at least 150 tracks for each hydrodynamic configuration.

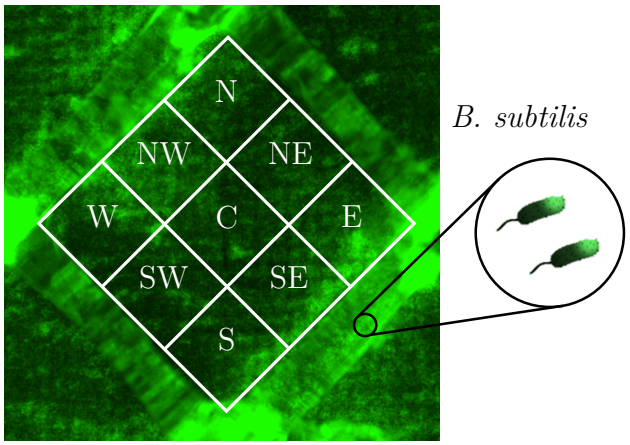

Figure 3.5: Separation of the membrane surface of one spacer element into nine regions.

3.1.6 Quantifying Deposited Cells with Flow Cytometry

The membrane was carefully removed from the flow cell after 4 h of biofouling experiment and cut into coupons of $2\,\mathrm{cm}^2$. These coupons were resuspended in sterile wastewater with $2.5\,\mathrm{mol\,m}^{-3}$ ethylenediaminetetraacetic acid (EDTA) and bath sonicated for 5 min to disperse all attached bacteria cells. The cell suspensions were diluted and analyzed in the FCM with a flow rate of $25\,\mu\mathrm{L\,min}^{-1}$. Staining of cells was not required for flow cytometry, as the green fluorescence protein was captured by a 530 nm (green emission) detector and side scatter with excitation wavelength 488 nm. Bacterial abundance was normalized to the sample surface area.

3.1.7 Statistical Analysis

Analysis of variance (ANOVA) with Fisher's least significant difference (LSD) procedure was performed with MATLAB. The significance level p was set to a value below 0.05. Significantly different groups were marked with signs (+, *, o). Correlations were tested with Pearson's correlation test at the same significance level p of below 0.05. The proportion of variance square R^2 was used as a goodness-of-fit measure. Time series of deposited particles were processed with spline smoothing to reduce artifacts between subsequent images.

3.2 Results and Discussion

The first section compares the applied methodology to approaches common in biofouling studies. The effects of permeate water flux on bacterial flow paths near the membrane surface are studied next. Then, the impact of permeate water flux and crossflow velocity on bacterial deposition and deposition patterns is investigated. Lastly, deposition beneath the spacer filaments is examined.

3.2.1 Discussion of the Applied Methodology

Fluorescence microscopy with a high resolution and a large field of view captured spatio-temporal deposition patterns and bacterial flow paths.

Contrary to conventional microscopy, the resolution of fluorescence microscopy is not a function of the magnification of the microscope but related to the amount of light that an object emits. Fluorescence microscopy made it possible to visualize single cells of *B. subtilis* while capturing two-dimensional information of a whole spacer element in one image. Concomitantly, the subtraction of the background was more straightforward than in conventional bright-field microscopy. A downside of the applied methodology is the need for fluorescent cells. Also, the methodology is lim-

ited to the initial biofilm formation stage. Multiple layers of biofilm can not be distinguished. Once a multi-layered biofilm has developed, other methods such as confocal laser scanning microscopy (CLSM) and optical coherence tomography (OCT) can resolve the three-dimensional structure. Both methods have their limits that justify the use of two-dimensional fluorescence microscopy in the present dissertation. CLSM is limited in field of view and frame-rate. OCT is an excellent option to capture large biofilms in the range of 10 to 1000 µm [83, 84]. Deposition studies reach this biofilm size typically over more than four hours [83, 85, 86]. Hence, OCT can not be used to quantify deposition at the initial stage of biofilm formation or track single cells.

Flow paths of cells were also tracked with fluorescence microscopy. The impact of biofilm formation on flow paths of cells could be monitored throughout the experiment. Particle image velocimetry has been used in a few membrane studies to quantify fluid flows in a spacer-filled channel [43,87,88]. Particle image velocimetry requires high frame-rates, a laser sheet for illumination, and a high concentration of particles. This high concentration of particles would affect the simultaneous deposition experiment. Other methods that might be able to quantify the fluid flow would require additional instruments and are not able to quantify deposition and flow paths at the same time [89–91].

3.2.2 Bacterial Flow Paths Near the Membrane Surface

Water flow enters and exits the spacer element close to the membrane (cf. Fig. 3.6a). Figures 3.6b-c depict the average flow paths of bacteria (n = 3 independent experiments) close to the membrane surface ($< 7\,\mu m$) at low crossflow velocity. The color scale represents bacterial velocities $\boldsymbol{u}$, while the arrows show the direction of the bacterial flow paths. Due to the low fluorescence of bacteria, movies had to be taken in five different locations within the spacer element (cf. Fig. 3.4).

During this early, yet critical, stage of biofilm formation the velocities of bacteria were up to $30\,\mu m\,s^{-1}$ under LCLP conditions (cf. Fig. 3.6b). Differ-

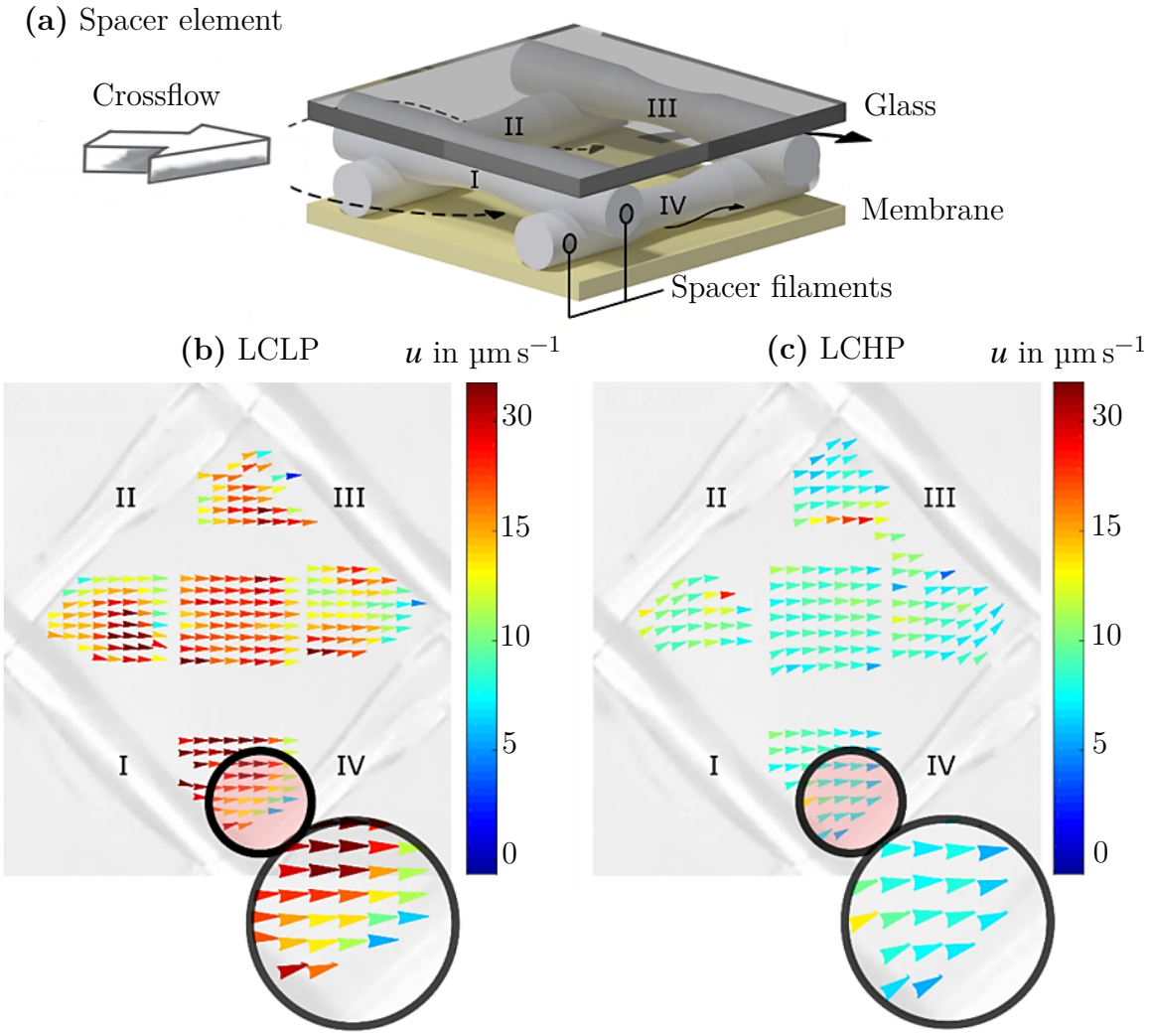

Figure 3.6: Three-dimensional view of the spacer element comprising filaments and calculated flow paths.

ently, bacterial velocities were much slower ($17\,\mu m\,s^{-1}$) at LCHP (cf. Fig. 3.6c). It should be noted that bacterial flow paths could not be determined at high crossflow velocity ($14\,cm\,s^{-1}$). Tracking bacteria under these conditions in real-time required high exposure times leading to a low frame rate ($< 10\,s^{-1}$) for image acquisition. These frame rates were not fast enough to distinguish between the different flow paths at the necessary resolution. Nonetheless, a higher crossflow velocity would likely result in higher bacterial velocities near the membrane surface [43]. Experiments with high

permeate water flux and low crossflow velocity (LCHP) resulted in enhanced pressure drop along the feed channel. Hence crossflow had to be readjusted immediately (approx. 10 min) after inoculating the feedwater. The immediate effects of bacteria deposition on membrane and spacer surfaces might have reduced the crossflow velocity at LCHP conditions. This reduction was more acute under LCHP than LCLP since bacteria cells were forced closer to the membrane with the increased permeate water flux. The mobility of these cells is often slower compared to those further away due to the difference in wall and fluid shear in a laminar velocity profile ($Re < 10$) [87]. Thus, the average velocity of all tracked cells was lower by 2-fold at LCHP in comparison to LCLP (cf. Fig. 3.6c).

After inoculation at LCLP, it was observed that most bacteria entered the spacer element under filament I and filament II. Concurrently, bacterial cells were captured exiting the spacer element under filament III and sporadically under the small gap between filament IV and the membrane (cf. Movie 3.1[18]). However, no bacteria were found entering or exiting beneath filaments II and IV at LCHP, which indicates that the gap was clogged, most likely by attached cells. Hence, an increase in the ratio between the drag and lift forces prompted irreversible attachment of cells to the membrane surface, as previously reported [41]. Concomitantly, higher permeate water flux also intensifies concentration polarization, which raises not only ion concentration but also nutrient and carbon concentration close to the membrane [92, 93]. Consequentially, it is possible that more bacteria will move toward the membrane surface via chemotaxis responses, which increases the probability of initial contact [92]. Attached bacteria that proliferated on the membrane surface secrete extracellular polymeric substance (EPS), which further hindered the flow path through the spacer element. Notably, under LCHP conditions, high numbers of bacteria deposited and grew on the membrane underneath filaments II and IV, thus blocking the small gap between these filaments and the membrane. Differently, this blockage did not occur under LCLP conditions during these early stages (4 h) of biofilm formation.

[18]**Movie 3.1:** Continuous observation of bacteria near membrane surface at LCHP and LCLP: `https://pubs.acs.org/doi/suppl/10.1021/acs.est.0c00380/suppl_file/es0c00380_si_001.avi`

Zooming into bacteria flow paths (cf. enlargement Fig. 3.6b) provided indications that the spacer filaments had little effect on the direction of planktonic bacteria at LCLP. Contrarily, the bacteria flow paths were often aligned with the spacer filament orientation under LCHP conditions (cf. enlargement Fig. 3.6c). Nonetheless, suspended bacteria followed the general flow direction in the center of the spacer element ($> 300\,\mu m$ distance to the filaments) regardless of the hydrodynamic conditions (cf. Fig. 3.6b-c). The area affected by flow perturbations induced by spacer filaments narrows with decreasing Reynolds number [43]. Previous studies considered Reynolds numbers greater than 70 [35, 43, 91], which is higher than the Reynolds number of 6.7 that was calculated for the present setup. Here, the water flow reattachment point after the recirculation zone was closer to the spacer filaments. The flow paths were aligned with the general flow direction for most of the spacer element. Hence, the general direction of the crossflow velocity had more impact on the flow paths of particles than previously reported [35, 43, 91].

3.2.3 Average Deposition

Bacterial cell accumulation on the membrane surface was quantified by large field, high-resolution epifluorescence microscopy at 30 s intervals. Figure 3.7 shows example images of initial biofilm formation after four hours of the experiment.

Figure 3.8 depicts the time-variant average bacterial abundance BA for the four different hydrodynamic configurations. Statistical analysis with ANOVA at a significance level of $p < 0.05$ resulted in three distinct groups (*, o, +) after four hours. Regardless of the hydrodynamic conditions, bacterial abundance BA on the membrane was low ($< 150\,\text{cells}\,\text{mm}^{-2}$) during the first 2 h and rapidly increased for the next 2 h. At the end of the experiments (4 h), clear and significant bacterial abundance differences were found between the four hydrodynamic conditions. Bacterial numbers were more than 5-fold higher at LCHP than at other hydrodynamic conditions. LCLP was 2-fold higher than HCHP, while the lowest number (<

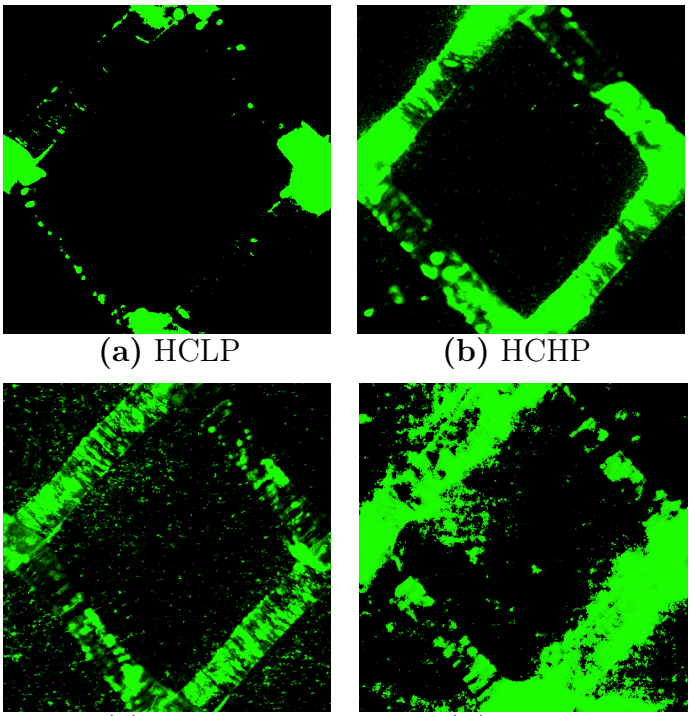

(a) HCLP **(b)** HCHP

(c) LCLP **(d)** LCHP

Figure 3.7: Example images of initial biofilm formation after 4 hours of the experiment.

100 cells mm^{-2}) of bacteria attached at HCLP after 4 h of constant flow.

Bacteria deposited exponentially between 2.3 and 3 h and linearly between 3 and 4 h at LCHP, which differs from the other hydrodynamic conditions. The exponential increase in deposition after 2.3 h was partly due to bacterial proliferation in the feed solution (cf. Fig. 3.3) and on the membrane surface [94]. Excess of nutrients due to concentration polarization could have expedited growth on the membrane surface between 2.3 and 3 h. However, over time, nutrient consumption may have consequently hindered growth, leading to a linear growth rate on the membrane surface at later stages. Both growth and nutrient consumption do not apply for fouling systems with inert beads [32, 33, 35] and emphasize the need for using bacteria to determine the impact of hydrodynamics on biofilm formation.

Bacterial abundance BA showed a strong linear correlation ($R^2 = 0.98$, $p < 0.05$) with the ratio σ of permeate water flux j_W to crossflow velocity u_F

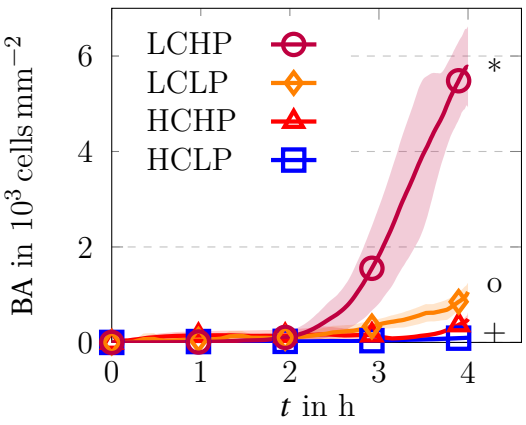

Figure 3.8: Average bacterial abundance BA over duration t of the experiment.

(cf. Fig. 3.9a-d). At each time step after t = 2.3 h, the relation between BA and σ can be approximated as linear (cf. Fig. 3.9e). The linear coefficients for the correlation between BA and σ change over time at the different hydrodynamic conditions. Hence, both time t and ratio σ of permeate water flux over crossflow velocity affect BA.

The deposition results with *B. subtilis* indicate that permeate water flux and crossflow velocity counteract each other. The bacterial velocity perpendicular to the membrane surface depends on the crossflow velocity due to lift forces away from the membrane and drag forces of the permeate water flux toward the membrane surface (cf. Sec. 2.3.2). The influence of permeation drag and crossflow velocity can be assumed to be independent of the Gram type, or species [93, 95]. Although the flow cell was equipped with a spacer, there was a linear correlation between BA and the ratio of permeate water flux to crossflow velocity σ (cf. Fig. 3.9d). Hence, the velocity component perpendicular to the membrane caused the variation in deposition results.

Different to inert beads [32,35,93], additional factors apply here that would only influence the deposition of bacteria. Higher ratios between permeate water flux and crossflow velocity also lead to increased concentration polarization of nutrients at the membrane surface [92]. A higher concentration of nutrients has two possible implications on bacterial accumulation. First,

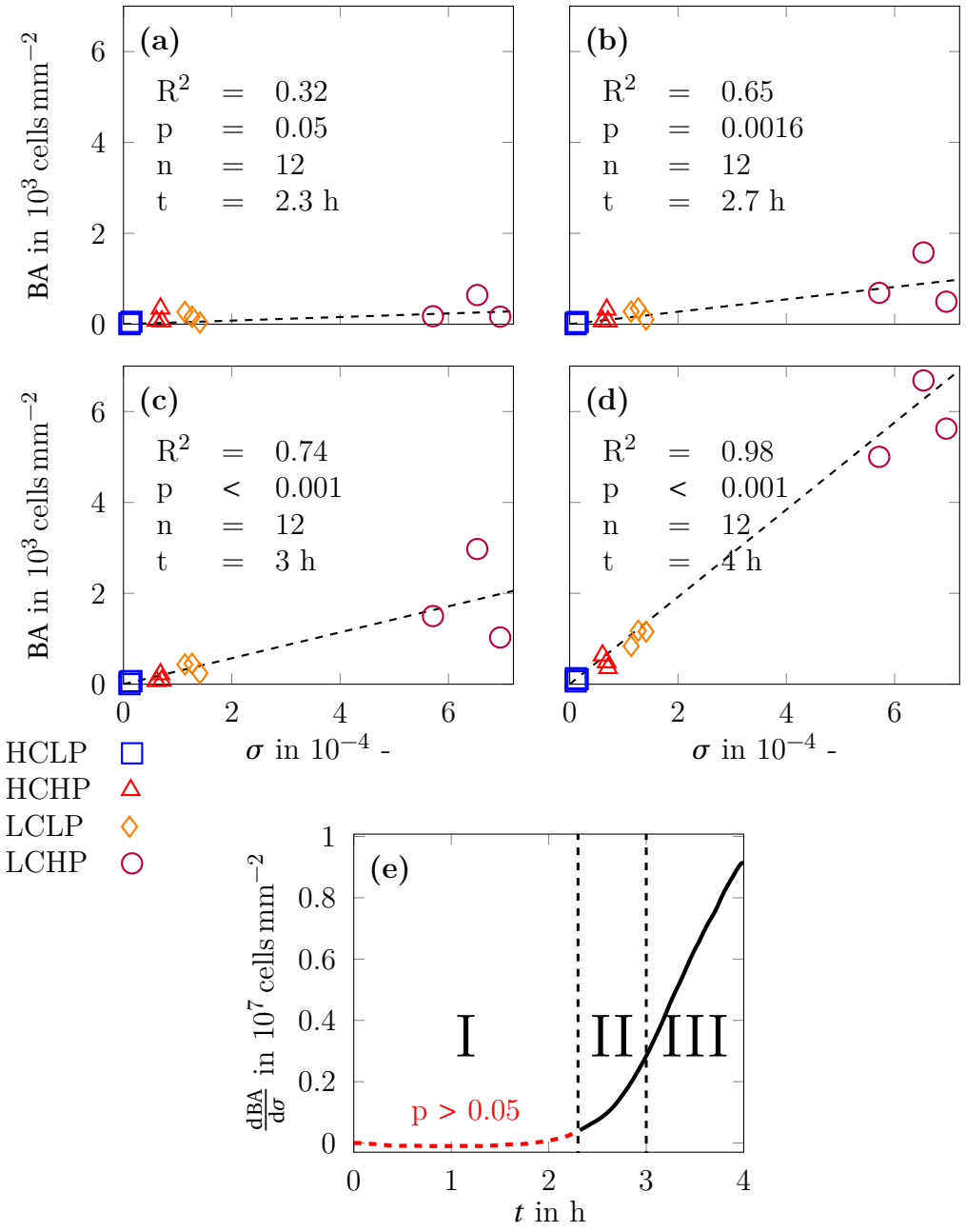

Figure 3.9: Analysis of average bacterial abundance BA over ratio σ of permeate water flux j_W to crossflow velocity u_F and time t.

nutrients induce direct movement of bacteria to the membrane surface due to chemotaxis and enhance the probability of irreversible cell attachment [92, 96]. Secondly, bacterial proliferation is expedited on the mem-

brane surface due to the increased availability of nutrients. Additionally, the concentration polarization of ions close to the membrane surface also impacts deposition (cf. Sec. 2.3.4). A higher ionic strength leads to less repulsion and increases attachment probability [34,65]. The ionic strength on the feed side of the membrane is related to reverse salt flux from the draw, permeate water flux, and mixing due to hydrodynamic conditions. Accordingly, LCHP had the highest ionic strength close to the membrane surface as mixing was limited at a low crossflow and the concentration of NaCl in the draw solution was the highest. On the other hand, HCLP had the lowest ionic strength due to high crossflow and the lowest concentration of NaCl in the draw solution. Consequently, this would further increase the difference in BA between the studied hydrodynamic conditions. Therefore, changes in concentration polarization as a result of different ratios in crossflow velocity to permeate water flux may indirectly affect bacterial deposition patterns. However, concentration polarization is less severe when treating wastewater as compared to treating solutions of high ion concentration. Hence, it was elucidated that the difference in electrostatic repulsion will have a minor relevance in the initial stages of biofilm formation using wastewater as feed solution.

3.2.4 Spatial Deposition Patterns

Analyzing the influence of the ratio of permeate water flux to crossflow velocity on spatial deposition patterns of bacteria can provide additional insights. Figure 3.10 shows the spatial deposition patterns of *B. subtilis* after 4 h of constant flow under different hydrodynamic conditions. Signs (*, +, o) indicate significantly different groups ($p < 0.05$, n = 3 independent experiments). The color of a patch signifies BA on the membrane, while the number shows the percentage of total BA from the average of three experiments for each configuration. Spatial distribution was quantified by dividing the area within the spacer element into nine sections (approx. $0.25\,\mathrm{mm}^2$) and calculating the percentage of total bacteria in each section.

The crossflow velocity impacted not only the total deposition but also

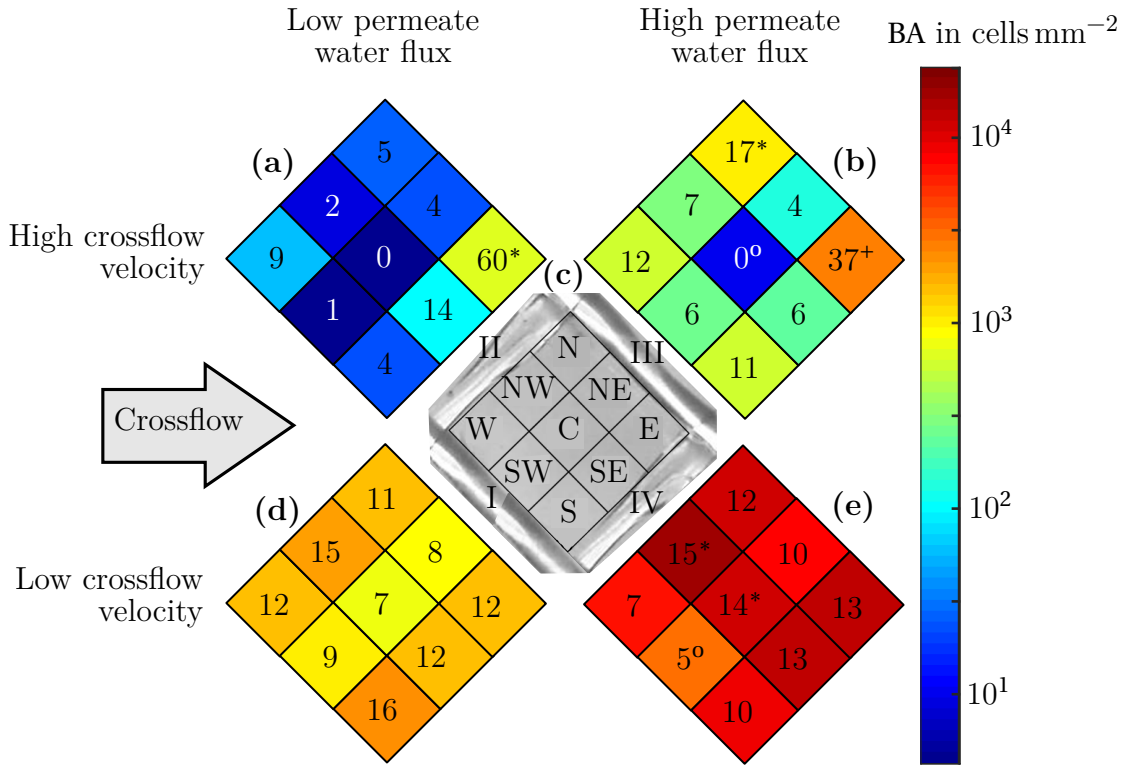

Figure 3.10: Spatial deposition patterns of *Bacillus subtilis* after 4 h.

the bacterial spatial distribution. Under low permeate water flux and high crossflow velocity most bacteria (60 %) deposited in the eastern (E) section (cf. Fig. 3.10a), while the deposition was evenly distributed at the low crossflow velocity (cf. Fig. 3.10d). Similarly, under high permeate water flux and high crossflow velocity, most of the bacterial deposition (37 %) was captured in section E (cf. Fig. 3.10b). However, under high permeate water flux and low crossflow velocity deposition was evenly distributed (cf. Fig. 3.10e). Additionally, at high crossflow velocity almost no bacteria (0.5 %) deposited in the central (C) section, which was different from the low crossflow velocity condition (14 %). For both high and low permeate water flux, an increase in crossflow velocity led to less deposition in the center as well as the sections that were between the filament crossings (SW, NW, NE, and SE). Here, the majority of deposition shifted to patches closer to the filament crossings (E, W, N, and S). A change from low (cf. Fig.

3.10a) to high permeate water flux (cf. Fig. 3.10b) at high crossflow velocity led to a more evenly distributed deposition with a significant change in the eastern (E) and northern (N) sections. Considering low crossflow velocity, an increase in permeate water flux from low (cf. Fig. 3.10d) to high (cf. Fig. 3.10e) increased the deposition by 2-fold in section C, while the percentage decreased by 60 % in the southern (S) section.

Summarizing the above, increasing the crossflow velocity led to a heterogeneous deposition close to the spacer filaments and crossings, while increasing the permeate water flux led to a more even distribution. Biofilms have previously been captured to develop at the contact points between the membrane and the spacer filaments at a permeate water flux of $105\,\mathrm{L\,m^{-2}\,h^{-1}}$ and crossflow velocity of $16\,\mathrm{cm\,s^{-1}}$ [83]. The spatial distribution of newly deposited bacteria (up to 4 h) reported here followed a comparable trend at the similarly high crossflow ($14\,\mathrm{cm\,s^{-1}}$), although the permeate water flux was lower (6 and $30\,\mathrm{L\,m^{-2}\,h^{-1}}$). On the other hand, qualitative deposition patterns of inert beads (3 µm) at varying permeate water fluxes (0 and $35\,\mathrm{L\,m^{-2}\,h^{-1}}$) and crossflow velocities ($7\,\mathrm{cm\,s^{-1}}$, $14\,\mathrm{cm\,s^{-1}}$, and $28\,\mathrm{cm\,s^{-1}}$) did not show such strong accumulation at spacer filaments during the initial stages of deposition (< 8 h) [32]. However, the differences in foulant, process conditions, and observation method hinder in-depth comparison to the quantitative deposition patterns obtained in the study at hand. Nonetheless, the results indicate that a high permeate water flux prompts irreversible attachment of cells and has a critical impact on the deposition patterns of bacteria during the initial stages of biofilm formation.

3.2.5 Bacterial Accumulation Beneath the Spacer Filaments

At the end of each experiment, the bacterial abundance BA was measured by flow cytometry (FCM) on the membrane surface and compared to BA obtained by fluorescence microscopy. Figure 3.11a shows a schematic presentation of the difference in the membrane area that is analyzed for bacterial accumulation by FCM and microscopic images. Figure 3.11b depicts

BA measured by epifluorescence microscopy and FCM after 4 hours of deposition. Asterisks indicate significantly different groups ($p < 0.05$, n = 3 independent experiments) within one configuration. The Figure 3.11c shows a representative image of *B. subtilis* biofilm in an FO channel with spacer captured by optical coherence tomography (OCT).

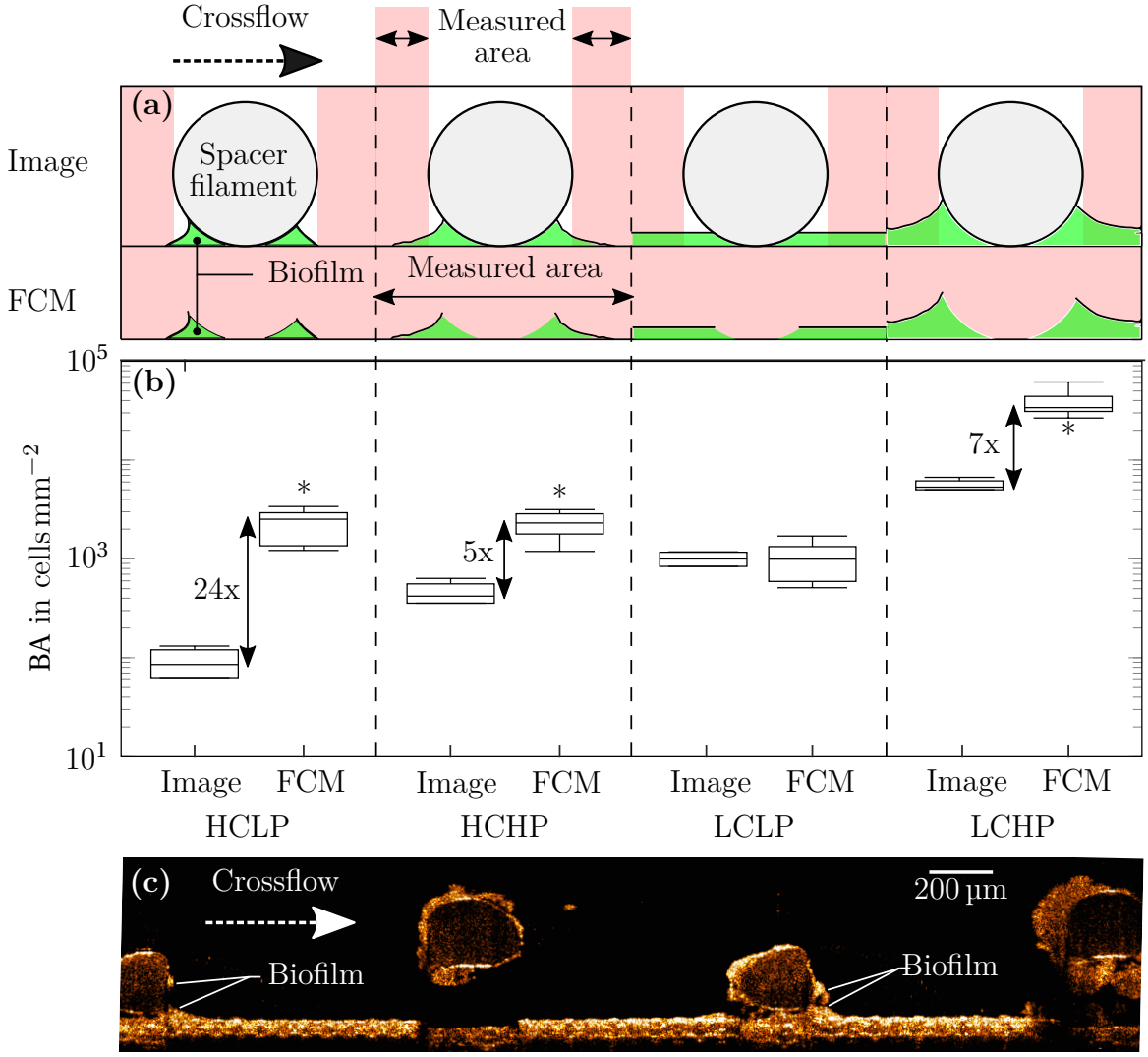

Figure 3.11: (a) Illustration of bacterial accumulation beneath spacer filaments. (b) BA measured by fluorescence microscopy and FCM. (c) Representative image of *Bacillus subtilis* biofilm in an FO channel with spacer captured by OCT.

The analysis of microscopic images resulted in three significantly differ-

ent groups (cf. Fig. 3.8a). However, only LCHP was significantly higher from the other hydrodynamic conditions in FCM measurements (cf. Fig. 3.12). Contrary to FCM measurements, microscopic images only capture the membrane area that was not concealed by the spacer filaments. Quantification of BA with flow cytometry cannot resolve the spatial distribution of BA thus included cells that also deposited underneath spacer filaments (cf. Fig. 3.11a). The area underneath spacer filaments has been observed to be highly stagnant thus will accumulate bacteria (cf. Fig. 3.11c) and other foulants [43, 83, 97].

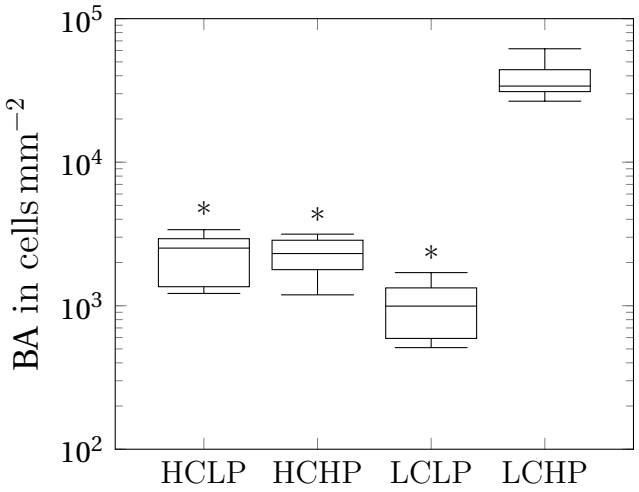

Figure 3.12: BA on the membrane surface measured by flow cytometry after 4 hours of deposition. Signs (o, *) indicate significantly different groups ($p < 0.05$, n = 9).

Accumulation of bacteria beneath the spacer filaments was only quantified by FCM measurements. It can be surmised that this accumulation caused the significant differences in BA between both methods (cf. Fig. 3.11b). Enhanced bacterial accumulation, which is deposition and growth beneath the spacer filaments, might eventually lead to an inhomogeneous mature biofilm. The spatial deposition was very homogeneous in the case of LCLP (cf. Fig. 3.10d). Only at LCLP, the number of deposited cells reached a similar value in both methods (cf. Fig. 3.11b). It can be deduced that under LCLP the cells have distributed uniformly on the membrane with minimal accumulation beneath the spacer filament.

The results showed that an increase in permeate water flux and a decrease in crossflow velocity led to homogeneous deposition, which explains the gradual change of ratio between FCM and fluorescence microscopy for HCLP, HCHP, and LCLP. However, it does not explain the difference between FCM and image analysis at LCHP. Comparing the flow paths of LCLP and LCHP led to the conclusion that small gaps between spacer filaments and membrane are blocked within minutes at LCHP. This blockage is proposed to be the main reason for enhanced deposition underneath spacer filaments at LCHP.

3.3 Implications and Applications

Bacterial flow paths and deposition patterns during the early stages of biofilm formation often affect the maturation dynamics and the consequent development of biofouling in membrane systems. In any membrane system with spacers, the bacterial flow paths and early deposition patterns will be affected by the applied crossflow velocities and permeate water fluxes. Chapter 3 investigated the deposition patterns and flow paths of *B. subtilis* during the first stages of biofilm formation in an FO system with spacers under varying hydrodynamic conditions.

It may be concluded that different hydrodynamic conditions led to a definite impact on the first stages of biofilm formation by *Bacillus subtilis* (Table 3.2):

- Bacterial velocity in the feed channel was affected by the drag force subjected by permeate water flux. Hence, bacterial velocities close to the membrane were the lowest under high permeate flux and low crossflow velocities. It was not possible to acquire the flow paths of bacteria under high crossflow velocities. However, it was suggested that bacterial motility close to the membrane surface will be higher at HCLP than HCHP.
- According to the bacterial flow paths, small gaps between the spacer

filaments and the membrane were blocked after a few minutes at LCHP but not LCLP. It was proposed that the increased permeate flux enhanced irreversible attachment and induced bacterial proliferation at LCHP, thus hindering flow in the feed channel.

- A higher ratio of permeate water flux to crossflow velocity led to a higher accumulation of cells on the membrane surface.
- A higher ratio of permeate water flux to crossflow velocity led to a more homogeneous deposition. Therefore, the difference between deposited cells beneath the spacer filaments and on the open membrane area were less at a high ratio of permeate water flux to crossflow velocity.

It is surmised that these effects would be more critical during the first stages of biofilm formation as few bacteria have yet attached, hence every slight change has a significant impact. These deposition patterns and irreversible attachments will likely dictate where biofilm grows and when biofouling develops, leading to differences in system performance.

The results obtained apply mainly to new and freshly cleaned FO systems using feedwater with high fouling propensity. Both permeation drag and lift forces act similarly in all membrane channels with spacers. Hence, Chapter 3 also has implications for other membrane systems, especially those that operate under low pressure. Studies have shown that biofilm formation differs between FO and RO due to the compression of the biofilm layer at a high hydraulic pressure [9, 10]. The results are likely also relevant for the initial deposition of bacteria in pressure-driven systems. However, they should be extrapolated with caution as the cake layer extends beyond a monolayer and compression becomes relevant.

The above insights will aid to quantify the combined effects of permeate water flux and crossflow velocity on membrane modules that commonly use spacers in feed channels. It is suggested that biofilm formation can be hindered with an appropriate choice of hydrodynamic parameters in membrane systems.

Chapter 3 has examined the initial cake layer formation of *Bacillus subtilis* in detail. Nonetheless, limits in the experimental design hinder a further examination of deposition mechanisms. Analysing the mass transfer in FO can contribute further insights into the deposition process.

Table 3.2: Summary of the different aspects affecting the initial stage of biofilm formation under hydrodynamic conditions. 1 = low, 5 = high. [a] Proposed, not measured.

	HCLP	**HCHP**	**LCLP**	**LCHP**
Ratio of crossflow velocity to permeate water flux σ	1	2	3	5
Bacterial velocity next to the membrane surface	5[a]	4[a]	2	1
Impaired flow paths through the spacer element	1[a]	1[a]	1	5
Accumulation of cells on the membrane surface	1	2	3	5
Homogeneous distribution on the membrane within the spacer element	1	2	5	4
Enhanced accumulation of bacteria beneath the spacer filaments	5	3	0	4

4 Microscopic Analysis of Mass Transfer in Forward Osmosis

Experiments with *Bacillus subtilis* have shown that the ratio of permeate water flux to crossflow velocity indicates the fouling propensity of a hydrodynamic configuration. However, limitations in the experimental design and setup hindered a detailed investigation of the deposition mechanisms. For example, increasing the crossflow velocity also leads to a higher load of nutrients and particles [98]. Hence, numerical methods can help to break down and analyze the complexity of the system [45]. Particle deposition has been studied before with numerical methods in membrane processes [45,99]. However, geometry and boundary conditions are very different to the deposition experiments presented in Chapter 3. This chapter provides more detailed insights into the interplay between crossflow velocity, permeate water flux, concentration polarization and particle deposition in similar conditions to Chapter 3.

Chapter 4 investigates the impact of crossflow velocity and permeate water flux on local flow patterns and concentration polarization in the feed channel in a representative two-dimensional geometry with computational fluid dynamics. Conditions in the draw channel affect the simulation of the feed channel by inducing a permeate water flux and a reverse salt flux (cf. Sec. 2.2.1). Lagrangian particle tracking is then used to model the deposition of polystyrene beads. Results of the deposition model are compared to experimental results. Lastly, the impact of particle size on the spatial distribution of deposition is investigated.

Chapter 2.3 introduced the most important particle forces in steady-state FO. The insights gained in this chapter indicate that these forces are a sufficient approximation to model the deposition process. The impact of

Table 4.1: Investigated hydrodynamic conditions. The permeate water flux j_W and crossflow velocity u_F was varied.

Short name	j_W	u_F
HCLP	$5\,L\,m^{-2}\,h^{-1}$	$13.7\,cm\,s^{-1}$
HCHP	$33\,L\,m^{-2}\,h^{-1}$	$13.7\,cm\,s^{-1}$
LCLP	$5\,L\,m^{-2}\,h^{-1}$	$1.1\,cm\,s^{-1}$
LCHP	$33\,L\,m^{-2}\,h^{-1}$	$1.1\,cm\,s^{-1}$

permeate water flux and crossflow velocity on deposition observed in Chapter 3 was replicated.

4.1 Methods

Here, the impact of hydrodynamic parameters on particle deposition is investigated with CFD. The methods section introduces the studied hydrodynamic cases, governing equations, the geometry of the model, the boundary conditions, and the solution procedure.

4.1.1 Investigated Hydrodynamic Cases

Four sets of simulations were conducted with different combinations of permeate water flux j_W and crossflow velocity u_F (Table 4.1).

4.1.2 Governing Equations and Solution

The mass transport was calculated by solving the Navier-Stokes equations and an incompressible transport equation for the scalar salt mass fraction w [100]

$$\nabla\left(\rho\ u\ w\right) - \nabla\cdot\left(D\ \nabla(\rho\ w)\right) = 0. \tag{4.1}$$

A Lagrangian approach was chosen to follow the particles through the computational domain. The investigated particle concentration was dilute [61][1]. Hence, particle-particle interactions and the influence of particles on the fluid flow were neglected. The particle trajectories were calculated with a previously determined flow field. Particle forces were modeled according to Section 2.3. These include the gravitational, buoyancy, lift, van der Waals, electric double layer forces, steady-state drag, pressure gradient, and Brownian motion. Particles were considered as deposited once they touched the membrane surface.

The fluid flow within the membrane channel, scalar transport, and particle deposition was calculated with the open-source tool OpenFOAM[2]. The solver was based on simpleFOAM, which decouples momentum and continuity equations, and was extended to include scalar transport.

4.1.3 Geometry Model

An FO channel contains spacers with a three-dimensional structure (cf. Fig. 4.1). In reality, the spacer structure is imperfect and varies from spacer element to spacer element. A high-resolution three-dimensional image has previously been captured and has been used for flow analysis [101, 102]. However, the computational effort is high, and the results are only valid for the investigated spacer part. Many studies [32, 103] use a representative structure of straight spacer filaments for their three-dimensional geometry. A representative two-dimensional case further simplifies the three-dimensional structure and reduces the computational effort [5, 45, 100, 104, 105]. Two-dimensional models can not fully capture the flow complexity and may overestimate concentration polarization [103], but are a good compromise between calculation time and model realism [45]. For this reason, a two-dimensional geometry model was chosen in the study at hand.

[1] Crowe et al. [61] used the particle volume fraction α_d to judge whether a flow can be considered as dilute ($\alpha_\mathrm{d} < 0.001$). In Chapter 3, α_d was below 1×10^{-7}.
[2] OpenFOAM version 6, `https://openfoam.org/version/6/`.

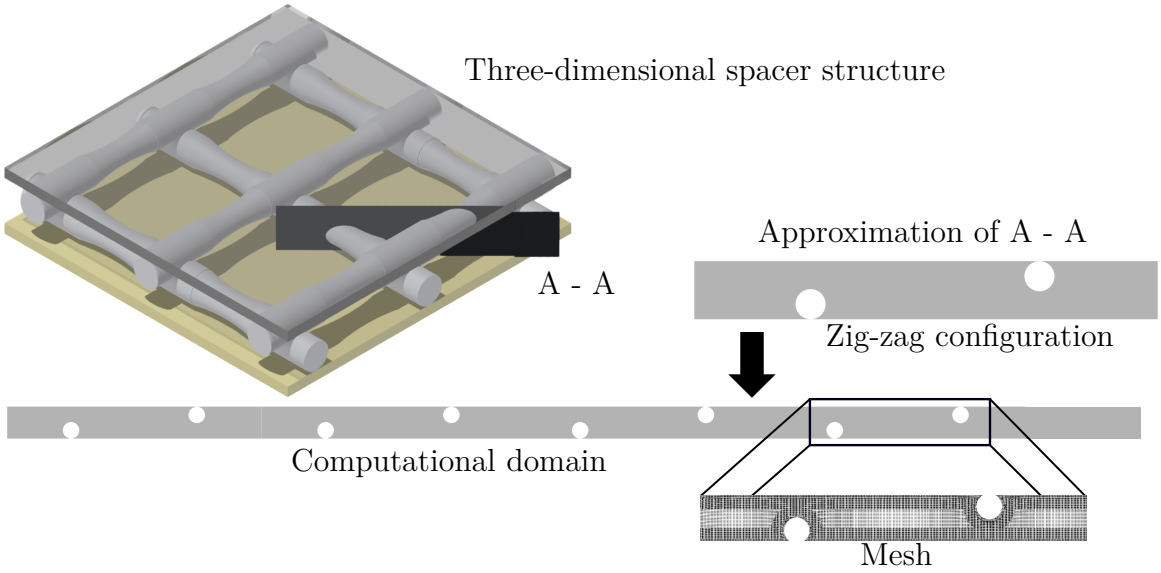

Figure 4.1: Simplification of three dimensional spacer structure by zig-zag configuration, computational domain, and mesh.

The zig-zag configuration has previously been used to examine particle deposition in membrane systems [45, 99] and was also used in the present work. Several studies have suggested that the curvature of an SWM does not significantly influence the fluid flow [45, 51]. Hence, the chosen channel geometry is representative of FO in an SWM. The computational mesh was adapted from Kiefer [104] and generated using the OpenFOAM tools blockMesh and snappyHexMesh. The mesh was then scaled by the tool transformPoints. A grid convergence study was conducted [4] to ensure the independence of the results for fluid velocity and scalar transport of the mesh (cf. Appendix Fig. A.1).

4.1.4 Boundary Conditions

Figure 4.2 visualizes the computational domain and defines the position of the patches Inlet, Wall, Membrane, and Outlet. The channel height h was 0.43 mm and the channel length L was 18.92 mm. The diameter of the spacer filament was half of h, and the distance between spacer filaments was four times h.

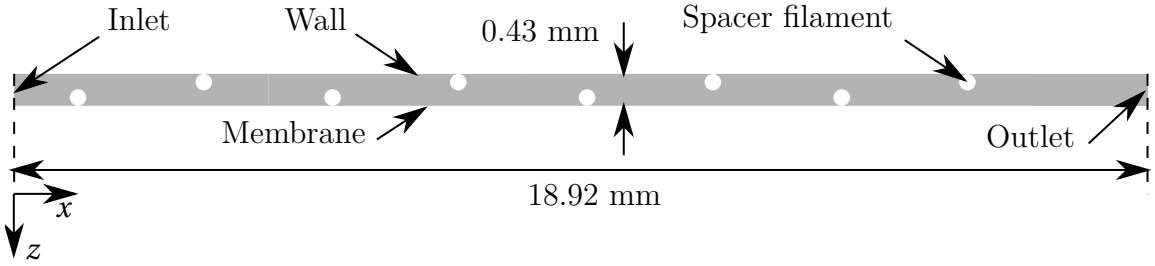

Figure 4.2: Computational domain.

Fluid Velocity

The velocity gradient was zero at the outlet of the geometry and the inlet velocity had a parabolic profile. Then, a no-slip boundary condition was applied to the wall, the membrane, and the spacer filaments.

The permeate water flux was calculated each time step and for all faces of the membrane boundary condition. In line with the study of Tiraferri et al. [2], the osmotic pressure was assumed as a linear function of the salt mass fraction. The permeate water flux j_W was calculated by combining equations 2.14 and 2.19 to [4]

$$j_W = K\left(\exp\left(-\frac{j_W S}{D}\right)\Pi_{D,b} - \Pi_{F,m}\right) + B\left(\exp\left(-\frac{j_W S}{D}\right) - 1\right). \tag{4.2}$$

The membrane parameters K, B, and S were obtained from the same membrane[3] as used in Chapter 3. Porifera [106] published results (cf. Tab. 4.2) of FO experiments. The membrane permeability K and salt permeability B were calculated by solving equations 2.24 and 2.25.

Salt Mass Fraction

The gradient of the salt mass fraction was set to zero at the outlet, the wall, and the spacers. The inlet and initial sodium chloride concentration of the feed channel was set to $8\,\mathrm{mol\,m^{-3}}$, which is the same sodium chloride

[3]FO membrane: FOMEM-0415, Porifera

Table 4.2: Membrane properties.

Parameter	Value	Source
j_W	$33 \pm 2\ \mathrm{L\,m^{-2}\,h^{-1}}$	Porifera [106]
j_S	$0.5 \pm 0.2\ \mathrm{g\,L^{-1}}$	Porifera [106]
S	$215 \pm 30\ \mu\mathrm{m}$	Porifera [106]
K	$2.56 \pm 0.39\ \mathrm{L\,m^{-2}\,h^{-1}\,bar^{-1}}$	calculated
B	$0.0626 \pm 0.038\ \mathrm{L\,m^{-2}\,h^{-1}}$	calculated

concentration as the artificial wastewater used in Chapter 3 and in the study of Bogler et al. [46]. The draw salt mass fraction was chosen to achieve the permeate water flux in the respective hydrodynamic case. In the case of high permeate water flux, a salt mass fraction of $57.3\,\mathrm{g\,kg^{-1}}$ and in the case of low permeate water flux $3\,\mathrm{g\,kg^{-1}}$ was chosen.

In FO, salt diffuses across the membrane from draw to feed. This diffusion process is called reverse salt flux. The reverse salt flux is a function of the concentration difference between both solutions (cf. Eq. 2.15). The salt flux was a mixed Dirichlet and von Neumann boundary condition, as both the gradient and the absolute value of the salt mass fraction were necessary to calculate it [100]. Coefficients C_1, C_2, C_3, and C_4 needed to be specified to calculate the salt mass fraction w_m at the membrane [100]

$$w_m = C_1\ w_P + C_2 \tag{4.3}$$

and the gradient at the membrane

$$\left.\frac{\partial w}{\partial z}\right|_m = C_3\ w_P + C_4. \tag{4.4}$$

Here, the index $_P$ denotes the node value of the adjacent cell to the membrane. The gradient of the salt mass fraction was approximated by

$$\frac{\partial w}{\partial z} \approx \frac{w_m - w_P}{\Delta z}. \tag{4.5}$$

C_1, C_2, C_3, and C_4 were determined with equation 2.20 as

$$w_{\mathrm{m}} = \underbrace{\frac{D}{D + j_{\mathrm{W}}\Delta z}}_{C_1} w_{\mathrm{P}} + \underbrace{\frac{j_{\mathrm{S}}\Delta z}{\rho D + \rho\, j_{\mathrm{W}}\Delta z}}_{C_2}, \tag{4.6}$$

and

$$\left.\frac{\partial w}{\partial z}\right|_{\mathrm{m}} = \underbrace{-\frac{D}{j_{\mathrm{W}} + D\Delta z}}_{C_3} w_{\mathrm{P}} + \underbrace{\frac{j_{\mathrm{S}}}{\rho D + \rho\, j_{\mathrm{W}}\Delta z}}_{C_4}. \tag{4.7}$$

The resulting boundary condition considers both internal concentration polarization (ICP) and external concentration polarization (ECP).

Pressure

The pressure gradient at the inlet, wall, spacer filaments, and the membrane was set to zero [100]. It was assumed that the pressure does not influence the fluid density [100]. The pressure at the outlet was the reference pressure. The initial internal pressure field was set to the reference pressure.

Simulation Parameters

Carboxylate modified polystyrene beads have a similar density ρ_{p} and surface potential as bacteria (cf. Tab. 4.3). The surface potential can be approximated by the zeta potential [73]. McGill and Smyth [108] determined the zeta potential of carboxylate modified polystyrene beads ψ_{p} as -58.74 ± 1.66 mV at a pH value of 7.4. Hurwitz et al. [107] measured the zeta potential of a polyamide membrane ψ_{m} as -30 mV at a pH value of 7. Crowe et al. [61] published the Hamaker constant of polystyrene beads H_{p} as 6.15 to 6.6×10^{-20} J, and of water H_{f} as 4.38×10^{-20} J. Shankaram and Wiesner used a membrane Hamaker constant H_{m} of 5×10^{-20} J for their deposition studies [62]. These parameters were used in the simulation.

Table 4.3: Simulation parameters.

Parameter	Value	Source
ψ_m	$-30\,\mathrm{mV}$	Hurwitz et al. [107]
ψ_p	$-58.74\,\mathrm{mV}$	McGill and Smyth [108]
H_m	$5 \times 10^{-20}\,\mathrm{J}$	Shankaram and Wiesner [62]
H_p	$6.375 \times 10^{-20}\,\mathrm{J}$	Crowe et al. [61]
H_f	$4.38 \times 10^{-20}\,\mathrm{J}$	Crowe et al. [61]
ρ_p	$1055\,\mathrm{kg\,m^{-3}}$	Johnson and Spence [109]
h	$0.43\,\mathrm{mm}$	Bogler et al. [46]
N_{inj}	1.072×10^6 beads	-
t_{inj}	$4\,\mathrm{s}$	-
t_{tot}	$30\,\mathrm{s}$	-

A total number N_{inj} of 1.072×10^6 beads was injected over a duration t_{inj} of 4 s. The particles enter through the inlet patch and leave the channel through the outlet or get stuck on the membrane surface. The simulation time t_{tot} was set to 30 s so that all the active particles in the domain can settle or leave the domain.

4.2 Impact of Hydrodynamics on Fluid Flow, Concentration Polarization, and Particle Deposition

In the present section, the fluid flow and concentration profile in the feed channel are discussed. Afterward, the deposition results are analyzed and compared to fluorescence microscopy experiments. The deposition model is then used to investigate the impact of particle size on particle deposition.

4.2.1 Fluid Flow in a Spacer-Filled Channel

The impact of the crossflow velocity u_F on the local fluid velocity u has been studied before in spacer-filled channels [45, 99]. However, each study has differing geometries and boundary conditions. This subsection investigates the impact of the crossflow velocity u_F on the local fluid velocity u with the same setup that will later be used to analyze local salt concen-

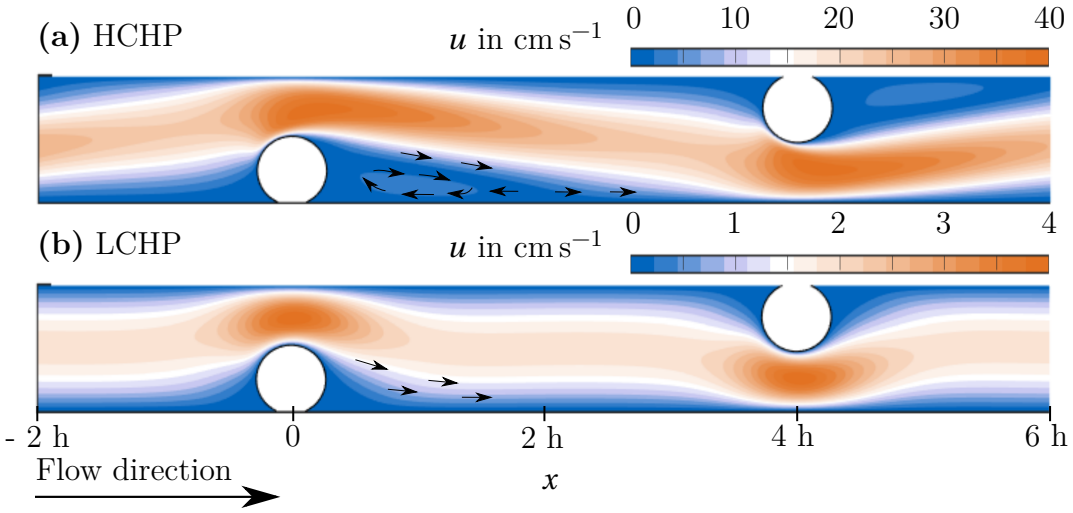

Figure 4.3: Fluid velocity u in the feed channel of FO.

tration and particle deposition in forward osmosis. Figure 4.5 depicts the velocity profile u in the computational domain between $x = 10.32\,\text{mm}$ and $x = 13.76\,\text{mm}$. The color scale indicates the absolute value of u, while the arrows indicate velocity directions. Both cases of high (HC) and low (LC) crossflow velocities u_F were calculated with high permeate water flux j_W (HP). The permeate water flux j_W did not significantly alter the velocity profile. Hence, the velocity profile of HP cases are also representative for LP conditions.

At LCHP, the flow profile was parabolic and changed only in close vicinity of the spacer filaments. In the case of HCHP, the flow did not attach to the membrane surface immediately downstream of the upstream spacer filament. Instead, a recirculation zone [87] formed (cf. black arrows Fig. 4.5a). Between $x = 0$ and $x = 2\ h$, the fluid shear τ_m on the membrane surface was directed opposite to the general flow direction. The spacer filaments obstructed the channel and forced the fluid to accelerate. The highest fluid shear on the membrane surface $\tau_\text{m,max}$ was reached opposite to the downstream spacer filament ($x = 4\ h$).

The flow velocity u has a considerable influence on concentration polarization [87] and particle deposition [99]. A high flow velocity u of $40\,\text{cm}\,\text{s}^{-1}$ close to the membrane surface increases convection which expedites sodium

chloride transport away from the membrane and thus reduces external concentration polarization (ECP) [100]. Concerning particle deposition, an increase in velocity u leads to more drag and lift forces (cf. Sec. 2.3.2) that influence deposition [3, 32, 35].

4.2.2 Local Salt Concentration

This subsection analyzes the simulation results for FO based on the approach of Kiefer [104] to study mass transfer in membrane distillation. The hydrodynamic parameters crossflow velocity u_F and permeate water flux j_W influenced the local concentration profile of sodium chloride c (cf. Fig. 4.4). In all cases, the highest c was reached close to the spacer filament, where scalar transport was governed by diffusion. At LCHP (cf. Fig. 4.4a), the maximum c was 4.7 times higher than c of the bulk solution, 3 times at HCHP (cf. Fig. 4.4b), 1.3 times at LCLP (cf. Fig. 4.4c), and 1.2 times at HCLP (cf. Fig. 4.4d).

A probability density function of the sodium chloride concentration on the membrane surface c_m can provide further insights. Figure 4.4 shows the fraction A of membrane area A_m that reaches a certain concentration c_m. With an increase in permeate water flux or a decrease in crossflow velocity, the mean concentration increased. Additionally, a decrease in crossflow velocity and an increase in permeate water flux widened the histogram, which implies a more heterogeneous distribution of concentration.

In the following, the average concentration of sodium chloride on the membrane surface $\bar{c}_\mathrm{m}$ will be investigated in more detail. Fig. 4.5a depicts the dependency of $\bar{c}_\mathrm{m}$ on the permeate water flux j_W for high, medium, and low crossflow velocities u_F. $\bar{c}_\mathrm{m}$ is a linear function of j_W for all three u_F. Considering the dependency of $\bar{c}_\mathrm{m}$ on the crossflow velocity u_F (cf. Fig. 4.5b), $\bar{c}_\mathrm{m}$ is not a linear function of u_F. The higher u_F, the less the impact of a further change on $\bar{c}_\mathrm{m}$.

The local ion concentration at the membrane has significant effects in FO. An increased ion concentration leads to less permeate water flux. A higher

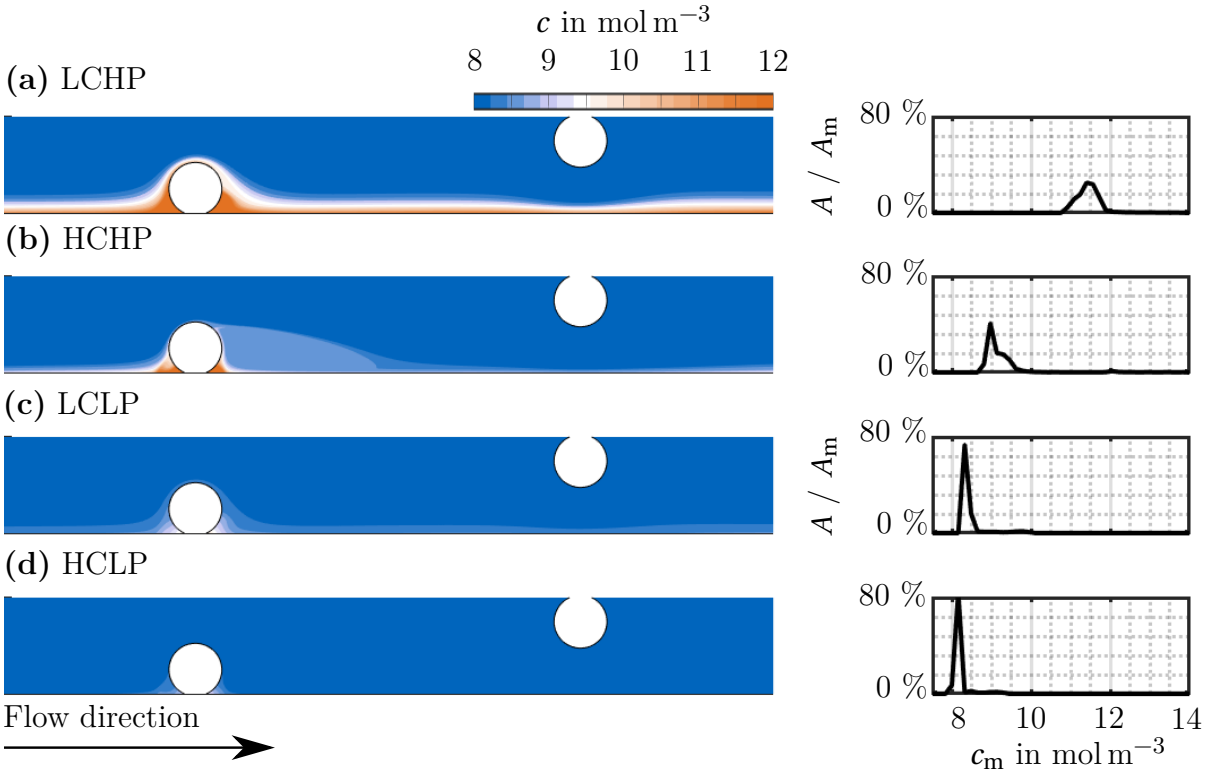

Figure 4.4: Impact of hydrodynamic conditions on molar concentration profile c and probability density function of c_m on the membrane surface. The membrane is at the bottom and an impermeable wall is at the top of each element (cf. Fig. 4.2).

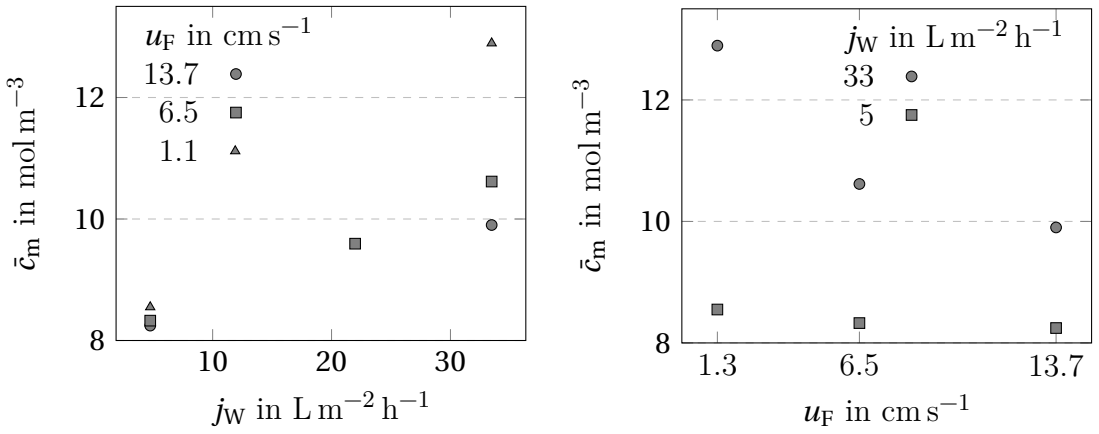

(a) Concentration $\bar{c}_m$ as a function of permeate water flux j_W for different crossflow velocities u_F.

(b) Concentration $\bar{c}_m$ as a function of crossflow velocity u_F for different permeate water fluxes j_W.

Figure 4.5: Estimation of average molar concentration on the membrane surface $\bar{c}_m$ for the calculated cases.

ion concentration also decreases the kinetic barrier for irreversible attachment (cf. Sec. 2.3.4) which leads to more deposition [3, 34, 110].

Simulations were conducted with sodium chloride in this section. However, the results for sodium chloride also have implications for other solutes. The selective permeation of the membrane will also lead to concentration polarization of nutrients and carbon close to the membrane, which increases the deposition of bacteria [92, 93]. Thus, an increase in permeate water flux and a decrease in crossflow velocity leads to an increase in ECP of nutrients and carbon and more deposition of bacteria on the membrane surface.

4.2.3 Comparison of the Deposition Model to Experiments

This section compares the simulated deposition probabilities to the deposition count obtained in experiments (cf. Ch. 3 and Bogler et al. [46]).

Contrary to the experiments, the number of injected particles was fixed in the simulations. The particle deposition probability Ψ was defined as the ratio of deposited particles N_{dep} to the total number of injected particles

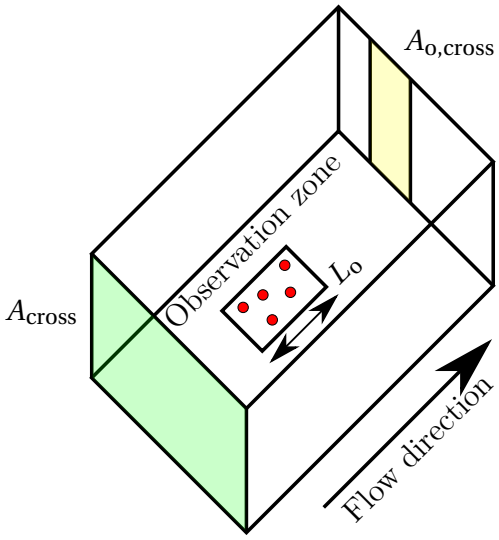

Figure 4.6: Illustration of the crossflow area A_{cross}, crossflow area of the deposition zone $A_{o,cross}$, and length of the deposition zone L_o.

N_{inj} and length of the observation zone L_o (cf. Fig. 4.6)

$$\Psi = \frac{N_{dep}}{N_{inj}\ L_o}. \tag{4.8}$$

The second spacer element between $x = 3.44\,\text{mm}$ and $x = 6.88\,\text{mm}$ was chosen for analysis. It is far enough from the channel entrance to avoid entrance effects [35], but there are still enough particles within the bulk fluid for the deposition study.

In experiments, the particle load that passes a spacer element increases with an increase in crossflow velocity. The particle number N_{inj} that passes the deposition zone can be calculated as

$$N_{inj} = c_p\ \dot{V}\ \frac{A_{o,cross}}{A_{cross}}. \tag{4.9}$$

Here, c_p is the particle concentration, $\dot{V}$ the volume flow rate, and A_{cross} the total test cell area perpendicular to the crossflow direction. $A_{o,cross}$ is then the area perpendicular to the flow direction of the deposition zone.

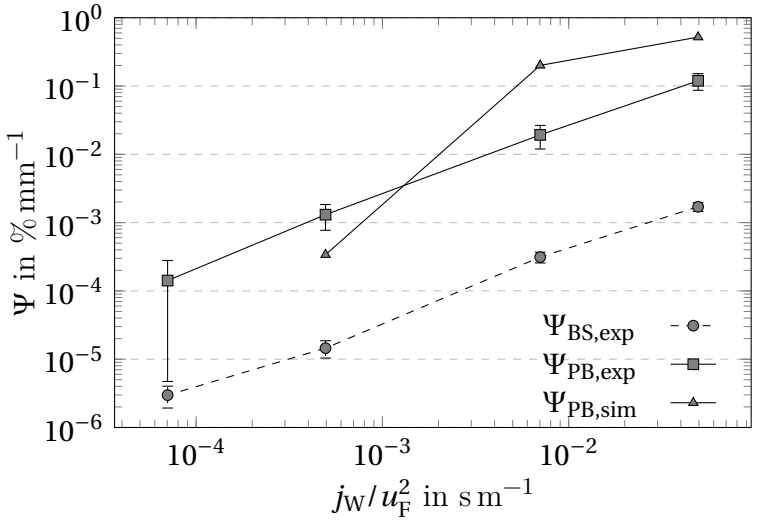

Figure 4.7: Deposition probability Ψ over ratio of permeate water flux j_W to crossflow velocity square u_F^2.

The deposition probability for *Bacillus subtilis* $\Psi_{BS,exp}$ (cf. Fig. 3.9) and polystyrene beads $\Psi_{PB,exp}$ was calculated by equation 4.8. Results of deposition experiments for polystyrene beads were obtained from the study of Bogler et al. [46]. The deposition count N_{dep} was linearly proportional to the ratio σ of permeate water flux j_W to crossflow velocity u_F. However, the deposition probability Ψ was linearly proportional to the ratio of j_W to u_F^2 (cf. Fig. 4.7). In the calculation of Ψ, N_{dep} was divided by the number of injected particles N_{inj}. N_{inj} was proportional to u_F. Hence, Ψ was proportional to $1/u_F^2$. The deposition probability of Bacillus subtilis $\Psi_{BS,exp}$ was

$$\Psi_{BS,exp} = 3 \times 10^{-1} \ \frac{j_W}{u_F^2} s^{-1}. \tag{4.10}$$

The $\Psi_{PB,exp}$ of polystyrene beads was

$$\Psi_{PB,exp} = 2.41 \times 10^{1} \ \frac{j_W}{u_F^2} s^{-1}. \tag{4.11}$$

Across the range of investigated hydrodynamics, the deposition probability of polystyrene beads $\Psi_{PB,exp}$ was two magnitudes higher than the deposition probability of *Bacillus subtilis* $\Psi_{BS,exp}$. Close to the membrane surface, the flow velocity decreases significantly. It was suggested [47] that

the attachment probability is influenced by the ability of bacteria to swim independently and actively detach from the surface. The motility of the bacteria explains the difference in attachment probability. Additionally, the geometry and size of *Bacillus subtilis* is different to polystyrene beads, which will be discussed in Section 4.2.4. Although there is a significant difference in deposition probability, the impact of hydrodynamics is very similar in both cases. It can thus be confirmed that polystyrene beads are a good proxy for qualitative deposition studies of *Bacillus subtilis*. However, quantitative results are not transferable.

$\Psi_{\mathrm{PB,sim}}$ was 4 times higher than $\Psi_{\mathrm{PB,exp}}$ at a ratio $j_{\mathrm{W}}/u_{\mathrm{F}}^2$ of $4.95 \times 10^{-2}\,\mathrm{s\,m^{-1}}$. The particle deposition model overestimated deposition at high ratios of permeate water flux to crossflow velocity square. The model assumed that once particles reach the membrane surface, they deposit and remain stuck to the membrane surface. More sophisticated models for particle adsorption could help increase prediction accuracy [66].

At $j_{\mathrm{W}}/u_{\mathrm{F}}^2 = 4.95 \times 10^{-4}\,\mathrm{s\,m^{-1}}$, $\Psi_{\mathrm{PB,sim}}$ was 4 times lower than $\Psi_{\mathrm{PB,exp}}$. No deposition was registered in the simulation at $j_{\mathrm{W}}/u_{\mathrm{F}}^2 = 7 \times 10^{-5}\,\mathrm{s\,m^{-1}}$. At low ratios of permeate water flux to crossflow velocity square, the simulation underestimated particle deposition. At both HCHP, and HCLP, most particles deposited close to spacer filament junctions in experiments (cf. Fig. 3.10a, and 3.10b). The two-dimensional geometry in the simulation can not represent the deposition mechanisms near filament junctions and consequentially underestimates deposition probability. Concomitantly, the membrane was assumed as smooth in simulations. The roughness of the membrane might cause more particles to attach, as roughness leads to a generally larger deposition area, locally lower shear rates, and reduced colloidal repulsion [34, 111, 112].

In all three cases, experiments and simulation, decreasing the ratio of permeate water flux to crossflow velocity square led to a decrease in deposition probability. The comparison has shown that the deposition model contained the forces that are responsible for the influence of hydrodynamics on deposition in FO with spacers. The model can be used for further qualitative investigations.

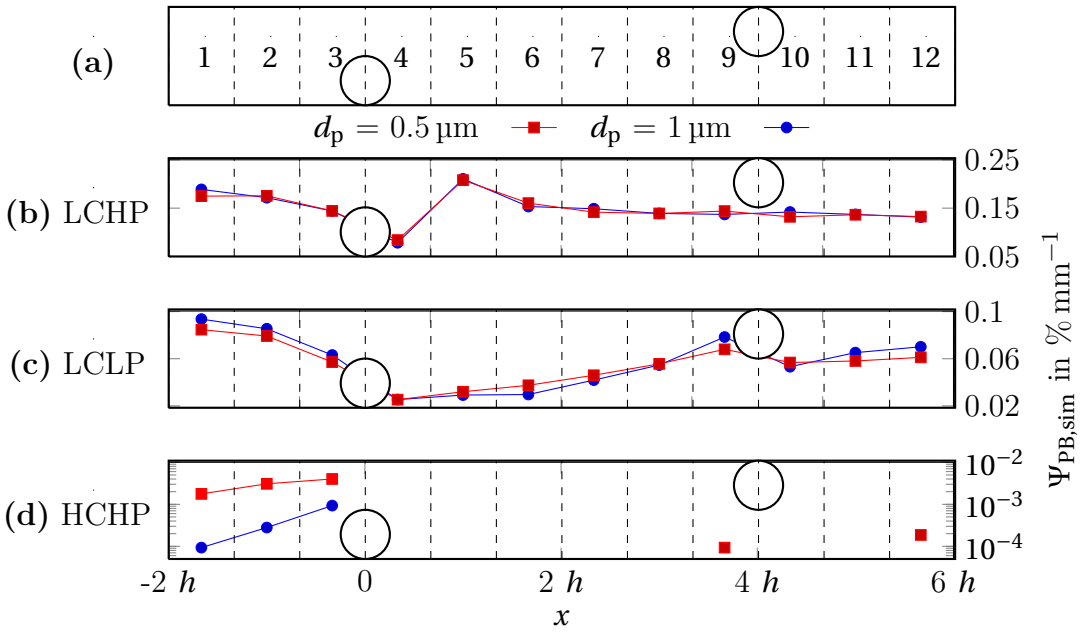

Figure 4.8: Spatial distribution of deposition probability $\Psi_{PB,sim}$ (cf. Eq. 4.8) as a function of position x and particle size d_p. $\Psi_{PB,sim}$ is shown in logarithmic scale at HCHP.

4.2.4 Influence of Particle Diameter on Spatial Deposition

So far, experiments have been conducted with polystyrene beads and *Bacillus subtilis*. The polystyrene beads had a particle size d_p of 1 µm. *Bacillus subtilis* are rod shaped and have a size of 0.8 µm x 5 µm. The particle diameter d_p has a large influence on particle forces (cf. Sec. 2.3.2). The deposition model makes it possible to investigate the impact of the particle diameter d_p on the spatial distribution of deposition in a spacer element.

For this purpose, the spacer element was divided into 12 zones (cf. Fig. 4.8a). Each zone was 0.43 mm long. The deposition probability $\Psi_{PB,sim}$ was calculated for a particle size d_p of 0.5 µm and 1 µm. Figure 4.8b-d show the spatial distribution of $\Psi_{PB,sim}$ for LCHP, LCLP, and HCHP. No deposition was observed in the case of HCLP. Hence, HCLP is not depicted.

At both d_p, most deposition occurred at LCHP, followed by LCLP, HCHP, and than HCLP. The ratio j_W / u_F^2 is a good indication for fouling propensity

for both d_p.

At LCHP, the highest deposition probability $\Psi_{PB,sim}$ was in zone 5 and zone 1 at LCLP. $\Psi_{PB,sim}$ was least in zone 4 at LCHP and LCLP. At low crossflow velocities u_F, the fluid flow re-attaches to the membrane surface in zone 5 (cf. Fig. 4.5b). Here, the fluid flow transports particles close to the membrane surface. At LCHP, j_W is higher than at LCLP, leading to a higher $\Psi_{PB,sim}$ in zone 5. The number of particles that pass close to the membrane surface is low in zone 4. Thus, zone 4 was the region with the least $\Psi_{PB,sim}$.

At LCHP, LCLP and HCHP, the spatial distribution of $\Psi_{PB,sim}$ was similar for both d_p. However, the value of $\Psi_{PB,sim}$ was significantly different at HCHP. The drag force is higher for large particles than for small particles (cf. Eq. 2.42). The difference in drag force is more pronounced when u_F is high (HCHP). Hence, the difference in $\Psi_{PB,sim}$ between particle diameters was larger at HCHP than at LCHP or LCLP.

This subsection has shown that the insights gained with one particle have implications for other particles with half or double the diameter. The spatial distribution of deposition for each hydrodynamic case was similar between the studied particle sizes. However, the number of deposited particles differed at a high crossflow velocity.

4.3 Conclusion

Chapter 4 analyzed the impact of hydrodynamics on fluid flow, concentration polarization, and particle deposition in FO with CFD. The hydrodynamics were varied to cover a wide range of operational parameters. The model was compared to previous experiments.

The driving parameters of particle deposition were permeate water flux j_W and crossflow velocity u_F (cf. Tab. 4.4). The highest maximum wall shear $\tau_{m,max}$ was observed for the high crossflow cases. The average concentration of sodium chloride on the membrane $\bar{c}_m$ was highest in the case of LCHP,

than HCHP, LCLP, and HCLP. Both permeate water flux j_W and crossflow velocity u_F significantly influenced particle deposition of polystyrene beads with a diameter of 1 µm. An increase in permeate water flux j_W led to an increase in deposition probability $\Psi_{PB,sim}$, while an increase in crossflow velocity u_F did the opposite.

Table 4.4: Quantitative comparison of calculated variables ($\tau_{W,max}$, $\bar{c}_m$, $\Psi_{PB,sim}$) and driving variables (j_W, u_F).

Variables	**LCHP**	**LCLP**	**HCHP**	**LCLP**
j_W in $L\,m^{-2}\,h^{-1}$	33	5	33	5
u_F in $cm\,s^{-1}$	1.3	1.3	13.7	13.7
$\tau_{m,max}$ in Pa	0.71	0.71	9.31	9.31
$\bar{c}_m$ in $mol\,m^{-3}$	12.89	8.55	9.90	8.25
$\Psi_{PB,sim}$ in $\%\,mm^{-1}$	1.8	0.69	1.6×10^{-3}	0

Comparing the deposition model to experiments has revealed that the model features the most relevant mechanisms that connect hydrodynamics and deposition probability. Additionally, further investigation of deposition probability in experiments led to the conclusion that polystyrene beads are a good proxy for a qualitative study of *Bacillus subtilis* deposition.

The impact of particle diameter on spatial deposition patterns was investigated next. Similar qualitative tendencies were found for the studied particle diameter. However, the number of deposited particles differed at high crossflow velocities. Hence, the difference in spatial deposition patterns is expected to be minor when varying the particle diameter whereas quantitative results are not comparable at high crossflow velocities.

Chapter 4 has examined the steady-state deposition process on a microscopic level. The outcome provides more detailed insights into relevant mechanisms in deposition studies. The first research aim of the dissertation was to contribute to the understanding of the steady-state deposition process in an SWM. Chapter 6 combines the results of Chapters 3 and 4 and models the impact of steady-state hydrodynamics and pulsating flows on deposition in an SWM. Hence, the fouling mitigation by pulsating flows has to be assessed on a laboratory scale first. Chapter 5 studies pulsating flow experiments on a laboratory scale. Although modeling was limited to

steady-state flow in Chapter 4, some concepts like concentration polarization and DVLO theory are also relevant in pulsating flow conditions.

5 Impact of Pulsating Flows on Particle Deposition

The second research aim of the dissertation is to assess whether pulsating flows are a viable technique to mitigate initial cake layer formation in a forward osmosis (FO) spiral-wound module (SWM). This chapter investigates the impact of pulsating flows on particle deposition on a laboratory scale.

Chapter 5 builds on the knowledge obtained in Chapter 3 and 4, which have confirmed that steady-state hydrodynamics significantly influence the deposition of particles. Here, the impact of pulsating feed flows on initial cake layer formation is studied. Spatial and temporal particle deposition is investigated quantitatively by fluorescence microscopy. Results show that both the frequency and amplitude of the pulsation are parameters that influence cake layer formation. Concomitantly, pulsating feed flows lead to less particle deposition and a significant change in deposition patterns.

5.1 Materials and Methods

The following materials and methods section introduces the experimental setup, the experimental procedure, the generation and measurement of pulsating flows, and the image acquisition.

5.1.1 Pulsating Forward Osmosis Setup

Similar to steady-state experiments (cf. Chap. 3), pulsating flow experiments were initiated in a bench-scale FO system with spacers (cf. Fig 5.1).

Deposited polystyrene beads were quantified with a mono-wavelength light

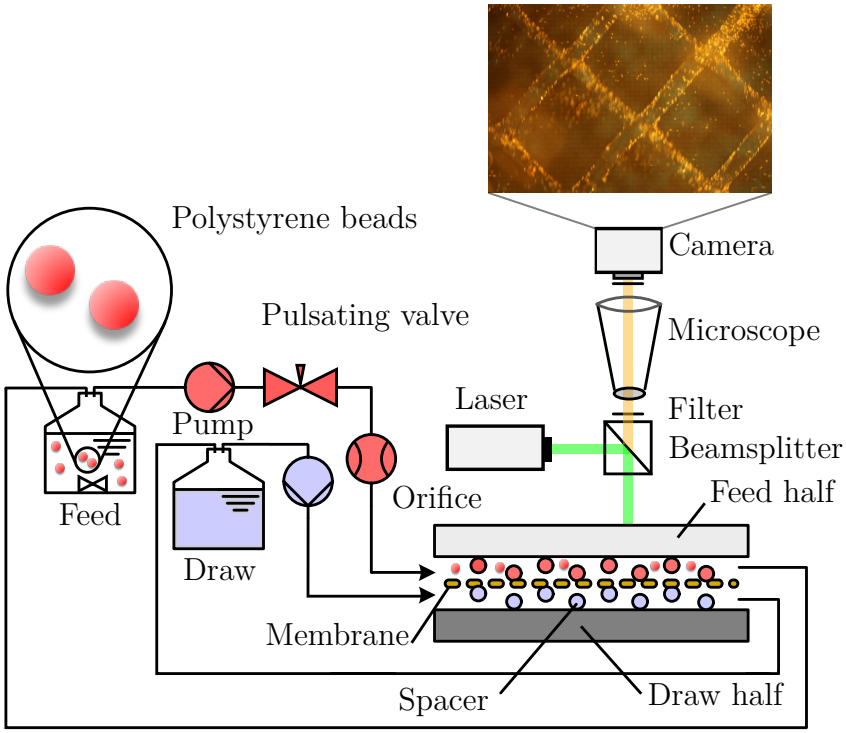

Figure 5.1: Schematic drawing of the bench-scale pulsating FO system with a cross-sectional view of the membrane crossflow cell.

source[1], a dichroic mirror[2], a long-pass filter[3], a long-distance microscope[4], and a camera[5].

Gear pumps[6] were used to set the crossflow rates, which were controlled by gravimetric measurements. The system temperature was maintained at 25 ± 0.5 °C. The permeate water flux was calculated from continuous measurements using a scale[7] beneath the draw reservoir. A valve[8] was used to initiate a pulsating crossflow with a defined frequency and duty value,

[1]Mono-wavelength light source: 514 nm, Coherent, Inc., USA
[2]Dichroic mirror: 50% transmission at 550 nm, Thorlabs GmbH, USA
[3]Long-pass filter: transmission 539 - 1,200 nm, Razor Edge LP 532 RU, AHF Analysentechnik AG, Germany
[4]Long-distance microscope: Infinity K2/Sc CF-3, Edmund Optics®, USA
[5]Camera: EOS 750D, Canon Inc., Japan
[6]Gear pumps: Diener Precision Pumps, Switzerland
[7]Scale: Kern & Sohn GmbH, Germany
[8]Pulsating valve: Landefeld Druckluft und Hydraulik GmbH, Germany

e.g., the percentage of time the valve is open. The valve was limited to frequencies of 10 Hz and below. The pulsation amplitude was measured with a 3D printed orifice. The crossflow cell, membrane, and spacers were the same as in Chapter 3.

5.1.2 Determining the Pulsation Amplitude

Pulsating flows were characterized by frequency, mean, and maximum crossflow velocity. The frequency and the mean crossflow velocity were controlled by the frequency of the valve and the speed of the pump. However, the maximum crossflow velocity was a function of the frequency and the duty value of the valve.

The amplitude of the crossflow velocity had to be measured. For this purpose, an orifice was 3D printed (cf. Fig 5.2a) with a resin 3D printer[9]. The pressure drop across the orifice was measured by a differential pressure sensor[10], which was then used to calculate the transient mass flow rate $\dot{m}$ based on Doblhoff-Dier et al. [113]. They related the pressure drop Δp across an orifice to $\dot{m}$

$$\Delta p = \frac{A_{\text{orifice}}}{\rho_{\text{F}}} \ \dot{m}^2 \ \text{sign}(\dot{m}) + B_{\text{orifice}} \frac{d\dot{m}}{dt}, \tag{5.1}$$

where A_{orifice} and B_{orifice} relate mass flow rate to the pressure drop across the orifice.

The parameter A_{orifice} depends on fluid properties and flow resistances, as well as the geometry of the aperture. A_{orifice} can be derived by measuring Δp at several steady-state mass flow rates $\dot{m}$, as equation 5.1 simplifies at steady-state (cf. Fig 5.2b). There was a linear correlation between the pressure drop Δp across the orifice and the squared mass flow rate $\dot{m}^2$ through the orifice ($\rho > 0.99$, $p < 0.01$). The corresponding value for A_{orifice} was $8 \times 10^{11}\ \text{m}^{-4}$.

B_{orifice} was determined in pulsating experiments (cf. Tab. 5.1). The devia-

[9]Resin 3D printer: Elagoo Inc., China
[10]Pressure sensor: -0.2 to 0.2 bar, Keller Ag, Switzerland

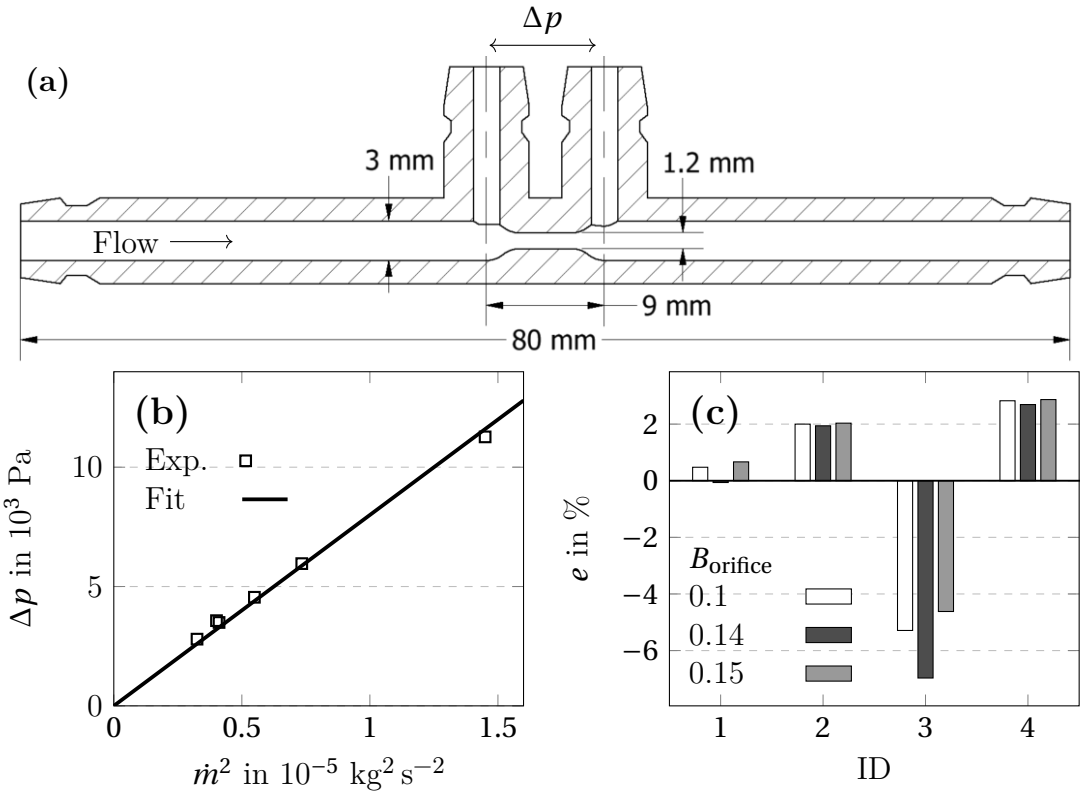

Figure 5.2: (a) 3D printed orifice. (b) Steady-state experiment to determine A_{orifice}. (c) Error e for several values of B_{orifice}. Experimental ID refers to table 5.1.

Table 5.1: Pulsating flow experiments to determine the B_{orifice} parameter for the 3D printed orifice.

ID	f in Hz	Duty value	$\dot{V}$ in L h^{-1}
1	10	0.3	6.6
2	10	0.5	7.5
3	5	0.3	6.3
4	5	0.5	7.0

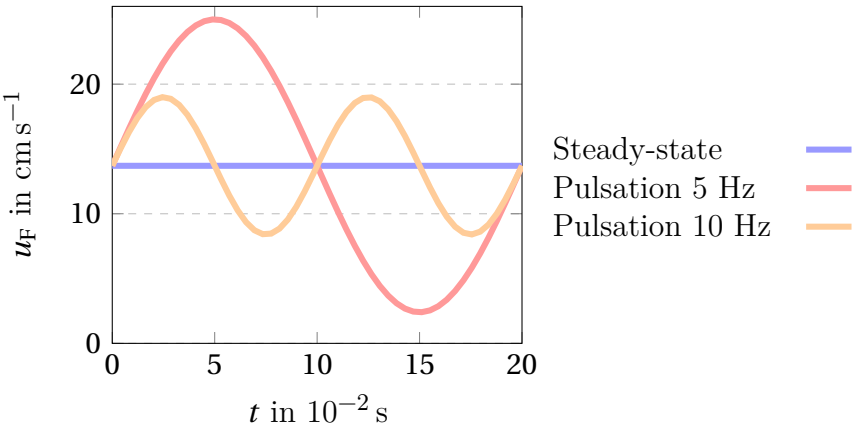

Figure 5.3: Crossflow velocity u_F over time t of the three hydrodynamic conditions.

tion e was defined as

$$e = \frac{\bar{\dot{m}}_{\text{orifice}} - \dot{m}}{\dot{m}}. \tag{5.2}$$

Here, $\bar{\dot{m}}_{\text{orifice}}$ was the mean mass flow rate determined by the orifice. $\dot{m}$ was the mass flow rate obtained by volumetric measurements. B_{orifice} was chosen as 0.136 to minimize e (cf. Fig 5.2c).

Once parameters A_{orifice} and B_{orifice} had been determined, the amplitude $\tilde{u}_F$ was measured inside the test rig (cf. Fig 5.1a). The orifice was inserted between the valve and the test cell. Measurements resulted in $\tilde{u}_F$ of 11.3 $\pm$ 3 cm s^{-1} in the case of 5 Hz and 5.3 $\pm$ 1.6 cm s^{-1} in the case of 10 Hz (cf. Fig 5.3). It is important to note that the amplitude measurements were taken separately from the deposition experiments to reduce the complexity of the experimental procedure.

5.1.3 Experimental Procedure

The FO membrane was stored at 4 °C in 1 % $NaHSO_3$ solution and was thoroughly washed by reverse osmosis permeate (ROP, $\kappa_C < 40\,\mu S\,cm^{-1}$) before use. After the membrane and spacers had been inserted in the cross-flow cell, the system was run with ROP until air bubbles were removed.

The experiment was initiated by adding artificial sterile wastewater stock solution to the feed (cf. Sec. 3.1.3). At the same time, the draw reservoir was supplemented with $5 \times 10^3\,\mathrm{mol\,m^{-3}}$ NaCl stock solution to reach a total volume of 6.9 L with the required draw concentration of $0.65 \times 10^3\,\mathrm{mol\,m^{-3}}$ to maintain a permeate water flux of $17.6 \pm 0.58\,\mathrm{L\,m^{-2}\,h^{-1}}$. Draw conductivity was measured[11].

After 15 min of stabilization, the feed solution was spiked with fluorescent carboxylate-modified polystyrene beads[12] with a particle diameter d_p of 1 µm. The particle concentration was $3.6 \times 10^7\,\mathrm{beads\,L^{-1}}$ in the feed solution. Lastly, image acquisition was started.

Three independent sets of experiments with different frequencies (0, 5, 10 Hz) were conducted over four hours. The mean crossflow velocity $\bar{u}_\mathrm{F}$ was set to $13.7\,\mathrm{cm\,s^{-1}}$ and the permeate water flux j_W to $17.6 \pm 0.6\,\mathrm{L\,m^{-2}\,h^{-1}}$. The parameters $\bar{u}_\mathrm{F}$ and j_W were chosen to mimic full-scale FO SWMs [22, 87]. The mean Reynolds number (cf. Eq. 2.28) was approximately 60.

5.1.4 Image Acquisition and Analysis

The imaging method was similar to Chapter 3. The main difference was the light source for the excitation of the particles. Here, the bright-field light source was replaced by a monochromatic light source. This replacement made it possible to visualize a larger deposition area, which was three spacer elements instead of one. A monochromatic light source eliminates the need for a filter that narrows the excitation wavelength. The result is an increased excitation power and more light emission of the particles.

Three spacer elements were chosen for image acquisition in the middle of the flow cell to eliminate possible effects on deposition from the inlet and outlet and the channel walls [32, 87]. The microscope was focused on the membrane surface, and the area of the spacer elements was captured. The images had a resolution of 24×10^6 pixels and and were taken every 30 s

[11] Conductivity meter: Mettler Toledo, USA

[12] Carboxylate-modified polystyrene beads: d_p = 1 ± 0.016 µm, ex. 535 nm, em. 575 nm, FluoSpheres, Molecular Probes, USA

throughout the experiment with an exposure time of 1 s. The pixels were 0.8 x 0.8 µm in size. The laser was set to a power of 0.8 W and controlled to illuminate the test section only during image acquisition to avoid bleaching of the fluorescent beads. The process of image analysis was done similarly to subsection 3.1.5.

5.2 Results and Discussion

This section aims to assess whether pulsating flows can reduce fouling on a laboratory scale. The first subsection examines the influence of pulsating flows on permeate water flux and reverse salt flux. The consecutive subsection analyzes temporal deposition data for the three studied cases. Afterward, average deposition after four hours is compared to the study of Bogler et al. [46]. The last subsection investigates the influence of pulsating flows on spatial deposition patterns.

5.2.1 Influence of Feed Flow Pulsations on Permeate Water Flux and Reverse Salt Flux

Three different hydrodynamic conditions were investigated: steady-state, pulsations with a frequency of 5 Hz, and 10 Hz. The permeate water flux j_W was measured continuously during the experiment and averaged over four hours. The reverse salt flux j_S was calculated from measured conductivity in the feed solution before and after the experiment.

Figure 5.4 shows j_W and j_S for a frequency f of 0, 5, and 10 Hz. No significant differences ($p > 0.05$) were observed in either j_W or j_S. Here, FO was used to treat artificial wastewater that contained a small number of ions ($\kappa_C < 1.2\,\mathrm{mS\,cm^{-1}}$). Additionally, the feed solution mass transfer coefficient k (cf. Eq. 2.30) was more than one magnitude higher than the permeate water flux j_W at steady-state. A low ion concentration in the feed solution and a high ratio of k to j_W indicate low external concentration polarization (ECP). The impact of ECP on permeate water flux and

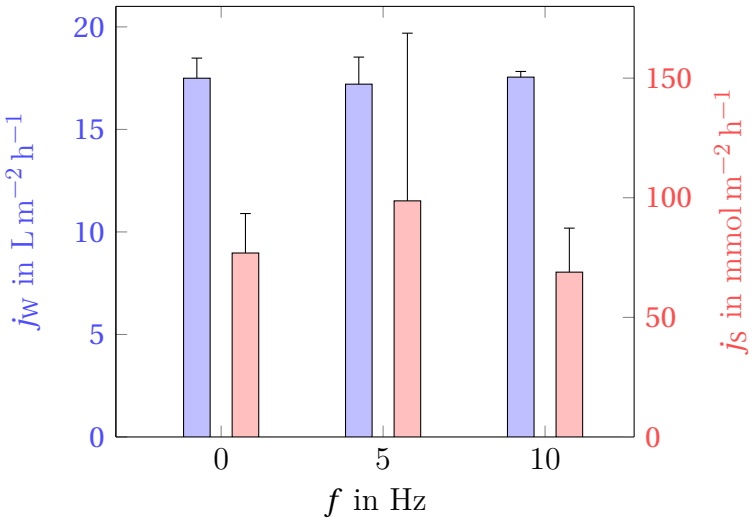

Figure 5.4: Permeate water flux j_W and reverse salt flux j_S for the three investigated cases.

reverse salt flux can be calculated by equation 2.24 and 2.25. ECP on the feed side leads to a change of 0.3 % in permeate water flux j_W and 16 % in reverse salt flux j_S. Although pulsations increase mixing, the possible difference in the measurements was smaller than the standard deviation. Concluding, permeate water flux and reverse salt flux are similar under steady-state and pulsating flow conditions, which is a requirement of the following particle deposition study.

5.2.2 Accumulation Rates at Pulsating Feed Flows

In all cases, particles started to deposit immediately after beads were added to the feed solution. The normalized particle count DP increased over time (cf. Fig. 5.5a). After 2 minutes of deposition, a significant difference ($p < 0.05$) was measured between steady-state (17 ± 13 beads mm^{-2}) and pulsating flow experiments at 10 Hz (6 ± 6 beads mm^{-2}). The DP measured at 10 Hz was significantly lower than DP at 5 Hz and DP at steady-state throughout the experiment.

Pulsations increase fluid shear and enhance mixing, which both affect particle deposition. Ion concentration close to the membrane surface changes the

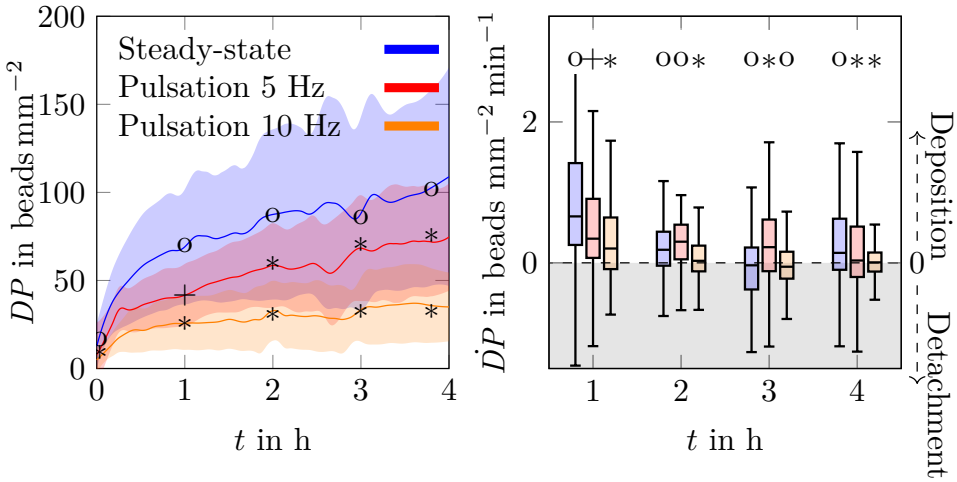

(a) Number of deposited particles DP over time t.

(b) Accumulation rate $\dot{DP}$ of particle deposition over time t.

Figure 5.5: Analysis of deposition DP over time t. Significantly different groups (*, +, o) were obtained by ANOVA analysis.

electrostatic properties of the polystyrene beads and the membrane [61,64], which are both negatively charged. Studies have shown that an increase in ion concentration will lead to a decrease in electrostatic repulsion of surfaces with the same charge, and therefore to an increase in deposition of particles [34, 65]. It is surmised that the increase in mixing led to less concentration polarization due to back-diffusion and less deposition when operating the system with pulsating flows. Concomitantly, particles were affected by both permeation drag and lift force that counteract each other (cf. Sec. 2.3.2). Pulsating flows periodically increase fluid shear on the membrane surface [114] which increases lift forces and contributes to the reduction of fouling development.

The accumulation rate $\dot{DP}$, which is the slope of DP over t, was calculated as the number of particles that deposited or detached within one time step. During the first hour, $\dot{DP}$ was 1.5 times higher at steady-state than at 5 Hz and 2.7 times higher than at 10 Hz (cf. Fig 5.5b). After four hours, $\dot{DP}$ was 15 times higher at a steady-state than at flow pulsations of 10 Hz. The

accumulation rates $\dot{DP}$ decreased over time t.

A lower accumulation rate $\dot{DP}$ eventually leads to less deposition. Three factors might be involved in the reduction of the particle accumulation rate $\dot{DP}$ over time t. The concentration of sodium chloride in the draw solution decreased by 3 % over four hours. Less driving force leads to less permeate water flux across the membrane and less accumulation rate $\dot{DP}$ of polystyrene beads (cf. Sec. 4.2.4). At the same time, electrostatic effects might also play a role, as particles that have already been deposited will decrease the likelihood of further attachment of particles with the same charge (cf. Sec. 2.3.4). Additionally, multiple particles that have deposited in close vicinity to each other can not be distinguished with the chosen microscopic approach.

5.2.3 Impact of Pulsating Feed Flows on Average Deposition

The ratio σ of permeate water flux j_W to crossflow velocity u_F has previously been used to explain the impact of steady-state hydrodynamics on particle deposition [46, 81]. However, u_F is not constant over time and oscillates around the mean value $\bar{u}_F$ at pulsating flows. The mean value $\bar{\sigma}$ corresponds to the mean value of the crossflow velocity $\bar{u}_F$ and illustrates the impact of pulsating flows on particle deposition (cf. Fig 5.6).

At steady-state, $\bar{\sigma}$ was equal to σ, as the crossflow velocity u_F was constant. Experiments at steady-state resulted in a normalized deposition count DP of $37 \pm 10\,\mathrm{beads\,mm^{-2}}$ at $\bar{\sigma} = 1.2 \times 10^{-5}$ [46]. At $\bar{\sigma} = 3.5 \times 10^{-5}$, DP was $109 \pm 62\,\mathrm{beads\,mm^{-2}}$. The deposition count DP was $349 \pm 37\,\mathrm{beads\,mm^{-2}}$ at a ratio $\bar{\sigma}$ of 6.1×10^{-5} [46]. Previous research indicated that the initial deposition of similar polystyrene beads is closely related to $\bar{\sigma}$ [46]. DP decreases when $\bar{\sigma}$ is reduced, which agrees with the results of the present study.

Considering pulsating flows, the frequency and measured amplitude $\tilde{u}_F$ differed. The mean ratio of permeate water flux to crossflow velocity $\bar{\sigma}$ was constant at 3.5×10^{-5}. Flow pulsations of 5 Hz frequency led to a

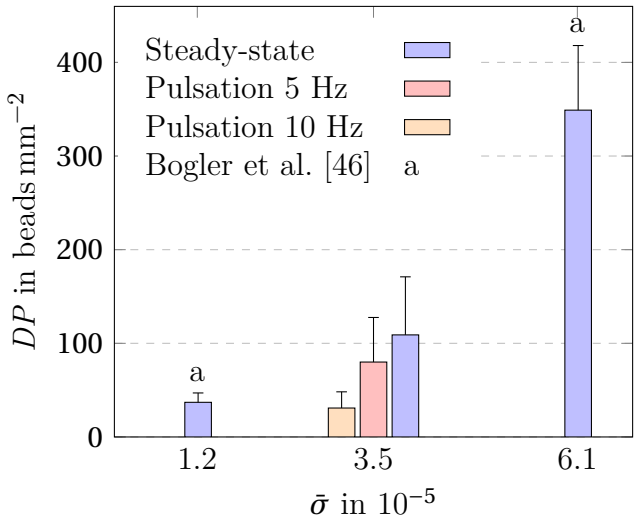

Figure 5.6: Particle deposition DP over mean ratio $\bar{\sigma}$ of permeate water flux j_W to crossflow velocity u_F after 4 hours of deposition experiment. The standard deviation is depicted by error bars.

Table 5.2: Comparison of pulsating flow and steady-state experiment with similar crossflow velocity $\bar{u}_F$.

Experiment	$\bar{u}_F$ in cm s^{-1}	j_W in L m^{-2} h^{-1}	DP in beads mm^{-2}
Steady-state	13.7	6.4	37
10 Hz	13.7	17.6	31

normalized deposition count DP of 80.0 ± 47.6 beads mm^{-2}. At 10 Hz, experiments resulted in a DP value of 30.9 ± 17.3 beads mm^{-2}. DP at steady-state was 1.2 times higher than with pulsations of 5 Hz and three times higher than with pulsations of 10 Hz, even though the mean crossflow velocity $\bar{u}_F$ and permeate water flux j_W were the same.

The steady-state experiment at a $\bar{\sigma}$ value of 1.2×10^{-5} corresponded to the same mean crossflow velocity $\bar{u}_F = 13.7$ cm s^{-1} as used in this study, but a lower permeate water flux $j_W = 6.4 \pm 0.8$ L m^{-2} h^{-1}. At 10 Hz, DP was 1.2 times lower although the permeate water flux was 2.7 times higher (cf. Tab. 5.2). Hence, the permeate water flux j_W can be increased without the drawback of increased deposition DP by applying pulsating feed crossflow velocities.

Although the amplitude $\tilde{u}_F$ was 1.3 times lower at 10 Hz than at 5 Hz, DP decreased by a factor of 2.6. Pulsations do affect deposition, though the increase in amplitude $\tilde{u}_F$ can not solely explain the effect. An increase in $\tilde{u}_F$ increases the fluid shear on the membrane surface [114], which decreases the attachment probability of particles [115]. An increase in frequency f also increases fluid shear on the membrane surface and may lead to a detachment of particles from the membrane surface [38]. Therefore, it can be concluded that both amplitude $\tilde{u}_F$ and frequency f are essential parameters when discussing the fouling mitigation potential of pulsating flows.

5.2.4 Spatial Distribution of Particle Deposition

The spatial resolution of particle deposition within a spacer element was recorded by fluorescence microscopy. Spacer filaments impose flow restrictions and force the flow to enter the spacer element under filament I and over II while leaving under III and over IV (cf. Fig 5.7a). For further investigation of the deposition pattern, the spatial distribution of deposition was separated into nine zones (cf. Fig 5.7b).

Figures 5.7c-e show the spatial distribution of deposited particles DP in a spacer element for the three studied cases after 4 h. Numbers indicate the percentage of deposited particles in one patch out of the whole element. DP in each region j was normalized by the steady-state value $DP_{j,0}$ and visualized by the color scale. ANOVA analysis revealed regions that had a significantly lower (o) or higher (*) DP value.

At a steady state, the DP within the NE zone was significantly higher (22%) than DP in the N, W, SW, and S elements (cf. Fig 5.7c). When the fluid is forced to pass under spacer filament I, the fluid shear increases immediately downstream of that filament and DP decreases in zone W, SW, and S. At the same time, before the flow passes filament III, particles are forced closer to the membrane surface leading to an increase in DP in zone NE.

At 5 Hz, DP was at least three times higher in the E, NE, and SW ele-

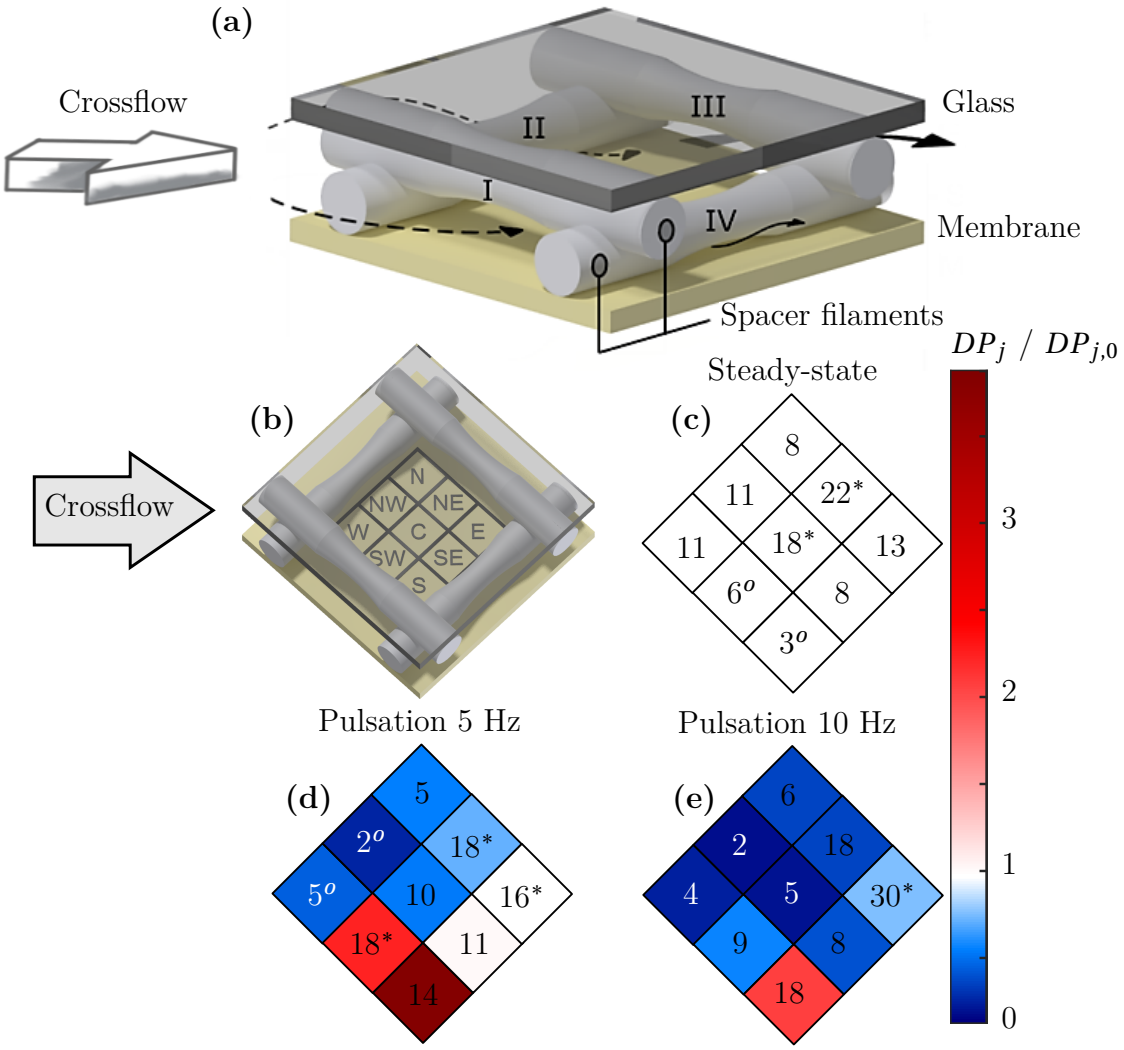

Figure 5.7: (a) Spacer element. (b) Separation of patches. (c-e) Spatial distribution of deposited particles.

ment than the NW and W element (cf. Fig 5.7d). At 10 Hz, most particles deposited in the E zone (cf. Fig 5.7e). The deposition DP was significantly lower in every other zone. Few particles deposited in regions close to filament II (W, NW, N) and between filaments I and III (NW, C, SE).

Compared to steady-state, the total deposition was less at 10 Hz. Total deposition decreases because deposition DP in most regions decreases. However, DP increased in region S by a factor of 2 from $30 \pm 38\,\mathrm{beads\,mm^{-2}}$ to $67 \pm 87\,\mathrm{beads\,mm^{-2}}$. Pulsating flows have little influence on the deposition DP close to the junction of III and IV and increase particle transport to the membrane near junction IV, and I. Particles are known to deposit close to spacer filaments and especially filament junctions [43,83,97]. Deposition can be reduced in most regions by pulsating flows, but a higher deposition in one region is a drawback that needs consideration. It is suggested that further increasing the frequency beyond 10 Hz would increase shear on the membrane surface and reduce deposition in region S. Another possibility would be optimizing the spacer geometry. Perforated spacers are more fouling resilient than conventional spacers [116], and pulsating flows might increase the resilience even more.

Homogeneity is the ratio of DP in the zone with the highest deposition to DP in the region with the lowest deposition. Values close to 1 represent cases where deposition is homogeneously distributed, while cases with increasing homogeneity values are those where deposition is concentrated. At steady-state, the deposition had a homogeneity value of 7, while it increased to 9 at 5 Hz, and 14 at 10 Hz pulsations. Similar to a decrease in the ratio σ between permeate water flux j_W to crossflow velocity u_F [46], an increase in the frequency f of pulsating flows leads to a less homogeneous deposition where deposition is concentrated in regions close to spacer filaments, and especially filament junctions. Numeric simulations have shown that an increase in pulsation frequency f increases fluid shear close to spacer filaments [114]. Differentially, an increase in amplitude $\tilde{u}_\mathrm{F}$ did not have the same effect. This explains why the deposition is more heterogeneous in the case of 10 Hz than 5 Hz, although the amplitude $\tilde{u}_\mathrm{F}$ of the pulsation was lower at 10 Hz.

5.3 Conclusion

Pulsation frequency f and amplitude $\tilde{u}_F$ are the two driving variables for fouling mitigation by pulsating flows (cf. Fig. 5.8). Accumulated particle deposition DP, accumulation rate $\dot{DP}$, and homogeneity were highest at steady-state, and lowest at pulsating feed flows of 10 Hz.

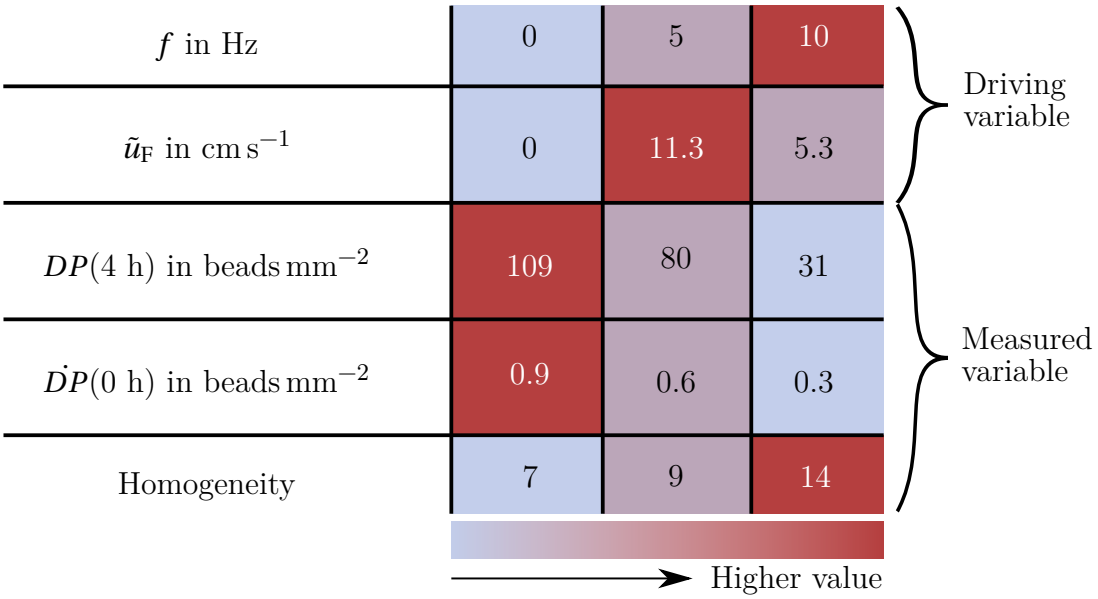

Figure 5.8: Summary of driving and measured variables for the three studied pulsating flow conditions.

In conclusion, the deposition probability was lower at pulsating flows when compared to steady-state. Furthermore, the higher the frequency and amplitude of the pulsating flow, the less deposition occurred on the membrane surface. For further investigation, it is suggested to apply pulsating flows at a frequency f of above 10 Hz and an amplitude $\tilde{u}_F$ above 5.3 cm s^{-1}.

Chapter 5 has shown that the right choice of transient hydrodynamic conditions decreases particle deposition of polystyrene beads with a diameter of 1 µm in FO. However, the impact of hydrodynamics on qualitative tendencies of deposition was similar for polystyrene beads and *Bacillus subtilis* (cf. Sec. 4.2.4). It is thus surmised that the insights gained here also apply to the initial deposition of *Bacillus subtilis*.

6 Fouling Propensity in a Spiral-Wound Module

The two research aims of the dissertation are to investigate the impact of steady-state and transient hydrodynamic conditions on particle deposition in forward osmosis (FO). Chapters 3 and 5 have shown that an appropriate choice of hydrodynamics can reduce particle deposition on laboratory-scale. This chapter transfers the knowledge gained on laboratory-scale to an SWM.

The process parameters permeate water flux and crossflow velocity change along a spiral-wound module (SWM). Previous sections have shown that changing process parameters affect the fluid flow (cf. Sec. 4.2.1), ion concentration at the membrane surface (cf. Sec. 4.2.2), and the fouling propensity of particles (cf. Sec. 4.2.4). Frequency and amplitude were the two driving variables for fouling mitigation by pulsating flows (cf. Chap. 5). However, it can be expected that damping diminishes the amplitude along an SWM.

It is the objective of Chapter 6 to predict hydrodynamics in an FO SWM at steady-state and identify areas that are prone to biofouling at steady-state. Additionally, areas prone to biofouling with pulsating feed flows are to be identified. For that purpose, Chapter 6 determines how the amplitude changes along an SWM and the corresponding damping rates. Subsequently, the FO process is modeled in an SWM in steady-state. Then, a model for damping and fouling mitigation by pulsating flows is integrated into the steady-state model. Lastly, results of permeate water flux and crossflow velocity in an SWM are combined with experimental data of deposition experiments (cf. Ch. 3 and 5).

The results reveal regions prone to fouling in the SWM and provide design guidelines for FO systems at steady-state and pulsating operating condi-

tions, respectively.

6.1 Materials and Methods

First, the governing equations of the steady-state model and the choice of boundary conditions are discussed. Next, the experimental damping system and experimental procedure are introduced.

6.1.1 Steady-State Model of Forward Osmosis in a Spiral-Wound Module

The length L of an SWM is separated into n elements for both the draw and feed channel (cf. Fig. 6.1). Each element has a membrane area A_j. There is a salt flux $j_\mathrm{S,j}$, and a permeate water flux $j_\mathrm{W,j}$ across each membrane area. The salt flux is directed from draw to feed, while the permeate water flux is directed the opposite way. For each element of the SWM, mass and salt balances are solved:

$$\begin{aligned}
\dot{m}_\mathrm{D,j} - \dot{m}_\mathrm{D,j+1} + A_\mathrm{j}\ \rho_\mathrm{W}\ j_\mathrm{W,j} - A_\mathrm{j}\ \rho_\mathrm{S}\ j_\mathrm{S,j} &= 0 \\
\dot{m}_\mathrm{F,j} - \dot{m}_\mathrm{F,j+1} - A_\mathrm{j}\ \rho_\mathrm{W}\ j_\mathrm{W,j} + A_\mathrm{j}\ \rho_\mathrm{S}\ j_\mathrm{S,j} &= 0 \\
w_\mathrm{D,j}\ \dot{m}_\mathrm{D,j} - w_\mathrm{D,j+1}\ \dot{m}_\mathrm{D,j+1} - A_\mathrm{j}\ \rho_\mathrm{S}\ j_\mathrm{S,j} &= 0 \\
w_\mathrm{F,j}\ \dot{m}_\mathrm{F,j} - w_\mathrm{F,j+1}\ \dot{m}_\mathrm{F,j+1} + A_\mathrm{j}\ \rho_\mathrm{S}\ j_\mathrm{S,j} &= 0.
\end{aligned} \tag{6.1}$$

The permeate water flux $j_\mathrm{W,j}$ and salt flux $j_\mathrm{S,j}$ are calculated by equations 2.24 and 2.25. The membrane parameters K, B, and S were obtained from table 4.2. Kim et al. [21] published operating conditions for an 8" spiral-wound FO module. These include volume flow rates $\dot{V}$, crossflow velocities u_F, salt mass fractions w, total membrane area A, and length L of the SWM (cf. Table 6.1). They used sodium chloride as draw solute.

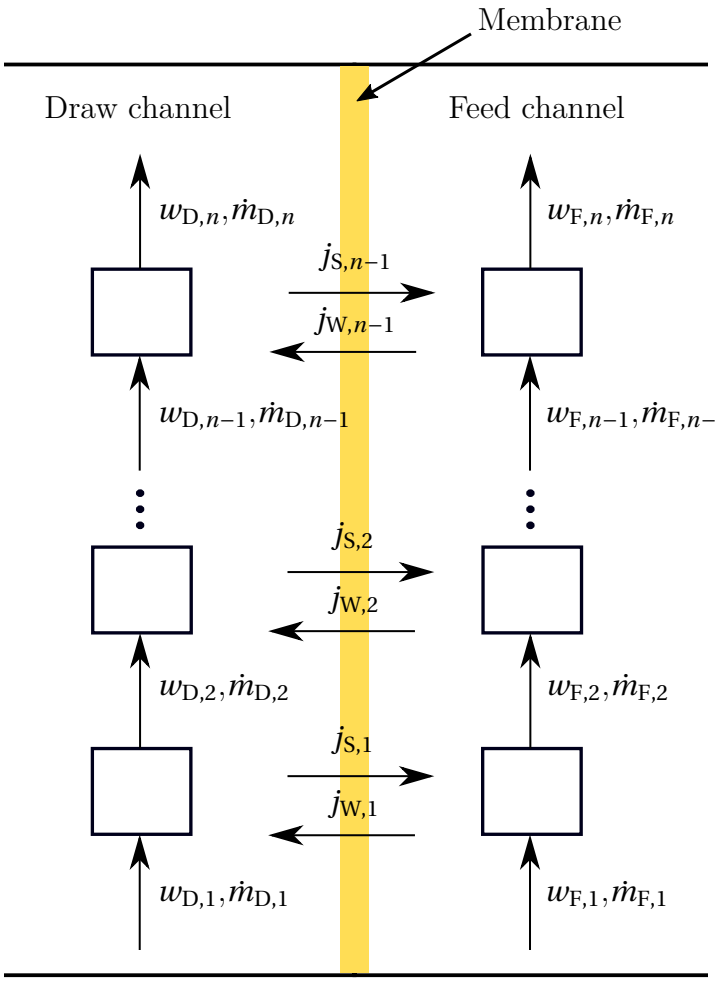

Figure 6.1: Separation of SWM into n elements for draw (D) and feed (F) channel.

Table 6.1: Parameters of the FO system model.

Parameter	Value	Unit
$\dot{V}_F$	17	$L\,min^{-1}$
$\dot{V}_D$	10	$L\,min^{-1}$
u_F	16	$cm\,s^{-1}$
u_D	4	$cm\,s^{-1}$
w_F	0	$g\,L^{-1}$
w_D	35	$g\,L^{-1}$
A	15	m^2
L	1	m

6.1.2 Modeling Fouling Propensity in a Spiral-Wound Module

The deposition probability $\Psi_{BS,exp}$ of *Bacillus subtilis* was proportional to j_W / u_F^2 at steady-state (cf. Eq. 4.10). Although the deposition probability of *Bacillus subtilis* and polystyrene beads differed in quantitative values, the qualitative impact of hydrodynamics was similar (cf. Sec. 4.2.4). It was thus assumed that *Bacillus subtilis* would react to pulsations the same way as polystyrene beads. The deposition probability Ψ can then be calculated as

$$\Psi = \Psi_{BS,exp} \left(1 - 0.07\ f\ \frac{\tilde{u}_F(x)}{\tilde{u}_{F,exp}}\right). \tag{6.2}$$

Ψ is a linear regression fit of the results of Chapter 5 (cf. Fig. 5.8). The frequency f and oscillating velocity $\tilde{u}_F$ were the two driving parameters in the pulsating flow experiments. The fluid flow is at steady-state when f or $\tilde{u}_F$ are equal to zero. At steady-state, the deposition probability Ψ has to be equal to the steady-state value $\Psi_{BS,exp}$. At a frequency f of 10 Hz and $\tilde{u}_{F,exp}$ of 5.3 cm s^{-1}, the deposition count was 27 % of the steady-state value. The deposition count was 70 % of the steady-state value at $f = 5$ Hz and $\tilde{u}_{F,exp} = 11.3$ cm s^{-1}. The oscillating velocity at the beginning of the module $\tilde{u}_F(x = 0)$ was set to 5.3 cm s^{-1}.

6.1.3 Experimental Damping Test Rig

Reverse osmosis permeate (ROP) was forced through the system (cf. Fig. 6.2) by a gear pump[1]. Pulsating flows were initiated by a valve[2]. The pulsation amplitude $\tilde{u}_F$ was controlled by varying the duty value. The absolute pressure p_{abs} was measured close to the orifices[3]. An RO SWM[4] with an effective length of 0.43 m was chosen for the investigation. It was assumed

[1]Gear pump: Liquiflo Equipment Company, USA
[2]Pulsating valve: Landefeld Druckluft und Hydraulik GmbH, Germany
[3]Absolute pressure sensors: 0 to 4 bar, and 0 to 2 bar, Keller Ag für Druckmesstechnik, Winterthur, Switzerland
[4]SWM: SW30-2521, Toray, Japan

that the damping behavior of an RO SWM that is operated near ambient pressure is similar to an FO SWM as both contain membrane sheets that are separated by a spacer. Two identical orifices were printed with a resin 3D printer[5]. Both orifices were equipped with differential pressure sensors[6]. The volume flow rate $\dot{V}$ was continuously measured by a magnetic flow meter[7]. The permeate channel of the SWM was closed.

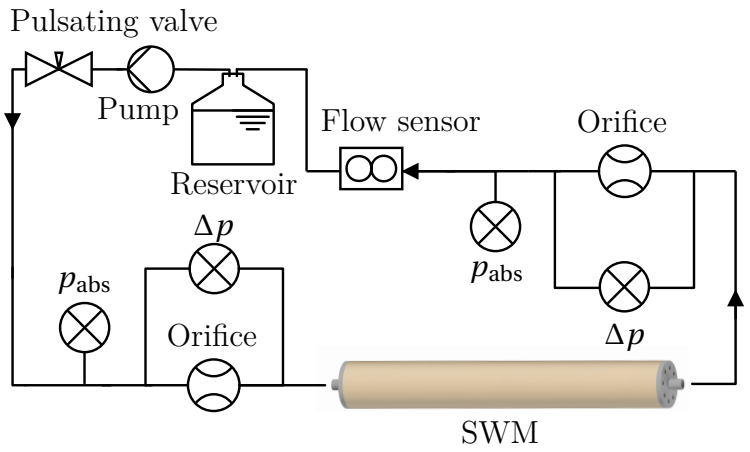

Figure 6.2: Schematic of damping experiment. The transient fluid velocity was measured upstream and downstream of the SWM.

6.1.4 Experimental Procedure

The calibration of each orifice followed the approach described in section 5.1.2. Steady-state experiments led to an A_{orifice} value of $6.2 \times 10^9\,\text{m}^{-4}$ for the upstream orifice and $A_{\text{orifice}} = 6.4 \times 10^9\,\text{m}^{-4}$ for the downstream orifice (cf. Fig. A.2). Pulsating flow experiments (cf. Tab. A.1) resulted in a B_{orifice} value of 0.03 (cf. Fig. A.3).

The damping experiment was based on the assumption that the temporal resolution of the measurement was high enough to register the velocity changes of the fluid. The pulsation frequency did not exceed 10 Hz. Addi-

[5]Resin 3D printer: Elagoo Inc., China
[6]Differential pressure sensors: -1 to 1 bar, and -0.5 to 0.5 bar, Keller Ag für Druckmesstechnik, Winterthur, Switzerland
[7]Volume flow sensor: Optiflux 5100C, DN6, Krohne Messtechnik GmbH, Duisburg, Germany

tionally, the length of the pipes between orifices and differential pressure sensors was short (0.2 m). A change in differential pressure reaches the corresponding sensor in approximately 0.14 ms. The temporal resolution of the system is thus high enough to register velocity changes of the fluid at a pulsation frequency of 10 Hz.

A harmonic feed flow pulsation $u_F(x,t)$ with mean value $\bar{u}_F$ and initial oscillating velocity $\tilde{u}_F$ propagates through an SWM as

$$u_F(x,t) = \bar{u}_F + \tilde{u}_F \; e^{-\alpha x} \; \sin \omega t. \tag{6.3}$$

Here, α is the damping rate. α was calculated with measurements of the oscillating velocity upstream $\tilde{u}_{F,1}$ and downstream $\tilde{u}_{F,2}$ of the SWM

$$\alpha = \frac{1}{L} \; \ln \frac{\tilde{u}_{F,1}}{\tilde{u}_{F,2}}. \tag{6.4}$$

Damping experiments were conducted for frequencies f of 3.25, 5.5, 7.25, and 10 Hz. Volume flow rates $\dot{V}$ were varied between 40, 70, and 100 L h^{-1}. Higher $\dot{V}$ were not possible with the test-rig. The duty value was chosen between 0.3 and 0.5.

6.2 Results and Discussion

First, damping results of an RO SWM are presented. It was assumed that damping rates of an FO SWM would be similar (cf. 6.1.3). The fouling propensity of a steady-state FO module is discussed next. The steady-state model, damping experiments, and fouling experiments at pulsating flows are combined into fouling propensity at pulsating flows. Lastly, design guidelines for an FO system with feed flow pulsations are derived.

6.2.1 Damping Rates of a Spiral-Wound Module

Damping rates α were calculated for several volume flow rates $\dot{V}$ and frequencies f (cf. Fig. 6.3). For both 70, and 100 $\mathrm{L\,h^{-1}}$, α increased propor-

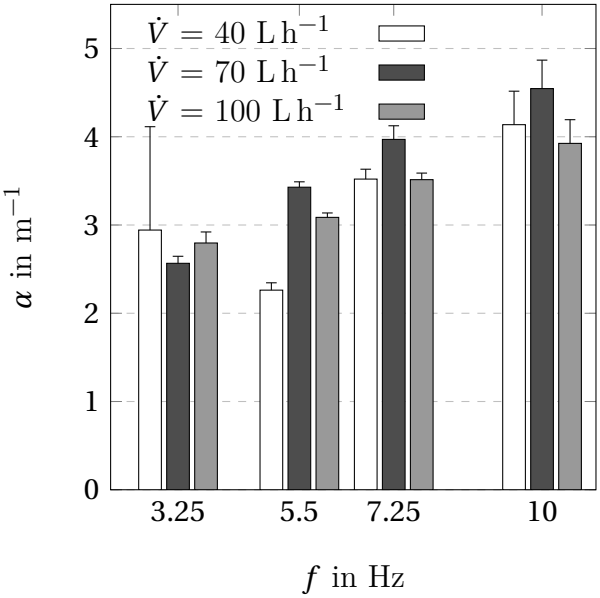

Figure 6.3: Damping rate α over frequency f and volume flow rate $\dot{V}$. The standard deviation is depicted by an error bar.

tional ($R^2 > 0.78$, $\mathrm{p} < 0.01$)[8] to an increase in f

$$\alpha(f) = 2.00 + 0.22\ f. \tag{6.5}$$

No statistically significant influence ($\mathrm{p} > 0.05$) of α to $\dot{V}$, absolute pressure, and oscillating crossflow velocity upstream of the SWM $\tilde{u}_{\mathrm{F},1}$ was observed. Additionally, there was no significant phase shift between the differential pressure measurement upstream and downstream of the SWM.

Meißner et al. [117] analyzed the damping behavior of viscoelastic piping. They state that the damping rate α is the sum of two factors: viscoelastic damping and fluid friction. While fluid friction dominates at low frequencies, an increase in pulsation frequency f increases the importance of vis-

[8] Correlations were tested with Pearson's correlation test (cf. Sec. 3.1.7). In this context, p denotes the significance level, while R^2 is the proportion of variance square. A correlation was regarded as significant when p was below 0.05.

coelastic damping. The same behavior was observed in the present study for SWMs at volume flow rates $\dot{V}$ of 70, and 100 $\mathrm{L\,h^{-1}}$.

In the case of 40 $\mathrm{L\,h^{-1}}$, the correlation of frequency f and damping rate α was not statistically significant ($p > 0.05$). The standard deviation was high at a f of 3.25 Hz. The noise of the differential pressure sensor had more influence on measurements at small volume flow rates, which led to higher standard deviations at low $\dot{V}$.

It is important to note that SWMs are commonly operated at crossflow velocities u_F ranging from 0.04 to 0.163 $\mathrm{m\,s^{-1}}$ [22, 87]. In the case of the SW30-2521, these values would require a volume flow rate $\dot{V}$ of 216 to 880 $\mathrm{L\,h^{-1}}$. However, technical limitations of the pump and the pulsating valve made it necessary to limit the experiments to volume flow rates of 100 $\mathrm{L\,h^{-1}}$ and below. No significant dependency of damping rates α to $\dot{V}$ was observed (cf. Fig. 6.3). It is thus expected that an increase in frequency f will also increase damping rates α at higher volume flow rates $\dot{V}$. It was also assumed that permeation does not change the amplitude $\tilde{u}_F$ of flow pulsation. This assumption is valid, as long as no significant dependence of damping rates α to volume flow rates $\dot{V}$ was observed.

6.2.2 Steady-State Fouling Propensity

The system can be set up as a co-current (CO) and a counter-current (CC) configuration. In the CO configuration, feed and draw have the same flow direction, while directions are opposite in the CC configuration.

Figure 6.4 shows the results of the steady-state system simulation. The feed crossflow velocity u_F decreases along the SWM by 45 % at CO and CC. The permeate water flux j_W decreases by 26 % at CO and increases by 26 % at CC. The reverse salt flux j_S decreases by 22 % at CO and increases by the same value at CC.

Both j_W and j_S are linear proportional to the concentration difference of feed and draw solution (cf. Eq. 2.14 and 2.15). The highest concentration difference can be found at the feed inlet ($x = 0$ m) at CO and at the feed

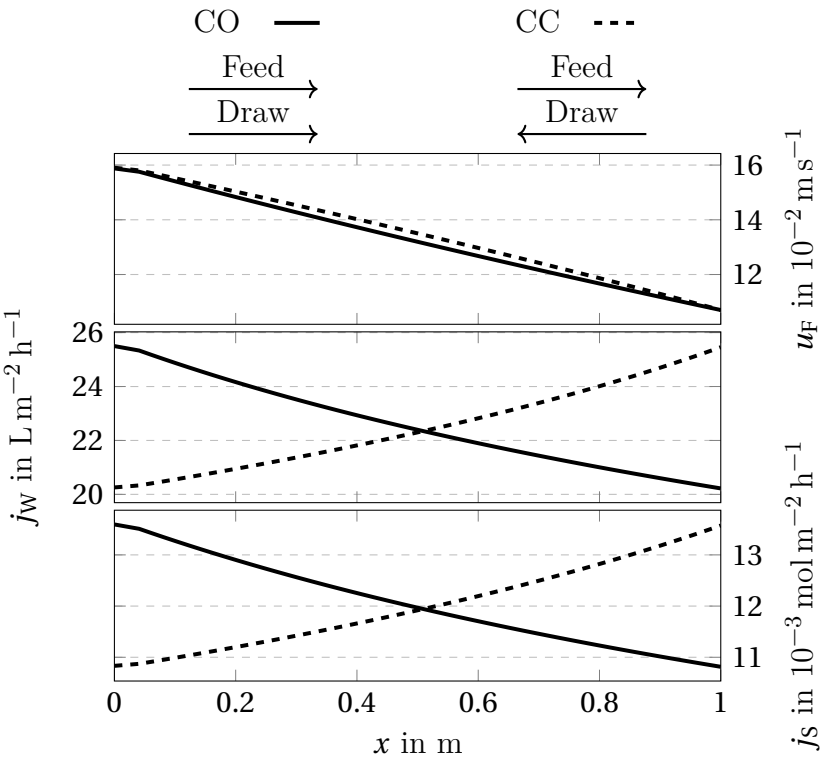

Figure 6.4: System simulation of FO in co-current (CO) and counter-current (CC) configuration. Feed crossflow velocity u_F, permeate water flux j_W, and reverse salt flux j_S over position x in the SWM.

outlet ($x = 1\,\mathrm{m}$) at CC. A high permeate water flux j_W and salt flux j_S indicates high external concentration polarization (ECP) on the feed side (cf. Eq. 2.24 and 2.25). A high ion concentration at the membrane decreases the energetic barrier for cell attachment (cf. Sec. 2.3.4). When only the energetic barrier is considered, it is more likely for *Bacillus subtilis* to attach at the feed inlet ($x = 0\,\mathrm{m}$) at CO and at the feed outlet ($x = 1\,\mathrm{m}$) at CC.

Fig. 6.5 shows the deposition probability Ψ of *B. subtilis* along an SWM for both CO and CC configuration. Instead of the normalized deposition count DP, it was chosen to show the deposition probability Ψ in this chapter, as Ψ is independent of the particle concentration in the feed solution (cf. Eq. 4.8). Ψ increased by 22 % at CO and by 44 % at CC. Ψ of CO was 6 %

higher than Ψ of CC at the feed inlet of the module. At the feed outlet of the module, Ψ was 10 % higher at CC than at CO.

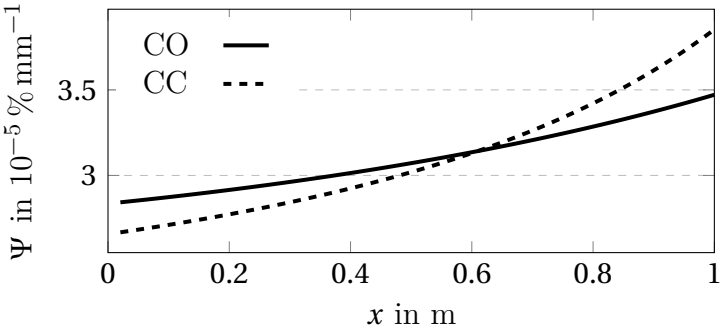

Figure 6.5: Deposition probability Ψ over position x in the SWM at co-current (CO) and counter-current (CC) configuration.

At CC and CO, the deposition probability Ψ was higher at the feed outlet than at the feed inlet. The studies conducted in this dissertation are valid for initial cake layer formation in FO. As far as the author is aware, fouling propensity distribution has not been modeled in an FO SWM so far. However, biofouling has been studied in full scale RO and NF plants [118–120]. A comparison of the results obtained in the present study to biofouling is difficult. While bacteria deposit similarly to inert beads in the initial stage of cake layer formation [48], the consecutive biofilm formation and growth is severely affected by the amount of nutrients and oxygen in the feed solution [3, 121, 122]. Nevertheless, it should be mentioned that the literature is not univocal on the position of the highest amount of biofilm formation in an SWM. In most cases [23], the highest amount of biofilm develops in the first halve of the lead module [119, 120, 123]. At the feed inlet, the feed crossflow velocity is highest thus the biofilm is well supplied by nutrients and oxygen. However, a higher amount of biofilm at the feed outlet than at the feed inlet has also been observed [118, 119]. In summary, it is possible that the deposition probability Ψ is higher at the feed outlet than at the feed inlet as calculated in this dissertation.

This section has shown that fouling propensity can be estimated along an FO SWM with the tools developed in this dissertation. Additionally, areas prone to fouling can be identified.

6.2.3 Fouling Propensity at Pulsating Flow

The steady-state system model can now be extended to contain pulsating flows. The damping rate α (cf. Eq. 6.5) of an RO SWM was used to calculate the pulsating crossflow velocity $u_F(x,t)$ in an FO SWM (cf. Eq. 6.3).

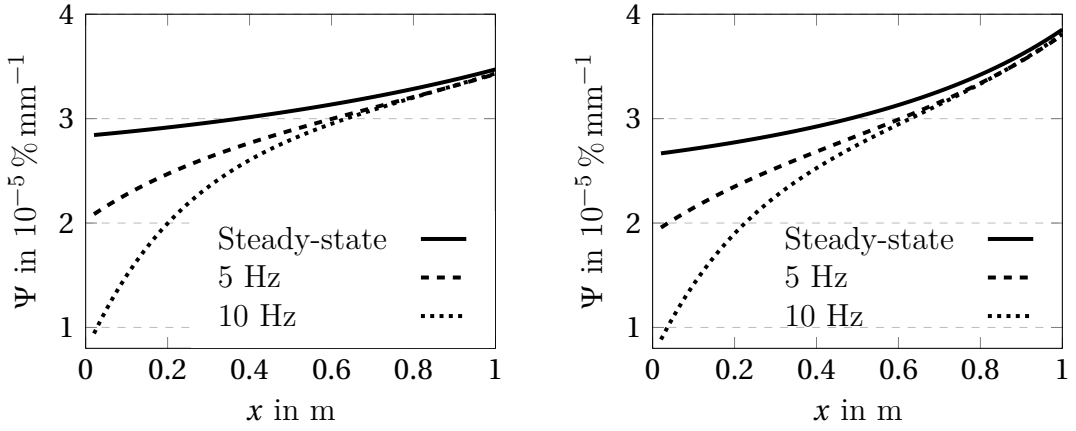

(a) Deposition probability Ψ over position x at CO configuration.

(b) Deposition probability Ψ over position x at CC configuration.

Figure 6.6: Fouling propensity in an SWM for CO and CC configuration under pulsating flow conditions.

Figure 6.6a shows the deposition probability Ψ in an SWM for steady-state, 5 Hz, and 10 Hz pulsations in the CO configuration. At 10 Hz, Ψ is 2.2 times lower than at 5 Hz and 3.0 times lower than at steady-state at the feed inlet of the module ($x = 0\,\mathrm{m}$). In CC configuration (cf. Fig. 6.6b), Ψ is 3.0 times higher at steady-state than at 10 Hz and 1.3 times higher than at 5 Hz. Damping diminishes the benefits of pulsating flows over the length of the module. There is no fouling mitigation at the feed outlet of a module with a length of 1 m.

In both cases, CO and CC, a high pulsation frequency leads to less fouling along the module than a low pulsation frequency. Hence, only pulsations with 10 Hz frequency will be considered when optimizing the FO system in the following subsection.

The support layer is thinner in FO than in pressure based system such as RO and NF (cf. Sec. 2.2.3). The FO membrane is less resilient to pressure than RO or NF membranes due to the thin support layer. Placing the pulsating valve downstream of an SWM would increase the average pressure in the SWM which should be avoided in FO. In pressure-based systems, the pulsating valve can be installed downstream of the SWM [39], which leads to more flexibility in system design.

6.2.4 Optimizing the Pulsating Flow Forward Osmosis System

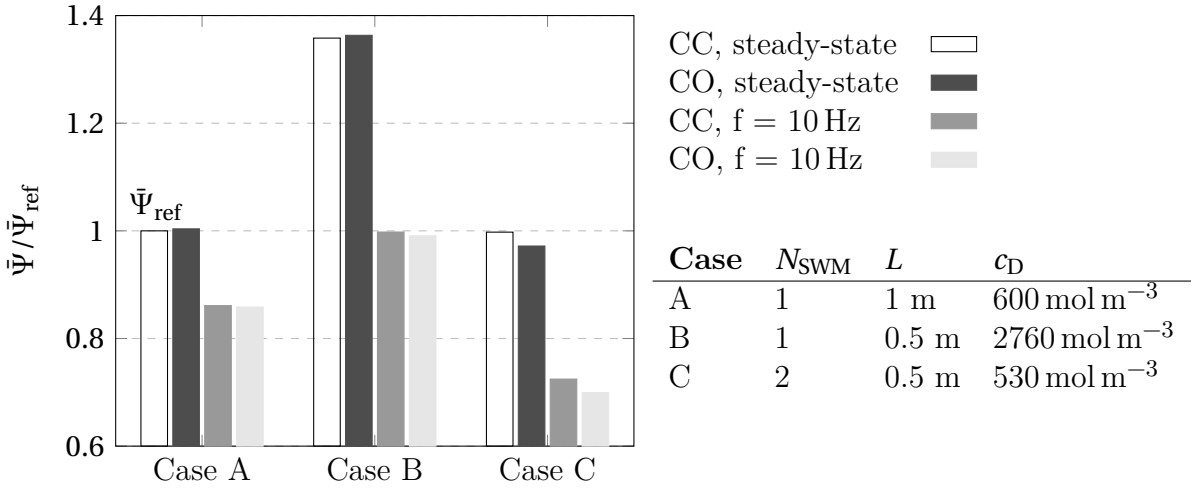

Case	N_{SWM}	L	c_{D}
A	1	1 m	$600\,\mathrm{mol\,m^{-3}}$
B	1	0.5 m	$2760\,\mathrm{mol\,m^{-3}}$
C	2	0.5 m	$530\,\mathrm{mol\,m^{-3}}$

Figure 6.7: Average deposition probability along the SWM $\bar{\Psi}$ normalized by the reference $\bar{\Psi}_{\mathrm{ref}}$. The permeate water flow was constant in all cases.

So far, the FO system consisted of an SWM with a length of one meter. The previous subsection has shown that damping diminishes the fouling mitigation potential of pulsating flows along the SWM. Hence, a single, long SWM might not be the best choice. The current subsection investigates alternative options.

Figure 6.7 depicts the average fouling propensity $\bar{\Psi}$ along the SWM with reference to $\bar{\Psi}_{\mathrm{ref}}$ for three cases. Case A represents the case that has been studied so far. CC at steady-state is chosen as reference value $\bar{\Psi}_{\mathrm{ref}}$. In all

cases, the permeate water flow is held constant. The number of parallel SWMs N_{SWM}, length L, and sodium chloride concentration in the draw solution c_{D} is varied.

The length of the module L is half in Case B than in Case A. The concentration c_{D} is increased to $2760\,\mathrm{mol\,m^{-3}}$ to maintain a constant permeate water flow. This draw concentration would require a less energy efficient regeneration step than RO as it is much higher than the usual operation range of sea water RO, which is up to $1370\,\mathrm{mol\,m^{-3}}$ [104]. In Case B, the deposition probability $\bar{\Psi}$ is higher than the reference $\bar{\Psi}_{\mathrm{ref}}$ at steady-state. Even with pulsating flows, $\bar{\Psi}$ is just sightly lower than $\bar{\Psi}_{\mathrm{ref}}$. Pulsating flows have more fouling mitigation potential in a short SWM. However, the permeate water flow has to be the same in Case B as in Case A. Hence, the permeate water flux is doubled. The increase in permeate water flux negates the positive effect of pulsating flows in Case B. Reducing the length of the SWM is thus not a viable option when the permeate water flux has to be increased.

The SWM length L is halved in Case C, but N_{SWM} is doubled. The volume flow rate of the system has to be constant. Hence, the crossflow velocity u_{F} at the feed inlet of Case C is half than u_{F} in Case A. In a short SWM, the mean osmotic pressure difference between feed and draw is higher than in a long SWM. The parallel setup of SWMs thus leads to a decrease of c_{D}. In Case C and at pulsating flow conditions, the fouling propensity $\bar{\Psi}$ at CO is 3.4 % less than at CC. Compared to steady-state (CO), pulsating flows decrease $\bar{\Psi}$ by up to 27.0 %.

The parallel setup of Case C (CO, f = 10 Hz) decreases $\bar{\Psi}$ of Case A (CO, f = 10 Hz) by an additional 15.9 %. Compared to the reference case (Case A, CC, steady-state), the modified setup (Case C, CO, f = 10 Hz) reduces the deposition probability $\bar{\Psi}$ by 30.0 %. Case C exhibits the lowest fouling propensity with CO configuration. It is thus suggested to configure a pulsating FO system in parallel with short SWMs in CO configuration.

This subsection optimized the pulsating FO system with a focus on initial cake layer formation. Bacteria that have deposited on the membrane sur-

face proliferate and form a biofilm. Biofilm formation leads to less permeate water flux and an increase in pressure drop along the membrane module. The common cleaning approach is a combination of physical and chemical cleaning [12, 17]. Although chemical cleaning removes most of the cake layer, foulants deposited in membrane pores remain [12, 17]. Additionally, the use of chemical agents shortens the membrane life, reduces membrane selectivity, consumes additional energy, and produces a problematic waste stream [12]. Although two SWMs are initially more expensive than a single SWM, the fouling optimized setup might be the best choice over the lifespan of an SWM when also considering the negative impact of cleaning approaches.

6.3 Design Guidelines

This chapter has investigated fouling propensity in an SWM at steady-state and pulsating flow conditions. At steady-state, the deposition probability was highest at the feed outlet of the module. Concomitantly, the CC configuration was better than the CO configuration in the first half of the module but worse in the second half. Damping increased with an increase in frequency. No dependency of damping on amplitude and volume flow rate was found. Although damping rates were higher at high-frequency pulsations, high-frequency pulsations were better suited to mitigate fouling in SWMs. The following design guidelines can be gathered from the results:

- The higher the amplitude and frequency of the pulsating flows, the higher the fouling mitigation potential.
- The length of the SWM should be as short as possible due to damping effects.
- A simultaneous decrease in length of the SWM and increase in ion concentration in the draw solution is not an option.
- The optimized setup are two short SWM in parallel configuration with

high pulsation amplitude and frequency in CO configuration instead of one long SWM.

7 Summary and Conclusion

This dissertation had two objectives. The first objective was to investigate the impact of steady-state hydrodynamics on cake layer formation in a forward osmosis spiral-wound module. The second objective was to assess the potential of pulsating feed flows to mitigate cake layer formation.

The objectives were pursued by investigating the influence of permeate water flux, crossflow velocity, and pulsating flow on the deposition behavior of particles in a forward osmosis system. Several methods were developed to help analyze deposition in a forward osmosis system and achieve a detailed understanding of deposition. These methods include experimental approaches and simulation methods:

- An experimental approach to investigate the initial deposition of stained bacteria and inert beads in forward osmosis. Fluorescence microscopy and laser-induced fluorescence microscopy made it possible to gather in-situ information on the deposition process. The high contrast between particles and background made quantification of deposition possible. The impact of permeate water flux, crossflow velocity, and pulsating flows on particle deposition was investigated with these methods.

- Mass transport phenomena in forward osmosis were analyzed by computational fluid dynamics. The forces acting on particles could be determined with detailed information about fluid flow and salt mass fraction in the channel. The calculated forces were used to predict the deposition probability of particles.

- The damping behavior of a reverse osmosis spiral-wound module was investigated in experiments. Two orifices were placed upstream and

downstream of the spiral-wound module. Differential pressure measurements across the orifices were used to calculate the transient velocity. The change in transient velocity was then related to damping.

- A comparison of deposition studies of polystyrene beads and *Bacillus subtilis* revealed that polystyrene beads are a good proxy for a qualitative study of *Bacillus subtilis* deposition at the initial stage of cake layer formation.

These methods and insights provided the basis to investigate fouling propensity in a forward osmosis spiral-wound module. Design guidelines for a pulsating forward osmosis system treating difficult feed water were derived. The main conclusions were as follows:

- The forward osmosis process must be optimized concerning fouling propensity. The ratio of permeate water flux to crossflow velocity square can be used to estimate the deposition probability in spiral-wound modules. A high ratio indicates high fouling propensity.
- The probability of bacterial attachment is higher in stagnant regions of low fluid shear, high ion, nutrient, and carbon concentration. Adapting the spacer design could be a viable method to minimize stagnant regions. Critical regions for particle deposition can be identified based on the methods developed in this dissertation.
- Pulsating flows are a viable tool for fouling mitigation. Short spiral-wound modules should be used, as damping effects diminish the impact of pulsating flows along the spiral-wound module.

Bibliography

[1] P. W. Atkins, J. de Paula, Atkins' physical chemistry, 10th Edition, Oxford University Press, New York, 2014.

[2] A. Tiraferri, N. Y. Yip, A. P. Straub, S. Romero-Vargas Castrillon, M. Elimelech, A method for the simultaneous determination of transport and structural parameters of forward osmosis membranes, Journal of Membrane Science 444 (2013) 523–538. doi:10.1016/j.memsci.2013.05.023.

[3] A. Bogler, S. Lin, E. Bar-Zeev, Biofouling of membrane distillation, forward osmosis and pressure retarded osmosis: Principles, impacts and future directions, Journal of Membrane Science 542 (2017) 378–398. doi:10.1016/j.memsci.2017.08.001.

[4] R. Allgayer, Effect of Hydrodynamics on the Early Stages of Particle Deposition in Membrane Systems, Master's Thesis, Technische Universität München (2020).

[5] R. V. Linares, Z. Li, M. Elimelech, G. Amy, H. Vrouwenvelder, Recent Developments in Forward Osmosis Processes, Vol. 16, IWA Publishing, 2017. doi:10.2166/9781780408125.

[6] A. Tal, Seeking Sustainability: Israel's Evolving Water Management Strategy, Science 313 (2007) 1081–1084.

[7] K. Madwar, H. Tarazi, Desalination techniques for industrial wastewater reuse, Desalination 152 (1-3) (2003) 325–332. doi:10.1016/S0011-9164(02)01080-9.

[8] R. Ordóñez, D. Hermosilla, N. Merayo, A. Gascó, C. Negro, A. Blanco, Application of multi-barrier membrane filtration technologies to reclaim municipal wastewater for industrial use, Separation and Purification Reviews 43 (2014) 263–310. doi:10.1080/15422119.2012.758638.

[9] S. E. Kwan, E. Bar-Zeev, M. Elimelech, Biofouling in forward osmosis and reverse osmosis: Measurements and mechanisms, Journal of Membrane Science 493 (2015) 703–708. doi:10.1016/j.memsci.2015.07.027.

[10] H. Yoon, Y. Baek, J. Yu, J. Yoon, Biofouling occurrence process and its control in the forward osmosis, Desalination 325 (2013) 30–36. doi:10.1016/j.desal.2013.06.018.

[11] M. Elimelech, W. Phillip, The future of seawater desalination: energy, technology, and the environment., Science 333 (2011) 712–717. doi:10.1126/science.1200488.

[12] K. Lutchmiah, A. R. D. Verliefde, K. Roest, L. C. Rietveld, E. R. Cornelissen, Forward osmosis for application in wastewater treatment: A review, Water research 58 (2014) 179–197. doi:10.1016/j.watres.2014.03.045.

[13] D. Karl Anderson, Concentration of Dilute Industrial Wastes by Direct Osmosis, Ph.D. thesis, University of Rhode Island (1977).

[14] B. D. Coday, P. Xu, E. G. Beaudry, J. Herron, K. Lampi, N. T. Hancock, T. Y. Cath, The sweet spot of forward osmosis: Treatment of produced water, drilling wastewater, and other complex and difficult liquid streams, Desalination 333 (2014) 23–35. doi:10.1016/j.desal.2013.11.014.

[15] S. Zhang, P. Wang, X. Fu, T. S. Chung, Sustainable water recovery from oily wastewater via forward osmosis-membrane distillation (FO-MD), Water Research 52 (2014) 112–121. doi:10.1016/j.watres.2013.12.044.

[16] R. J. York, R. S. Thiel, E. G. Beaudry, Full-scale experience of direct osmosis concentration applied to leachate management, in: Proceedings of the international waste management and landfill symposium, 1999, pp. 359–366.

[17] R. W. Holloway, A. E. Childress, K. E. Dennett, T. Y. Cath, Forward osmosis for concentration of anaerobic digester centrate, Water Research 41 (2007) 4005–4014. doi:10.1016/j.watres.2007.05.054.

[18] E. R. Cornelissen, D. Harmsen, K. F. de Korte, C. J. Ruiken, J. J. Qin, H. Oo, L. P. Wessels, Membrane fouling and process performance of forward osmosis membranes on activated sludge, Journal of Membrane Science 319 (2008) 158–168. doi:10.1016/j.memsci.2008.03.048.

[19] R. Valladares Linares, Z. Li, M. Abu-Ghdaib, C.-H. Wei, G. Amy, J. S. Vrouwenvelder, Water harvesting from municipal wastewater via osmotic gradient: An evaluation of process performance, Journal of Membrane Science 447 (2013) 50–56. doi:10.1016/j.memsci.2013.07.018.

[20] K. Lutchmiah, E. R. Cornelissen, D. J. Harmsen, J. W. Post, K. Lampi, H. Ramaekers, L. C. Rietveld, K. Roest, Water recovery from sewage using forward osmosis, Water Science and Technology 64 (2011) 1443–1449. doi:10.2166/wst.2011.773.

[21] J. E. Kim, S. Phuntsho, F. Lotfi, H. K. Shon, Investigation of pilot-scale 8040 FO membrane module under different operating conditions for brackish water desalination, Desalination and Water Treatment 53 (2014) 2782–2791. doi:10.1080/19443994.2014.931528.

[22] R. Valladares Linares, S. S. Bucs, Z. Li, M. AbuGhdeeb, G. Amy, J. S. Vrouwenvelder, Impact of spacer thickness on biofouling in forward osmosis, Water Research 57 (2014) 223–233. doi:10.1016/j.watres.2014.03.046.

[23] J. S. Vrouwenvelder, J. A. M. van Paassen, J. M. C. van Agtmaal, M. C. M. van Loosdrecht, J. C. Kruithof, A critical flux to avoid

biofouling of spiral wound nanofiltration and reverse osmosis membranes: Fact or fiction?, Journal of Membrane Science 326 (2009) 36–44. doi:10.1016/j.memsci.2008.09.029.

[24] I. W. Sutherland, Biofilm exopolysaccharides: A strong and sticky framework, Microbiology 147 (1) (2001) 3–9. doi:10.1099/00221287-147-1-3.

[25] M. Herzberg, S. Kang, M. Elimelech, Role of extracellular polymeric substances (EPS) in biofouling of reverse osmosis membranes, Environmental Science and Technology 43 (12) (2009) 4393–4398. doi:10.1021/es900087j.

[26] E. Rosenberg, E. F. DeLong, S. Lory, E. Stackebrandt, F. Thompson (Eds.), The Prokaryotes: Applied Bacteriology and Biotechnology, Springer-Verlag Berlin Heidelberg, 2013.

[27] L. Li, X.-p. Liu, H.-q. Li, A review of forward osmosis membrane fouling: types, research methods and future prospects, Environmental Technology Reviews 6 (1) (2017) 26–46. doi:10.1080/21622515.2016.1278277.

[28] E. Bar-Zeev, U. Passow, S. Romero-Vargas Castrillón, M. Elimelech, Transparent exopolymer particles: From aquatic environments and engineered systems to membrane biofouling, Environmental Science and Technology 49 (2) (2015) 691–707. doi:10.1021/es5041738.

[29] H.-C. Flemming, G. Schaule, T. Griebe, J. Schmitt, A. Tamachkiarowa, Biofouling - The Achilles heel of membrane processes, Desalination 113 (1997) 215–225. doi:10.1016/S0011-9164(97)00132-X.

[30] E. Bar-Zeev, I. Berman-Frank, O. Girshevitz, T. Berman, Revised paradigm of aquatic biofilm formation facilitated by microgel transparent exopolymer particles, Proceedings of the National Academy of Sciences of the United States of America 109 (2012) 9119–9124. doi:10.1073/pnas.1203708109.

[31] W. Guo, H.-H. Ngo, J. Li, A mini-review on membrane fouling, Bioresource Technology 122 (2012) 27–34. doi:10.1016/j.biortech.2012.04.089.

[32] A. I. Radu, M. S. H. van Steen, J. S. Vrouwenvelder, M. C. M. van Loosdrecht, C. Picioreanu, Spacer geometry and particle deposition in spiral wound membrane feed channels, Water Research 64 (2014) 160–176. doi:10.1016/j.watres.2014.06.040.

[33] T. H. Chong, F. S. Wong, A. G. Fane, Implications of critical flux and cake enhanced osmotic pressure (CEOP) on colloidal fouling in reverse osmosis: Experimental observations, Journal of Membrane Science 314 (2008) 101–111. doi:10.1016/j.memsci.2008.01.030.

[34] A. Subramani, E. Hoek, Direct observation of initial microbial deposition onto reverse osmosis and nanofiltration membranes, Journal of Membrane Science 319 (2008) 111–125. doi:10.1016/j.memsci.2008.03.025.

[35] Y.-L. Li, T.-H. Chang, C.-Y. Wu, C.-J. Chuang, K.-L. Tung, CFD analysis of particle deposition in the spacer-filled membrane module, Journal of Water Supply: Research and Technology - AQUA 55 (2006) 589–601. doi:10.2166/aqua.2006.058.

[36] S. Zou, Y.-N. Wang, F. Wicaksana, T. Aung, P. C. Y. Wong, A. G. Fane, C. Y. Tang, Direct microscopic observation of forward osmosis membrane fouling by microalgae: Critical flux and the role of operational conditions, Journal of Membrane Science 436 (2013) 174–185. doi:10.1016/j.memsci.2013.02.030.

[37] S. Kerdi, A. Qamar, J. S. Vrouwenvelder, N. Ghaffour, Effect of localized hydrodynamics on biofilm attachment and growth in a cross-flow filtration channel, Water Research 188 (2021) 116502. doi:10.1016/j.watres.2020.116502.

[38] S. T. Kuruneru, E. Sauret, S. C. Saha, Y. T. Gu, Coupled CFD-DEM simulation of oscillatory particle-laden fluid flow through a

porous metal foam heat exchanger: Mitigation of particulate fouling, Chemical Engineering Science 179 (2018) 32–52. doi:10.1016/j.ces.2018.01.006.

[39] B. Liberman, L. Eshed, G. Greenberg, Pulse Flow RO - The new RO technology for waste and brackish water applications, Desalination 479 (2020) 114336. doi:10.1016/j.desal.2020.114336.

[40] S. S. Giri, M. Harshiny, S. S. Sen, V. Sukumaran, S. C. Park, Production and characterization of a thermostable bioflocculant from Bacillus subtilis F9, isolated from wastewater sludge, Ecotoxicology and Environmental Safety 121 (2015) 45–50. doi:10.1016/J.ECOENV.2015.06.010.

[41] P. Wattiau, M.-E. Renard, P. Ledent, V. Debois, G. Blackman, S. Agathos, A PCR test to identify Bacillus subtilis and closely related species and its application to the monitoring of wastewater biotreatment, Applied Microbiology and Biotechnology 56 (5-6) (2001) 816–819. doi:10.1007/s002530100691.

[42] E. Bar-Zeev, M. Elimelech, Reverse osmosis biofilm dispersal by osmotic back-flushing: Cleaning via substratum perforation, Environmental Science & Technology Letters 1 (2014) 162–166. doi:10.1021/ez400183d.

[43] M. M. Gimmelshtein, R. Semiat, Investigation of flow next to membrane walls, Journal of Membrane Science 264 (2005) 137–150. doi:10.1016/j.memsci.2005.04.033.

[44] J. M. Passmore, D. L. Rudolph, M. M. Mesquita, E. E. Cey, M. B. Emelko, The utility of microspheres as surrogates for the transport of E. coli RS2g in partially saturated agricultural soil, Water Research 44 (4) (2010) 1235–1245. doi:10.1016/j.watres.2009.10.010.

[45] A. I. Radu, Modeling Fouling in Spiral Wound Membrane Systems, Ph.D. thesis, Delft University of Technology (2014). doi:10.4233/uuid:e5b8ff75-73dd-444f-8213-0b4acfd2378e.

[46] A. Bogler, A. Kastl, M. Spinnler, T. Sattelmayer, A. Be'er, E. Bar-Zeev, Where, when and why? Quantifying the relation of particle deposition to crossflow velocity and permeate water flux in forward osmosis, Journal of Membrane Science 604 (March) (2020) 118055. doi:10.1016/j.memsci.2020.118055.

[47] A. Bogler, A. Kastl, M. Spinnler, T. Sattelmayer, A. Be'er, E. Bar-Zeev, Particle counting and tracking: Zooming on deposition and flow paths during initial stages of cake formation in forward osmosis with spacers, Journal of Membrane Science 597 (2020) 117619. doi:10.1016/j.memsci.2019.117619.

[48] J. Meinders, H. van der Mei, H. Busscher, Deposition efficiency and reversibility of bacterial adhesion under flow, Journal of Colloid and Interface Science 176 (2) (1995) 329–341. doi:10.1006/jcis.1995.9960.

[49] E. C. W. Clarke, D. N. Glew, Evaluation of the Thermodynamic Functions for Aqueous Sodium Chloride from Equilibrium and Calorimetric Measurements below 154 °C, Journal of Physical and Chemical Reference Data 14 (1985) 489–610. doi:10.1063/1.555730.

[50] W. A. Phillip, J. S. Yong, M. Elimelech, Reverse draw solute permeation in forward osmosis: Modeling and experiments, Environmental Science and Technology 44 (13) (2010) 5170–5176. doi:10.1021/es100901n.

[51] G. Schock, A. Miquel, Mass transfer and pressure loss in spiral wound modules, Desalination 64 (1987) 339–352. doi:10.1016/0011-9164(87)90107-X.

[52] A. Bhinder, S. Shabani, M. Sadrzadeh, Effect of Internal and External Concentration Polarizations on the Performance of Forward Osmosis Process, in: Osmotically Driven Membrane Processes - Approach, Development and Current Status, IntechOpen, 2018, pp. 67–85. doi:10.5772/intechopen.71343.

[53] Z. Alihemati, S. A. Hashemifard, T. Matsuura, A. F. Ismail, N. Hilal, Current status and challenges of fabricating thin film composite forward osmosis membrane: A comprehensive roadmap, Desalination 491 (2020) 114557. doi:10.1016/j.desal.2020.114557.

[54] Y. N. Wang, K. Goh, X. Li, L. Setiawan, R. Wang, Membranes and processes for forward osmosis-based desalination: Recent advances and future prospects, Desalination 434 (2018) 81–99. doi:10.1016/j.desal.2017.10.028.

[55] Q. Ge, M. Ling, T. S. Chung, Draw solutions for forward osmosis processes: Developments, challenges, and prospects for the future, Journal of Membrane Science 442 (2013) 225–237. doi:10.1016/j.memsci.2013.03.046.

[56] J. R. McCutcheon, R. L. McGinnis, M. Elimelech, A novel ammonia-carbon dioxide forward (direct) osmosis desalination process, Desalination 174 (2005) 1–11. doi:10.1016/j.desal.2004.11.002.

[57] Q. Ge, J. Su, G. L. Amy, T. S. Chung, Exploration of polyelectrolytes as draw solutes in forward osmosis processes, Water Research 46 (4) (2012) 1318–1326. doi:10.1016/j.watres.2011.12.043.

[58] D. Li, X. Zhang, G. P. Simon, H. Wang, Forward osmosis desalination using polymer hydrogels as a draw agent: Influence of draw agent, feed solution and membrane on process performance, Water Research 47 (1) (2013) 209–215. doi:10.1016/j.watres.2012.09.049.

[59] Y. Cai, W. Shen, R. Wang, W. B. Krantz, A. G. Fane, X. Hu, CO2 switchable dual responsive polymers as draw solutes for forward osmosis desalination, Chemical Communications 49 (75) (2013) 8377–8379. doi:10.1039/c3cc43289k.

[60] Q. Ge, J. Su, T. S. Chung, G. Amy, Hydrophilic superparamagnetic nanoparticles: Synthesis, characterization, and performance in forward osmosis processes, Industrial and Engineering Chemistry Research 50 (2011) 382–388. doi:10.1021/ie101013w.

[61] C. T. Crowe, J. D. Schwarzkopf, M. Sommerfeld, Y. Tsuji, Multiphase Flows with Droplets and Particles, 2nd Edition, CRC Press Taylor & Francis Group, Boca Raton, 2012.

[62] C. Shankararaman, M. R. Wiesner, Particle Transport in Clean Membrane Filters in Laminar Flow, Environmental Science and Technology 26 (8) (1992) 1611–1621. doi:10.1021/es00032a019.

[63] M. R. Maxey, J. J. Riley, Equation of motion for a small rigid sphere in a nonuniform flow, Physics of Fluids 26 (4) (1983) 883–889. doi:10.1063/1.864230.

[64] C. Henry, J. P. Minier, G. Lefèvre, Towards a description of particulate fouling: From single particle deposition to clogging, Advances in Colloid and Interface Science 185-186 (2012) 34–76. doi:10.1016/j.cis.2012.10.001.

[65] L. Song, M. Elimelech, Particle Deposition onto a Permeable Surface in Laminar Flow, Journal of Colloid and Interface Science 173 (1995) 165–180. doi:10.1006/jcis.1995.1310.

[66] M. Elimelech, J. Gregory, X. Jia, R. A. Williams, Particle Deposition and Aggregation, Butterworth-Heinemann, Woburn, MA, 1995. doi:10.1016/c2013-0-04548-3.

[67] H. C. Hamaker, The London-Van Der Waals attraction between spherical particles, Physica 4 (1937) 1058–1072.

[68] J. Visser, On Hamaker constants: A comparison between Hamaker constants and Lifshitz-van der Waals constants, Advances in Colloid and Interface Science 3 (1972) 331–363. doi:10.1016/0001-8686(72)85001-2.

[69] J. Gregory, Approximate Expressions for Retarded van der Waals Interaction, Journal of Colloid And Interface Science 83 (1) (1981) 138–145. doi:10.1016/0021-9797(81)90018-7.

[70] H. Helmholtz, Über elektrische Grenzschichten, Annalen der Physik und Chemie 7 (1879) 337–382.

[71] D. L. Chapman, A contribution to the theory of electrocapillarity, The London, Edinburgh, and Dublin Philisophical Magazine and Journal of Science 25 (1913) 475–481.

[72] L. G. Guoy, Sur la construction de la charge electrique a la surface d'un electrolyte, Journal de Physique 9 (1910) 657–668.

[73] O. Stern, Zur Theorie der elektrolytischen Doppelschicht, Zeitschrift für Elektrochemie und Angewandte Physikalische Chemie 30 (1924) 508–516.

[74] R. Hogg, T. W. Healy, D. W. Fuerstenau, Mutual coagulation of colloidal dispersions, Transactions of the Faraday Society 62 (1966) 1638–1651. doi:10.1039/tf9666201638.

[75] A. Putnam, Integrable form of droplet drag coefficient, Journal of American Rocket Society 31 (1961) 1467–1468.

[76] P. G. Saffman, The lift on a small sphere in a slow shear flow, Journal of Fluid Mechanics 22 (1965) 385–400. doi:10.1017/S0022112065000824.

[77] J. B. Mclaughlin, Inertial migration of a small sphere in linear shear flows, Journal of Fluid Mechanics 224 (1991) 261–274. doi:10.1017/S0022112091001751.

[78] R. Mei, An approximate expression for the shear lift force on a spherical particle at finite Reynolds number, International Journal of Multiphase Flow 18 (1992) 145–147. doi:10.1016/0301-9322(92)90012-6.

[79] B. Derjaguin, L. Landau, Theory of the stability of strongly charged lyophobic sols and of the adhesion of strongly charged particles in solutions of electrolytes, Progress in Surface Science 43 (1993) 30–59. doi:10.1016/0079-6816(93)90013-L.

[80] E. J. W. Verwey, J. T. G. Overbeek, K. van Nes, Theory of the Stability of Lyophobic Colloids: The Interaction of Sol Particles Having an Electric Double Layer, Elsevier Publishing Company, 1948.

[81] A. Kastl, A. Bogler, M. Spinnler, T. Sattelmayer, A. Be'er, E. Bar-Zeev, Impact of Hydrodynamics on the First Stages of Biofilm Formation in Forward Osmosis with Spacers, Environmental science & technology 54 (2020) 5279–5287. doi:10.1021/acs.est.0c00380.

[82] P. Glueckstern, M. Priel, E. Gelman, N. Perlov, Wastewater desalination in Israel, Desalination 222 (2008) 151–164. doi:10.1016/j.desal.2007.01.143.

[83] L. Fortunato, S. Bucs, R. V. Linares, C. Cali, J. S. Vrouwenvelder, T. O. Leiknes, Spatially-resolved in-situ quantification of biofouling using optical coherence tomography (OCT) and 3D image analysis in a spacer filled channel, Journal of Membrane Science 524 (2017) 673–681. doi:10.1016/j.memsci.2016.11.052.

[84] Y. Wibisono, K. El Obied, E. Cornelissen, A. J. Kemperman, K. Nijmeijer, Biofouling removal in spiral-wound nanofiltration elements using two-phase flow cleaning, Journal of Membrane Science 475 (2015) 131–146. doi:10.1016/j.memsci.2014.10.016.

[85] S. West, M. Wagner, C. Engelke, H. Horn, Optical coherence tomography for the in situ three-dimensional visualization and quantification of feed spacer channel fouling in reverse osmosis membrane modules, Journal of Membrane Science 498 (2016) 345–352. doi:10.1016/j.memsci.2015.09.047.

[86] L. Fortunato, Y. Jang, J.-G. Lee, S. Jeong, S. Lee, T. Leiknes, N. Ghaffour, Fouling development in direct contact membrane distillation: Non-invasive monitoring and destructive analysis, Water Research 132 (2018) 34–41. doi:10.1016/j.watres.2017.12.059.

[87] S. S. Bucs, R. Valladares Linares, J. O. Marston, A. I. Radu, J. S. Vrouwenvelder, C. Picioreanu, R. V. Linares, J. O. Marston, A. I. Radu, J. S. Vrouwenvelder, C. Picioreanu, Experimental and numerical characterization of the water flow in spacer-filled channels of spiral-wound membranes, Water Research 87 (2015) 299–310. doi:10.1016/j.watres.2015.09.036.

[88] A. H. Haidari, S. G. Heijman, W. G. van der Meer, Visualization of hydraulic conditions inside the feed channel of Reverse Osmosis: A practical comparison of velocity between empty and spacer-filled channel, Water Research 106 (2016) 232–241. doi:10.1016/j.watres.2016.10.012.

[89] T. R. Pintelon, S. A. Creber, D. A. Graf von der Schulenburg, M. L. Johns, Validation of 3D simulations of reverse osmosis membrane biofouling, Biotechnology and Bioengineering 106 (4) (2010) 677–689. doi:10.1002/bit.22717.

[90] B. Manz, F. Volke, D. Goll, H. Horn, Measuring local flow velocities and biofilm structure in biofilm systems with Magnetic Resonance Imaging (MRI), Biotechnology and Bioengineering 84 (4) (2003) 424–432. doi:10.1002/bit.10782.

[91] Y. Gao, S. Haavisto, C. Y. Tang, J. Salmela, W. Li, Characterization of fluid dynamics in spacer-filled channels for membrane filtration using Doppler optical coherence tomography, Journal of Membrane Science 448 (2013) 198–208. doi:10.1016/j.memsci.2013.08.011.

[92] M. Herzberg, M. Elimelech, Physiology and genetic traits of reverse osmosis membrane biofilms: A case study with Pseudomonas aeruginosa, ISME Journal 2 (2008) 180–194. doi:10.1038/ismej.2007.108.

[93] S. Suwarno, X. Chen, T. Chong, D. McDougald, Y. Cohen, S. Rice, A. Fane, Biofouling in reverse osmosis processes: The roles of flux, crossflow velocity and concentration polarization in biofilm development, Journal of Membrane Science 467 (2014) 116–125. doi:10.1016/j.memsci.2014.04.052.

[94] I. S. Ngene, R. G. Lammertink, M. Wessling, W. G. Van der Meer, Particle deposition and biofilm formation on microstructured membranes, Journal of Membrane Science 364 (2010) 43–51. doi:10.1016/j.memsci.2010.07.048.

[95] D. A. Drew, J. A. Schonberg, G. Belfort, Lateral inertial migration of a small sphere in fast laminar flow through a membrane duct, Chemical Engineering Science 46 (12) (1991) 3219–3224. doi:10.1016/0009-2509(91)85023-Q.

[96] R. M. Martinez, Bacillus subtilis, in: Brenner's Encyclopedia of Genetics: Second Edition, 2013th Edition, Elsevier Inc., 2013, pp. 246–248. doi:10.1016/B978-0-12-374984-0.00125-X.

[97] C. Picioreanu, J. S. Vrouwenvelder, M. C. van Loosdrecht, Three-dimensional modeling of biofouling and fluid dynamics in feed spacer channels of membrane devices, Journal of Membrane Science 345 (2009) 340–354. doi:10.1016/j.memsci.2009.09.024.

[98] J. S. Vrouwenvelder, C. Hinrichs, W. G. J. van der Meer, M. C. M. van Loosdrecht, J. C. Kruithof, Pressure drop increase by biofilm accumulation in spiral wound RO and NF membrane systems: Role of substrate concentration, flow velocity, substrate load and flow direction, Biofouling 25 (6) (2009) 543–555. doi:10.1080/08927010902972225.

[99] Y. L. Li, K. L. Tung, Y. S. Chen, K. J. Hwang, CFD analysis of the initial stages of particle deposition in spiral-wound membrane modules, Desalination 287 (2012) 200–208. doi:10.1016/j.desal.2011.10.001.

[100] M. Gruber, C. Johnson, C. Tang, M. Jensen, L. Yde, C. Hélix-Nielsen, Computational fluid dynamics simulations of flow and concentration polarization in forward osmosis membrane systems, Journal of Membrane Science 379 (2011) 488–495. doi:10.1016/j.memsci.2011.06.022.

[101] N. Horstmeyer, T. Lippert, D. Schön, F. Schlederer, C. Picioreanu, K. Achterhold, F. Pfeiffer, J. E. Drewes, CT scanning of membrane feed spacers – Impact of spacer model accuracy on hydrodynamic and solute transport modeling in membrane feed channels, Journal of Membrane Science 564 (July) (2018) 133–145. doi:10.1016/j.memsci.2018.07.006.

[102] A. Qamar, S. Bucs, C. Picioreanu, J. Vrouwenvelder, N. Ghaffour, Hydrodynamic flow transition dynamics in a spacer filled filtration channel using direct numerical simulation, Journal of Membrane Science 590 (February) (2019) 117264. doi:10.1016/j.memsci.2019.117264.

[103] G. A. Fimbres-Weihs, D. E. Wiley, Numerical study of mass transfer in three-dimensional spacer-filled narrow channels with steady flow, Journal of Membrane Science 306 (1-2) (2007) 228–243. doi:10.1016/j.memsci.2007.08.043.

[104] F. Kiefer, Multi-Effect Vacuum Membrane Distillation for High-Recovery Desalination, Ph.D. thesis, Technische Universität München (2020).

[105] A. Präbst, F. Kiefer, A. Kroiß, M. Spinnler, T. Sattelmayer, Influence of dynamic operation of reverse osmosis systems on fluid dynamics and mass transfer by investigation of 2-D spacer filled channels, Desalination and Water Treatment 73 (2017) 22–26. doi:10.5004/dwt.2017.20531.

[106] PFO MEMBRANE, Tech. Rep. July, Porifera (2018).

[107] G. Hurwitz, G. R. Guillen, E. M. Hoek, Probing polyamide membrane surface charge, zeta potential, wettability, and hydrophilicity with contact angle measurements, Journal of Membrane Science 349 (1-2) (2010) 349–357. doi:10.1016/j.memsci.2009.11.063.

[108] S. L. McGill, H. D. Smyth, Disruption of the mucus barrier by topically applied exogenous particles, Molecular Pharmaceutics 7 (6) (2010) 2280–2288. doi:10.1021/mp100242r.

[109] I. D. Johnson, Ultrasensitive detection technology, in: I. Johnson, M. T. Spence (Eds.), Molecular Probes Handbook: A guide to fluorescent probes and labeling technologies, 11th Edition, Life Technologies Corporation, 2010, Ch. 6, p. 1060.

[110] M. M. Motsa, B. B. Mamba, A. D'Haese, E. Hoek, A. R. D. Verliefde, Organic fouling in forward osmosis membranes: The role of

feed solution chemistry and membrane structural properties, Journal of Membrane Science 460 (2014) 99–109. doi:10.1016/j.memsci.2014.02.035.

[111] V. Kochkodan, N. Hilal, A comprehensive review on surface modified polymer membranes for biofouling mitigation, Desalination 356 (2015) 187–207. doi:10.1016/j.desal.2014.09.015.

[112] E. M. Hoek, S. Bhattacharjee, M. Elimelech, Effect of membrane surface roughness on colloid-membrane DLVO interactions, Langmuir 19 (11) (2003) 4836–4847. doi:10.1021/la027083c.

[113] K. Doblhoff-Dier, K. Kudlaty, M. Wiesinger, M. Gröschl, Time resolved measurement of pulsating flow using orifices, Flow Measurement and Instrumentation 22 (2011) 97–103. doi:10.1016/j.flowmeasinst.2010.12.001.

[114] A. Kastl, A. Präbst, F. Kiefer, M. Spinnler, T. Sattelmayer, Colloidal fouling mitigation using pulsating flows in osmotic membrane processes, Desalination and Water Treatment 157 (2019) 228–241. doi:10.5004/dwt.2019.23778.

[115] C. Boxler, W. Augustin, S. Scholl, Composition of milk fouling deposits in a plate heat exchanger under pulsed flow conditions, Journal of Food Engineering 121 (2014) 1–8. doi:10.1016/j.jfoodeng.2013.08.003.

[116] S. Kerdi, A. Qamar, J. S. Vrouwenvelder, N. Ghaffour, Fouling resilient perforated feed spacers for membrane filtration, Water Research 140 (2018) 211–219. doi:10.1016/j.watres.2018.04.049.

[117] E. Meißner, Berechnung pulsierender Strömung in Systemen aus Kunststoffleitungen mit Berücksichtigung von Reibungsverlusten, Forschung im Ingenieurwesen 43 (2) (1977) 53–63. doi:10.1007/BF02574542.

[118] H. F. Ridgway, A. Kelly, C. Justice, B. H. Olson, Microbial fouling of reverse-osmosis membranes used in advanced wastewater treatment

technology: Chemical, bacteriological, and ultrastructural analyses, Applied and Environmental Microbiology 45 (3) (1983) 1066–1084. doi:10.1128/aem.45.3.1066-1084.1983.

[119] H. S. Vrouwenvelder, J. A. Van Paassen, H. C. Folmer, J. A. Hofman, M. M. Nederlof, D. Van Der Kooij, Biofouling of membranes for drinking water production, Desalination 118 (1-3) (1998) 157–166. doi:10.1016/S0011-9164(98)00116-7.

[120] J. S. Vrouwenvelder, J. A. van Paassen, L. P. Wessels, A. F. van Dam, S. M. Bakker, The Membrane Fouling Simulator: A practical tool for fouling prediction and control, Journal of Membrane Science 281 (1-2) (2006) 316–324. doi:10.1016/j.memsci.2006.03.046.

[121] C. S. Ong, P. S. Goh, W. J. Lau, N. Misdan, A. F. Ismail, Nanomaterials for biofouling and scaling mitigation of thin film composite membrane: A review, Desalination 393 (2016) 2–15. doi:10.1016/j.desal.2016.01.007.

[122] M. Gryta, The assessment of microorganism growth in the membrane distillation system, Desalination 142 (1) (2002) 79–88. doi:10.1016/S0011-9164(01)00427-1.

[123] R. P. Carnahan, L. Bolin, W. Suratt, Biofouling of PVD-1 reverse osmosis elements in the water treatment plant of the City of Dunedin, Florida, Desalination 102 (1-3) (1995) 235–244. doi:10.1016/0011-9164(95)00059-B.

[124] P. J. Roache, Perspective: A method for uniform reporting of grid refinement studies, Journal of Fluids Engineering 116 (1994) 405–413. doi:10.1115/1.2910291.

A Appendix

A.1 Grid Convergency Study

Calculating particle deposition with CFD is a two step process. First, fluid velocity and salt mass fraction are calculated in a mesh (cf. Sec. 4.1.2). The results are then used to calculate the forces that affect a particle and the resulting particle trajectory (cf. 2.31). Hence, it is important that the results of the first step are independent of the mesh to assure a correct calculation of particle trajectories and deposition behavior.

A grid convergence index (GCI) study can assure the mesh independence of results for fluid velocity and the salt mass fraction at the membrane. The study was conducted according to Roache [124] (cf. Fig. A.1). At a cell

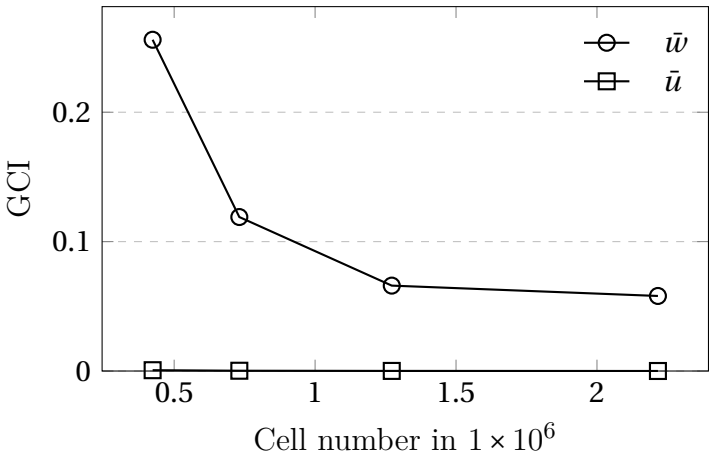

Figure A.1: GCI study for the average salt mass fraction at the membrane boundary $\bar{w}$ and the average fluid velocity $\bar{u}$ above the bottom spacer filament [4].

number of 1.3×10^6, the GCI did not change significantly when increased

to 2.2×10^6, while the computational effort was significantly higher. Hence, a cell number of 1.3×10^6 was chosen for the mesh.

A.2 Calibration of Orifices for the Damping Experiment

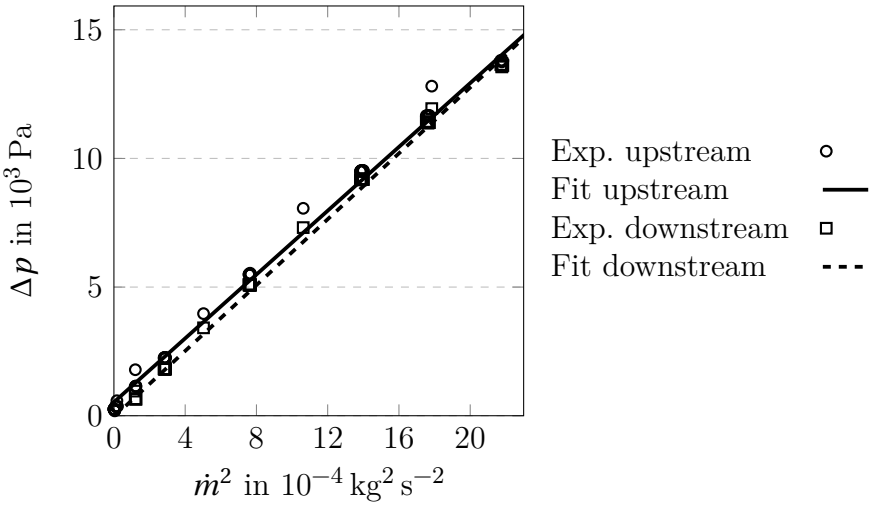

Figure A.2: Steady-state experiment to determine A_{orifice} for the upstream and downstream Orifice. Pressure difference Δp across orifice over squared mass flow rate $\dot{m}^2$.

Table A.1: Design of damping experiments to determine B_{orifice} with the variables volume flow rate $\dot{V}$, frequency f and duty value of the valve.

ID	Duty value	$\dot{V}$ in $\mathrm{L\,h^{-1}}$	f in Hz
1	0.4	72	3
2	0.4	105	3
3	0.4	74	6.5
4	0.4	112	6.5
5	0.4	73	10
6	0.4	112	10
7	0.5	79	3
8	0.5	111	3
9	0.5	75	6.5
10	0.5	113	6.5
11	0.5	70	10
12	0.5	115	10
13	0.3	62	3
14	0.3	92	3
15	0.3	61	6.5
16	0.3	94	6.5
17	0.3	66	10
18	0.3	96	10

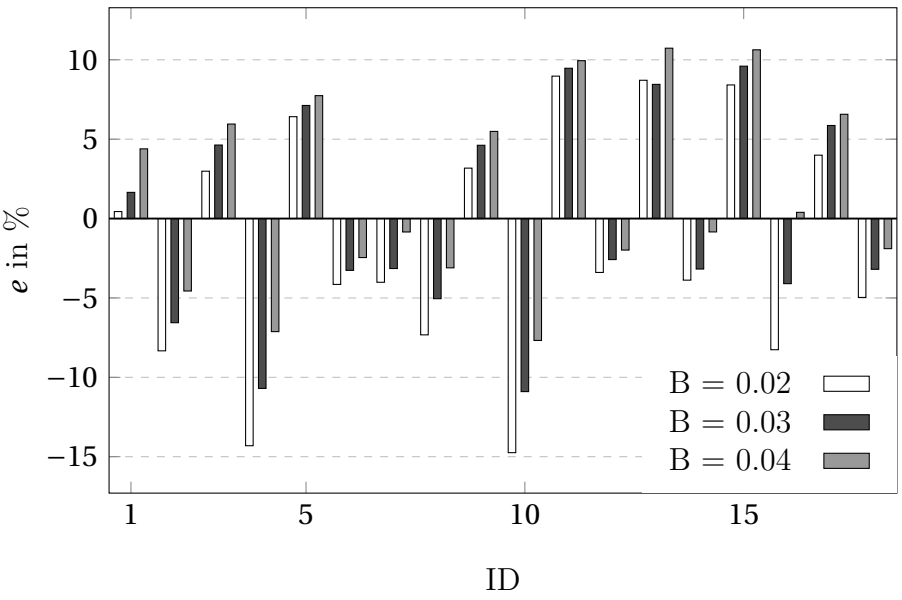

Figure A.3: Error e over experiment ID (cf. Tab. A.1) for several values of B_{orifice}.

A.3 Previous Publications

Parts of this dissertation were published by the author in journal papers [46, 47, 81, 114]. All of these prior printed publications are registered according to the valid doctoral regulations. However, not all of them are quoted explicitly everywhere. Whether these personal prior printed publications were referenced depended on maintaining comprehensibility and providing all necessary context.

A.4 Supervised Student Theses

Associated with this dissertation, a number of student theses were supervised by the author of the present work. These theses were prepared at the Lehrstuhl für Thermodynamik, Technische Universität München in the years 2017 to 2020 under the close supervision of the present author. Parts of these supervised theses may be incorporated into the present thesis. The author would like to express his sincere gratitude to all formerly supervised students for their commitment and support of this research project.

Student	**Titel/Thesis**
Raphaela Allgayer	Effect of Hydrodynamics on the Early Stages of Particle Deposition in Membrane Systems, Master's Thesis, August 2020
Mischa Grussmann	Untersuchung des Dämpfungsverhaltens von Pulsierenden Strömungen in Membranprozessen, Semester Thesis, December 2018
Lukas Eicke	Experimentelle Untersuchung des Foulingverhaltens bei der Vorwärtsosmose, Bachelor's Thesis, November 2018